Journal of Volcanology and Geothermal Research 455 (2024) 108187

Contents lists available at ScienceDirect

Journal of Volcanology and Geothermal Research

journal homepage: www.journals.elsevier.com/journal-of-volcanology-and-geothermal-research

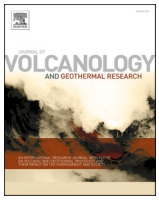

Invited review article

New perspectives on ice forcing in continental arc magma plumbing systems

Brad S. Singer [a,*], Pablo Moreno-Yaeger [a], Meredith Townsend [b], Christian Huber [c], Joshua Cuzzone [d], Benjamin R. Edwards [e], Matias Romero [a], Yasmeen Orellana-Salazar [a], Shaun A. Marcott [a], Rachel E. Breunig [a], Ken L. Ferrier [a], Kathryn Scholz [f], Allie N. Coonin [c], Brent V. Alloway [g], Marissa M. Tremblay [h], Sally Stevens [a], Ivo Fustos-Toribio [i], Patricio I. Moreno [j], Franco Vera [k], Álvaro Amigo [k]

[a] Dept. of Geoscience, University of Wisconsin-Madison, 1215 West Dayton Street, Madison, WI 53706, United States of America
[b] Dept. of Earth and Environmental Sciences, Lehigh University, 1 West Packer Avenue, Bethlehem, PA 18015, United States of America
[c] Dept. of Earth, Environmental, and Planetary Sciences, Brown University, Providence, RI, 02912, United States of America
[d] Joint Institute for Regional Earth System Science and Engineering, University of California, 607 Charles E. Young Drive East, Los Angeles, CA 90095, United States of America
[e] Dept. of Geosciences, Dickinson College, P.O. Box 1773, Carlisle, PA 17013, United States of America
[f] Dept. of Earth Sciences, University of Oregon, Cascade Hall, 100, 1272 University of Oregon, Eugene, OR 97403, United States of America
[g] Instituto de Geografía, Pontificia Universidad Católica de Chile, Santiago, Chile
[h] Dept. of Earth, Atmospheric, and Planetary Sciences, Purdue University, 550 Stadium Mall Drive, West Lafayette, IN 47907, United States of America
[i] Dept. of Ingeniería Civil, Universidad de la Frontera, Temuco, Chile
[j] Dept. de Ciencias Ecológicas, Universidad de Chile, Santiago, Chile
[k] Servicio Nacional de Geología y Minería, Av. Santa María 0104, Providencia, Chile

ARTICLE INFO

Keywords:
Volcanoes
Ice sheets
Crustal stress
Surface loading
Geochronology
Petrology
Numerical modeling
Glaciovolcanism

ABSTRACT

Determining how and why eruptive outputs are modulated by the loading and unloading of ice is key to understanding whether ongoing and accelerating deglaciation across mid- to high-latitudes will impact future activity at many volcanoes. Here, we address two central questions. First, does decompression of the upper crust during rapid thinning of ice sheets propel increases in eruption rates? Second, does surface loading during ice sheet growth, followed by rapid unloading during deglaciation, promote changes in magma storage conditions and compositions within the underlying magma plumbing systems? To provide new perspectives on these questions, we address the mechanics and dynamics of ice sheet-arc magma plumbing system interactions at a regional-to-local scale within the Andean Southern Volcanic Zone. Here, piedmont glacier lobes, forming the northernmost extension of the Patagonian ice sheet, have enveloped dozens of large, active, composite volcanoes as these glaciers reached local thicknesses of nearly 2 km during the local Last Glacial Maximum (LGM) between ~35 and 18 ka, before retreating rapidly between 18 and 15 ka. Our multi-faceted review features a synthesis of existing and new field observations, laboratory measurements, and numerical simulations. Advances in $^{40}Ar/^{39}Ar$ radioisotopic and ^{3}He surface exposure geochronology, in conjunction with geologic mapping, facilitate reconstructions of volcanic eruptive histories spanning the last glacial-deglacial cycle and in places provide constraints on the thickness of ice at specific time slices. The magnitude and geometry of the glacial loading and unloading is captured in a climate model-driven numerical simulation that reveals spatial and temporal heterogeneities in the configuration of the northernmost Patagonian ice sheet retreat. Geological observations including dated moraine complexes, dated lava-ice contact features, and glacial erratic boulders at high altitude on volcano slopes, are consistent with this model. Deep valleys imply intense localized erosion on volcano flanks, and deposited sediment in nearby floodplains implies narrow regions of rapid sediment deposition. These observations, in conjunction with dated lava flows, provide constraints on rates and patterns of crustal loading and unloading by sediment redistribution.

* Corresponding author.
E-mail address: bsinger@wisc.edu (B.S. Singer).

https://doi.org/10.1016/j.jvolgeores.2024.108187
Received 19 June 2024; Received in revised form 30 August 2024; Accepted 4 September 2024
Available online 11 September 2024

The ice loading model, cone growth, and a sediment redistribution history inform numerical simulations of intra-crustal stress changes below the volcanic arc in response to the ice-driven and sediment-driven changes. In turn, the modeled surface loading is central to designing numerical simulations of magma reservoir responses to intra-crustal stress changes beneath the volcanoes. Following periods of subdued volcanic output, upticks in eruptive rates are found at three volcanoes during, or shortly after, the LGM. A numerical magma chamber model suggests that this behavior could be the result of a delicate balance between the timescales of magma cooling, the rate of magma recharge from depth, and viscous relaxation of surrounding crustal rocks. Depressurization of the crust increases eruptive mass flux to the surface only if: (1) the rate of recharge just outcompetes the rate of cooling, (2) the rate of recharge is barely large enough before loading to overcome viscous relaxation of overpressure by creep around the chamber, and (3) magmas are volatile undersaturated, and exsolve volatiles via second boiling during the long repose associated with the high ice loads that precede rapid deglaciation. Existing and newly developed thermobarometers that constrain magma crystallization and storage depths can be applied to eruptive products spanning a glacial-deglacial transition, such that not only secular changes in rates of volcanic eruption, but also changes in the depths of pre-eruptive magma storage and in magma composition can each be interpreted in the light of intra-crustal stress changes associated with glacial loading and unloading.

1. Introduction

The hypothesis that climate driven surface loading and unloading modulates volcanic eruptions by way of deglaciation (Rampino et al., 1979; Hall, 1982) or sea-level change (Matthews, 1968; Walcott, 1972) has been considered for decades. Observations of increased global volcanic activity following the Last Glacial Maximum (LGM) illuminated by Huybers and Langmuir (2009), as well as possible orbital pacing of volcanism on longer time scales suggested by Kutterolf et al. (2013), have renewed interest in the role of climate in driving volcanic activity. Indeed, a growing set of observations hint at a solid earth-cryosphere relationship in which changes in ice sheet thickness, sea level, and volcanic activity track Milankovitch periods (e.g., Geyer and Bindeman, 2011; Kutterolf et al., 2019; Sternai et al., 2019; Edwards et al., 2020; Satow et al., 2021). In parallel, a deeper appreciation of magma plumbing and reservoir systems is emerging that emphasizes complexities in their trans-crustal architecture, multi-component (melt-crystals-volatiles) physical and compositional states, and susceptibility to internal or external eruption triggering mechanisms (Degruyter and Huber, 2014; Bachmann and Huber, 2016; Cashman et al., 2017; Huber et al., 2019; Sparks et al., 2019). Glacially driven surface loading and unloading has been considered as an external eruption-modulating mechanism. For example loss of an ice sheet can promote lithospheric decompression that enhances mantle melting and eruptive activity (Jull and McKenzie, 1996; Maclennan et al., 2002), extensive glacial erosion can cause decompression-induced stress changes on volcanoes that enhance eruptive activity (Sternai et al., 2016), and changes in the magnitude and rate of intra-crustal stress changes as ice sheets wax and wane can enhance or impede dike propagation and magma transport needed to produce eruptions (Jellinek et al., 2004; Geyer and Bindeman, 2011; Mora and Tassara, 2019; Wilson and Russell, 2020; Satow et al., 2021; Coonin et al., 2024).

Steady improvements in: (1) the calibration, application, and interpretation of a variety of mineral-melt thermobarometers (e.g., Putirka, 2008, 2016, 2017; Ridolfi et al., 2010; Wieser et al., 2022, 2023a,b; Boschetty et al., 2022; Cutler et al., 2024; Weber and Blundy, 2024), (2) volatile concentration estimates from melt inclusions (e.g., Rasmussen et al., 2022), and (3) thermodynamic phase equilibrium modeling (e.g., Gualda et al., 2012, 2019) have increased the resolution for depths of magma storage and melt extraction beneath continental arc volcanoes (e.g., Huber et al., 2019; Wieser et al., 2023c). These tools now enable the exploration of whether ice loading and unloading over time impacts where magma stagnates, cools, and differentiates within the plumbing system, and whether, or not it can ascend to erupt (e.g., Rocchi et al., 2024).

In Iceland, where the lithosphere is exceptionally thin, decompression melting is dominant, and ice loading strongly influences mantle melt production and volcanic output (Sigvaldasson et al., 1992; Jull and McKenzie, 1996; Eksinchol et al., 2019; Maclennan et al., 2002; Licciardi et al., 2007). Along mid-ocean ridges (Stevens et al., 2016; Huybers and Langmuir, 2017) and island arcs (Nakada and Yokose, 1992; Sternai et al., 2016; Satow et al., 2021; Stewart, 2018), sea-level changes have been invoked to explain shifts in both the rate and style of eruptions. We focus here on continental volcanic arcs that are distinguished by construction on thick lithosphere and which in higher latitudes can be buried under extensive ice sheets (Watt et al., 2013). In contrast to Iceland or ocean island arcs, the rates and compositions of eruptions from continental volcanoes—responsible for 90 % of subaerial volcanism globally and posing a major hazard—are likely modulated by changes in crustal magma storage and transport rather than mantle melt production (Jellinek et al., 2004; Huber et al., 2019; Townsend and Huber, 2020; Wilson and Russell, 2020; Rasmussen et al., 2022). This does not impy that variation in the flux of mantle melt into the lower crust, advocated for by Till et al. (2019), is unimportant, but rather acknowledges the complexity of magma transport and differentiation within trans-crustal magma plumbing systems that could be affected by external triggers including a sudden change in surface load (e.g., Cashman et al., 2017). Whereas individual arc volcanoes clearly reflect impacts of multiple glacial cycles (e.g., Singer et al., 1997, 2008; Bacon and Lanphere, 2006; Conway et al., 2015; Moreno-Yaeger et al., 2024), systematic studies (e.g., Conway et al., 2023) are few.

The synchronicity of volcanic and climate events has been examined using global and regional records (Glazner et al., 1999; Jellinek et al., 2004; Nowell et al., 2006; Huybers and Langmuir, 2009; Geyer and Bindeman, 2011; Kutterolf et al., 2013; Watt et al., 2013; Rawson et al., 2016). These efforts comprise statistical analysis of terrestrial eruptive frequency patterns during deglaciation following the last glacial maximum (LGM) at ~18 ka [ka = thousand years ago; kyr thousand years duration], with limited investigation of longer records in marine sediments and ice cores (Kutterolf et al., 2013; Nyland et al., 2013; Schindlbeck et al., 2018). Moreover, the focus has mostly been on changes in eruptive rate following unloading and whether, or not, such rate increases are detectable (Jellinek et al., 2004; Watt et al., 2013; Conway et al., 2023). However, these approaches neglect several aspects of how trans-crustal multi-phase magma plumbing systems operate. For example, long term (10^5–10^6 yr) mantle and lower crustal inputs produce and incubate upper crustal magma reservoirs that evolve thermo-mechanically on much shorter timescales (10^2–10^4 yr) and only occasionally erupt (Bachmann and Huber, 2016; Till et al., 2019; Huber et al., 2019; van Zalinge et al., 2022). Feedback between host rock rheology and the P-T-X of magma bodies can play a key role in controlling melt extraction and eruption (Cashman et al., 2017; Huber et al., 2019). We thus expect that external forcing, by way of rapid ice retreat, propels complex responses in underlying magma plumbing systems that can vary among adjacent long-lived composite volcanoes. Characterizing this coupling that affects the pre-eruptive evolution of magma will enhance understanding of the earth system while providing new insights on volcano evolution and hazards (Aubry et al., 2022).

2. Avenues forward

Advancing understanding of how changes in the climate system affect the continental lithosphere and its magma plumbing systems requires integration of field observations, petrological and geochemical analyses, and modeling. The observations include precise volcano chronologies that underpin growth and erosion rate estimates (Conway et al., 2023)—coupled with thermobarometry to assess changes in magma storage and extraction depths over time, together with geometrically accurate records of the growth and retreat of ice sheets and glaciers across a region (e.g., Davies et al., 2020). Numerical modeling can address the dynamics of ice sheets and topography (e.g., Åkesson et al., 2018; Cuzzone et al., 2019, 2024; Seguinot et al., 2016; Ugelvig et al., 2016; Sternai et al., 2016), and crustal stress changes in response to surface loading (e.g., Albino et al., 2010; Moon et al., 2017). Thus far, models of how ice sheet growth and retreat impact magma transport in continental volcanic arcs employ thin-plate bending of the lithosphere under glacial loading to assess how and whether stress changes promote either the ponding of magma in reservoirs, or its ascent in dikes (Rawson et al., 2016; Mora and Tassara, 2019; Wilson and Russell, 2020; Rocchi et al., 2024; Fig. 1).

Building upon these models requires: (1) accounting for thousands of meters of topography in glaciated volcanic arcs and the intricacies of how ice sheet thinning and retreat within such a landscape proceed over time following glacial maxima, and (2) consideration of the mechanics and dynamics of magma reservoirs and magma transport through the crust. The crust acts as a non-linear filter for magma transported between the mantle and the surface. The complexity of that filter is rooted in the rheological response of the crust to buoyant and/or pressurized magmas transiting through it. Understanding the conditions that favor magma storage and accumulations and modulate eruption characteristics through time requires a deep understanding of mechanics (magma and crust rheology, fracture and dike dynamics) as well as the internal dynamics of magma storage regions (phase separation and differentiation; cooling, crystallization and volatile exsolution). We posit that progress along these directions is rooted in two main efforts. The first effort lies in the integration of disciplines to capture the coupling between surface dynamics and magmatism. It involves integrating field mapping, geochronology, petrology and geochemistry with ice sheet reconstruction and associated sediment erosion and deposition modeling into a multidisciplinary set of constraints. The second effort requires the development of models that couple magma transport to magma chamber (storage) dynamically to understand whether external forcings constrained by this integration are sufficient to affect the eruption history of a magmatic system and how.

The perspectives presented in this paper leverage emerging findings regarding ice forcing in continental arc magma plumbing systems gleaned from ongoing research that includes a novel blend of field constraints including: geochronology of pre-, *syn*-, and post-glacial eruptive products, glaciovolcanism and use of ice-lava contact features, magma composition and storage conditions, and surface exposure chronology to assess ice sheet retreat. These observations can be used to inform and evaluate numerical model simulations of: ice sheet growth and retreat, mass redistribution by erosion and deposition, evolution of intracrustal stress, magma reservoir evolution and pressurization, and reservoir failure leading to magma transport and eruption. Our

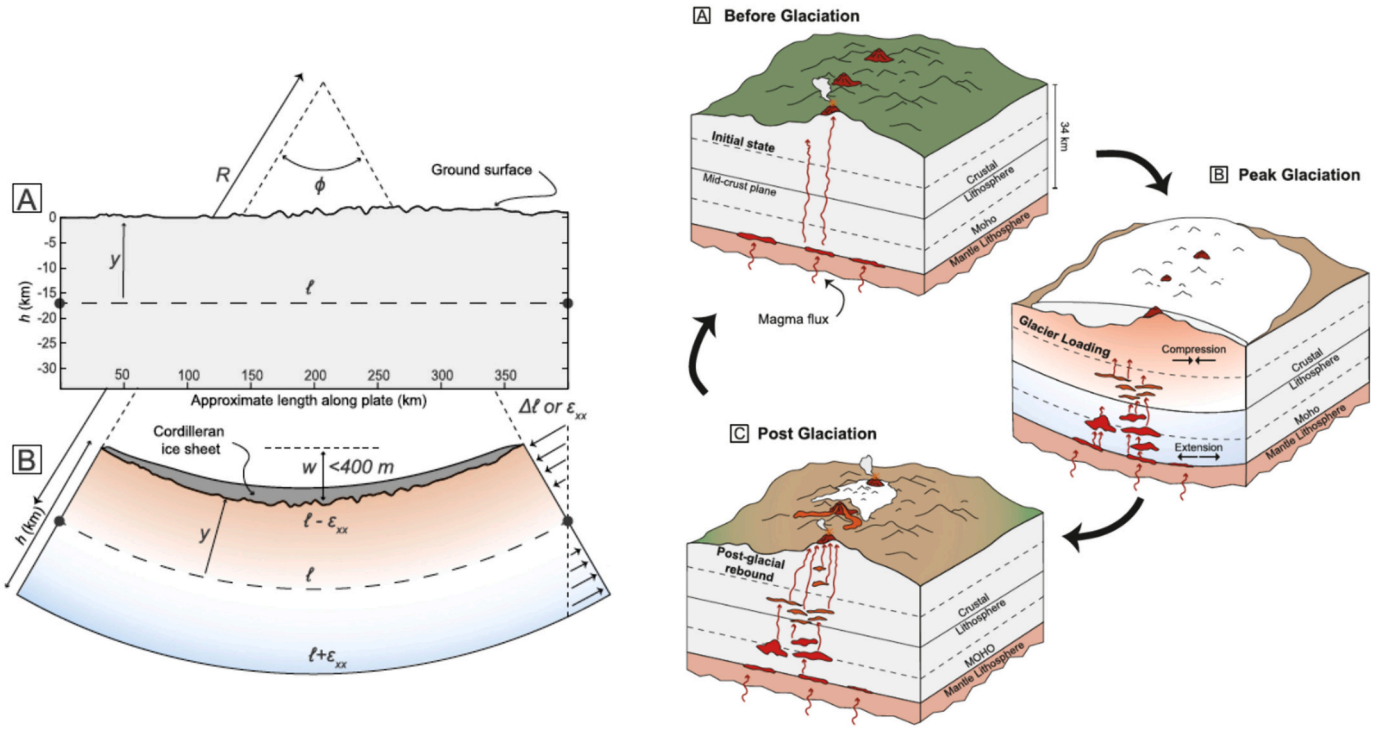

Fig. 1. Left panels: schematic of cylindrical plate-bending model employed by Wilson and Russell (2020) for the northern Cascade arc in Canada. As the Cordilleran ice sheet is loaded onto the plate, bending extends the lower crust and contracts the upper crust, thereby inducing magma ponding in the lower crust, and inhibiting magma ascent through the upper crust. Right panels: Conceptual model of glacial pumping of a magma charged crust resulting from loading and unloading of ice using the plate-bending model on the left (from Wilson and Russell, 2020). A) Prior to glaciation with the crust in a relaxed state. A background number of eruptions occur, reflecting the steady, long-term supply of magma to the crust. B) Glacial build-up invokes compression in the upper crust and extension in the lower crust as illustrated in the mechanical model at the left. This encourages ponding of magma in the crust due to arrested dike ascent and an overall reduction in eruptions. C) Immediately following deglaciation, relaxation of accumulated stress in the crust releases magmas stored in the upper part of the crust resulting in an increase in eruption rate.

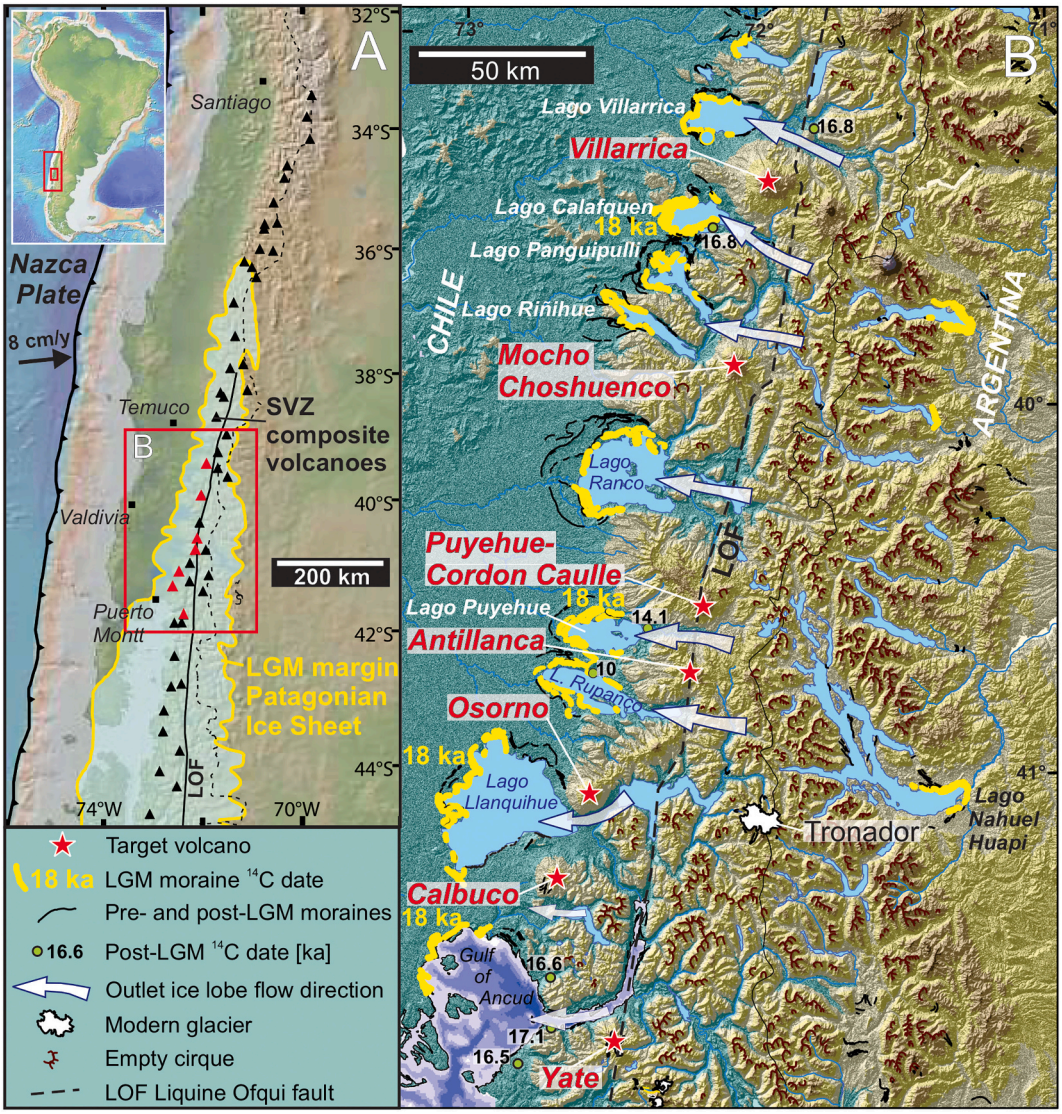

Fig. 2. A. Patagonian ice sheet extent during the local LGM; target volcanoes red triangles. B. Yellow lines: moraines deposited 23.0–17.8 ka which impound large proglacial lakes; those marked 18 ka are associated with many ^{14}C dates (modified from Davies et al., 2020). The arrows indicate flow paths of throughgoing streams of the Patagonian ice sheet (PIS) during the LGM westward from the Andean rangecrest.

integrated investigation of links between the cryosphere, topography and magmatism capitalizes on existing and newly acquired knowledge about ice-volcano interactions mainly within the Andean Southern Volcanic Zone (SVZ). An aim is to bring to light aspects that may make particular volcanic plumbing systems more, or less, sensitive to the impacts of glacially induced changes in surface loading and crustal stress.

3. The Andean Southern Volcanic Zone natural laboratory

Of the glaciated continental arcs, the Andean Central Southern Volcanic Zone (CSVZ, 37–41.5°S) is the strongest candidate in which to pursue our aims (Watt et al., 2013). This reflects a dense array of large composite arc front volcanoes, extensive and well-documented eruptive activity (Hickey-Vargas et al., 1989; Singer et al., 2008; Watt et al., 2011; Fontijn et al., 2014; Rawson et al., 2015, 2016; Naranjo et al., 2017; Alloway et al., 2015, 2017a, 2017b, 2022; Naranjo et al., 2017; Geoffroy et al., 2018; Mixon et al., 2021; Vander Auwera et al., 2021; Bechon et al., 2022; DeSilva et al., 2023; Moreno-Yaeger et al., 2024) and well-dated LGM glacial deposits (e.g., Lowell et al., 1995; Denton et al., 1999; Moreno et al., 2015; Fig. 2). In addition to its numerous volcanoes, many geophysical characteristics are relatively uniform, including the subducting plate age at the trench (<23 Ma), thicknesses of the crust, which decreases from about 42 km under Villarrica volcano to 35 km under Yate, and mantle wedge (Tassara et al., 2006; Hickey-Vargas et al., 2016). The base of the seismogenic zone is 12 km beneath the arc front, whereas local earthquakes extend to depths of 40 km beneath the forearc (Sielfeld et al., 2019), indicating the magmatic plumbing systems reside within thermally mature crust, which may explain the high eruption rates (Fig. 3).

Composite arc front volcanoes including from north to south: Villarrica, Mocho-Choshuenco, Puyehue-Cordón Caulle, Antillanca Volcanic Complex, Osorno, Calbuco, and Yate, have been impacted by growth and decay of Andean piedmont glacier lobes of the northernmost Patagonian ice sheet during the Late Pleistocene, with well-dated glacial deposits documenting maximum ice extents (Porter, 1981; Denton et al., 1999; Lowell et al., 1995; Kaplan et al., 2004; 2008; Glasser et al., 2008; Hein et al., 2010; Moreno et al., 2015; Davies et al., 2020). At its greatest extent, ice grew to thicknesses reaching from 1300 to at least 1900 m where it encased, in many instances, all but the uppermost flanks of

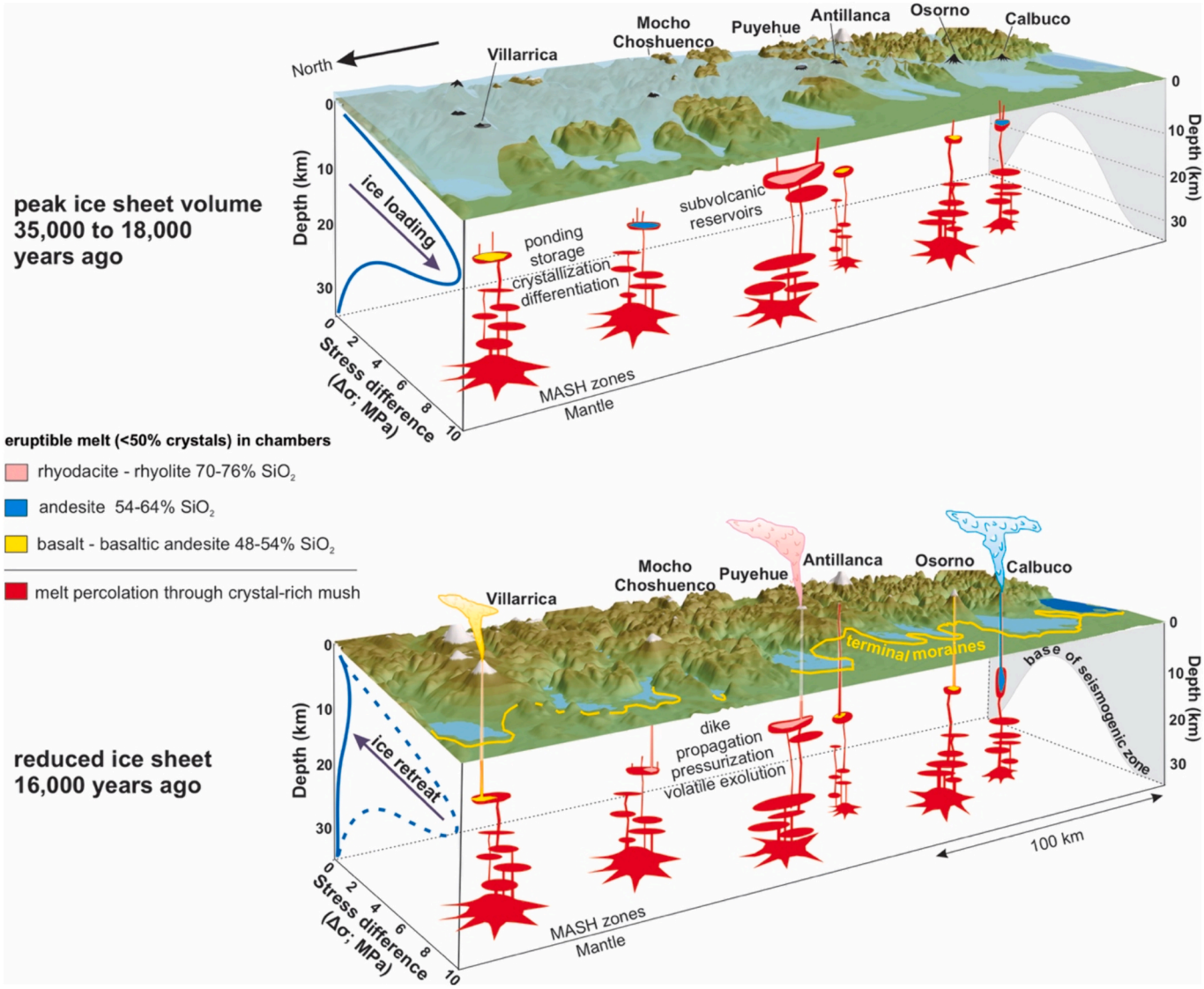

Fig. 3. Conceptual model for hypothetical volcanic responses along the Central Southern Volcanic Zone of the Andes to changes in ice loading from peak ice thickness during the local LGM between 35 and 18 ka, to nearly complete retreat of ice by 16 ka. During peak ice conditions, surface loading increases the lithostatic stress at depths where magma is stored within the upper portions of trans-crustal plumbing systems that perforate a 35 km thick crust. Upon rapid retreat of the Patagonian ice sheet, this stress drops by several MPa. Goals of our ongoing research in this continental magmatic arc are to determine: 1. How the composition, timing, and volume of eruptions vary from volcano to volcano during the last 50 ka and whether ice loading and unloading modulates the longer term melt flux from the mantle, 2. Whether some magmas and reservoirs are more sensitive than others to changes in surface loading and unloading by virtue of constrasts in melt composition, volatile contents, storage depth, or recharge rate, and 3. Mechanically how the stress drop may promote volatile exsolution, pressurization of stored magma, and dike propagation to fuel an increase in the number and volume of post-LGM eruptions.

these volcanoes (Figs. 2 and 3). Dated Patagonian ice sheet glacial deposits indicate that the last deglaciation began locally at 18 ka (Clark et al., 2009; Kaplan et al., 2008; Moreno et al., 2015). Moreover, the last deglaciation occurred very rapidly between 18 and 15 ka based on paleoclimate proxy records (Moreno et al., 2015), ^{14}C dating of the onset of tephra deposition and up-building of andic soil cover-beds with intervening tephra layers (Alloway et al., 2022), and ice sheet modeling detailed below (Cuzzone et al., 2024). The region has eight large (~20–40 km) proglacial lakes impounded by end moraines, that reflect the configuration of the various Andean piedmont glacier lobes. These former glacial lake basins (which have been repeatedly occupied over the Quaternary) are efficient sediment traps and thus sensitive recorders of geomorphic responses to glaciation and climate (Figs. 2 and 3; Andersen et al., 1999; Bertrand et al., 2005, 2008; Heirman et al., 2011). These features permit resolution of the histories of ice configuration and sediment redistribution over the last glacial-to-interglacial transition, and hence constrain the surface loading history.

For the target CSVZ arc-front volcanoes investigated by our team – temporal comparative analysis utilizing tephrochronology is fraught with difficulty on account of the paucity of LGM and older volcaniclastic cover-bed records as a direct consequence of pervasive glacial erosion and/or deep burial. Often the only cover-bed records preserved in, and adjacent to, these environments are of late Last Glacial and younger age (< 18 ka). These volcanoes have been mapped by Chile's Servicio Nacional de Geología y Minería (SERNAGEOMIN) and a coherent inter-regional post-LGM tephra record is emerging (Watt et al., 2011; Lohmar et al., 2012; Rawson et al., 2015; Fontijn et al., 2016; Naranjo et al., 2017; Geoffroy et al., 2018; Alloway et al., 2017a, 2017b, 2022; DeSilva et al., 2023).

Even less well documented are the chronology and petrology of effusive lava eruptions that span from pre-, to *syn*-, to post-LGM time as this was not the focus of the volcano-specific geochemical and petrologic

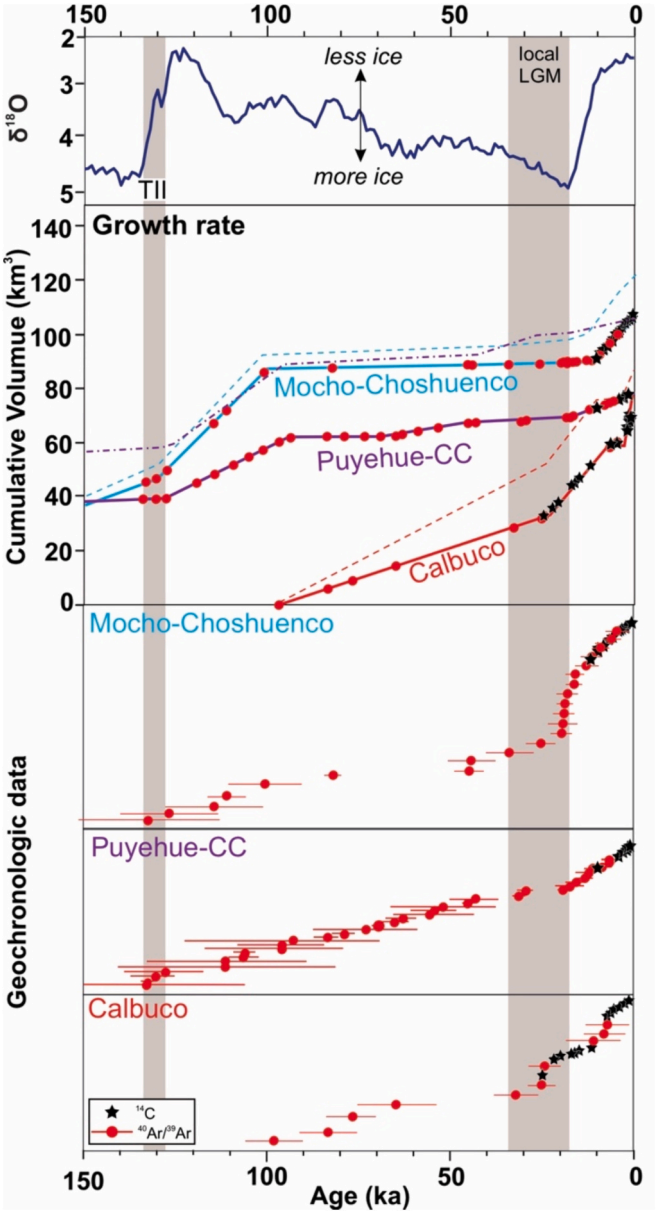

Fig. 4. Records of cumulative volume erupted over time from three composite arc front volcanoes in the Andean Southern Volcanic Zone (from Coonin et al., 2024). $^{40}Ar/^{39}Ar$ ages from effusive lava flows and ^{14}C ages for tephra deposits have been used together with field relations to estimate eruptive volumes and growth rates. Solid curves are minimum growth rates, dashed curves account for erosion (data from Singer et al., 2008; Mixon et al., 2021; Moreno-Yaeger et al., 2024). Comparison with the $\delta^{18}O$ marine proxy record for global ice volume (Lisiecki and Raymo, 2005) indicates that following both Termination II (TII, 127 ka) and the local Last Glacial Maximum (LGM, 35–18 ka), volumetric rates of eruption of volcanic products, including lava flows, and regionally-dispersed tephras, increased significantly.

efforts of Hickey-Vargas et al. (1989), McMillan et al. (1989), López-Escobar et al. (1995), Bechon et al. (2022), Vander Auwera et al. (2021), or Boschetty et al. (2022). A more complete eruptive record that includes lava flows is key to addressing the questions we aim to tackle. This requires many precise age determinations from lava flows in well-documented stratigraphic successions that are challenging but possible to date using $^{40}Ar/^{39}Ar$ and ^{3}He methods. We highlight below the geochronologic and petrologic measurements that, when acquired, can provide powerful first-order insights as to magma plumbing system behavior spanning the rapid transition from peak glacial to nearly ice-free conditions. Indeed, available chronologic data from Puyehue Cordón-Caulle, Calbuco, and Mocho-Choshuenco (Fig. 4) suggest that both effusive and explosive volcanic output along the CSVZ are sensitive to glacial-interglacial fluctuations in ice load.

4. Field and laboratory observations

Here we expand upon the sets of field observations, and geochronologic and petrologic data that are required to address how ice forcing impacts magma plumbing systems. We provide examples from our ongoing work in the CSVZ.

4.1. Eruption rates and volcano growth and erosion rates

It is hypothesized that glacial loading and unloading can impact magma plumbing systems, and hence eruptive outputs from composite arc volcanoes, in two principal ways. First, deglacial unloading may promote an increase in eruption frequency and volume by facilitating dike ascent (e.g., Singer et al., 2008; Watt et al., 2013; Conway et al., 2023). Second, ice loading can impede magma ascent causing it to pond, cool, and differentiate, thereby exerting a compositional effect on eruptive products (e.g., Rawson et al., 2016; Rocci et al., 2024). Using examples mainly from the CSVZ, we examine here some of the evidence for such impacts and demonstrate that despite the uncertainties, building detailed records of cone growth and petrologic changes that span one or more complete glacial-interglacial cycles can illuminate potential causal relationships during evolution of the cryosphere and underlying magma plumbing systems. Subsequently, we examine petrologic evolution of a spectrum of compositionally distinctive CSVZ arc front volcanoes where the chronology and growth rate records are most robust and discuss potential impacts of glacial loading and unloading on magma storage conditions.

Essential to understanding potential causal relationships between glaciation and eruption rates are accurate and precise chronologies, in concert with volumetric cone growth rate estimates, both of which are associated with uncertainties that can limit the ability to assess whether any feedback can be distinguished (Conway et al., 2023). To simplify their review, Conway et al. (2023) focus on age determinations close to the LGM and point to uncertainties in these few ages as being perhaps insufficient to recognize any change in eruption rate associated with the glacial-interglacial transition. Clearly, higher precision age determinations are desirable. Our current effort in the CSVZ capitalizes on improvements in $^{40}Ar/^{39}Ar$ mass spectrometers and analytical procedures expressly aimed at improving the precision and accuracy of ages determined from Late Pleistocene to Holocene lavas pursued in the WiscAr Geochronology Laboratory at the University of Wisconsin-Madison (Jicha et al., 2016; Martínez et al., 2018; Klug et al., 2022; Mixon et al., 2021; 2022; Moreno-Yaeger et al., 2024). We are also capitalizing on the ability to estimate the eruption ages of Holocene, minimally eroded mafic lava flows and scoria cones using surface exposure dating with measurements of cosmogenic ^{3}He in olivine (e.g., Moreno-Yaeger, in 2024; Doll et al., 2024). However, we argue here that simply compiling dates from lava flows to constrain growth rates is not enough. Of the seven composite arc front volcanoes we are investigating, geochronologic constraints of sufficient accuracy and precision so as to distinguish eruptions that occurred during the last glaciation (before 18 ka), from those that occurred during and after the rapid deglaciation between 18 and 15 ka, are currently available from Calbuco (Mixon et al., 2021), Puyehue-Cordón Caulle (Singer et al., 2008) and Mocho-Choshuenco (Moreno-Yaeger et al., 2024; Fig. 4). Importantly, our geochronologic work on these volcanoes also leverages extensive mapping and field observations regarding the stratigraphic context of the dated lavas as well as topographically-constrained volume estimates for packages of dated lavas, that are used to estimate volumes lost to erosion during particular periods of time. The cone growth curves for these three volcanoes are minimum estimates that consider erosive

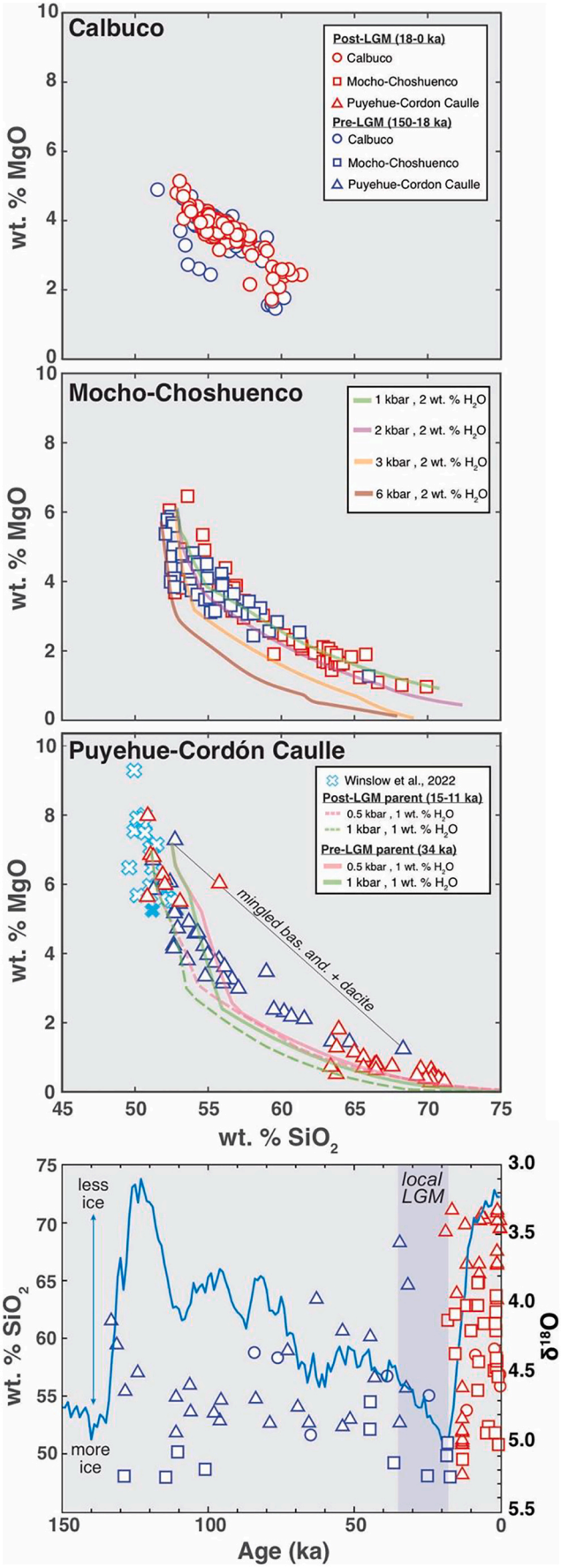

(caption on next column)

Fig. 5. SiO_2 vs. MgO for Pre-, and Post-LGM for lavas from Calbuco (Mixon et al., 2021), lava and tephra from Mocho-Choshuenco (Moreno-Yaeger et al., 2024; Rawson et al., 2016), and lava and tephra (Singer et al., 2008; Naranjo et al., 2017) and mafic enclaves in 2011 rhyolite; Winslow et al., 2022) from Puyehue-Cordón Caulle. Note that post-LGM compositions are distinctly different at each edifice. Calbuco compositions are monotonous and there is no shift in composition associated with the transition from pre- to post-LGM time. In contrast, at Puyehue Cordón Caulle compositions shift from mainly andesitic during pre-LGM time, to exceptionally bimodal following deglaciation. At Mocho Chochuenco a continuum of basaltic to rhyolitic compositions erupts throughout its history. For Mocho-Choshuenco and Puyehue-Cordón Caulle, alphaMELTS thermodynamic phase equilibrium models illustrate possible fractional crystallization of basaltic andesitic parent magmas to generate rhyolites. At Mocho-Choshuenco rhyolite can be produced at pressures between 1 and 2 kbar, whereas at Puyehue-Cordón Caulle the recent rhyolites can be generated via fractional crystallization at pressures less than 1 kbar. The bottom panel shows how the compositions erupted at each volcano have evolved over the last 150 kyr. The blue curve is global ice volume $\delta^{18}O$ proxy from Lisiecki and Raymo (2005).

losses and include estimated tephra volumes for the largest post-glacial eruptions (Fig. 4).

The growth history of Puyehue-Cordón Caulle volcano is constrained using forty-three $^{40}Ar/^{39}Ar$ ages of lava flows and ^{14}C dates for seven major post-LGM tephras (Singer et al., 2008; Fig. 4). Notably, after the LGM at about 18 ka eruptions became exceptionally bimodal, including some basalt interspersed with voluminous dacitic-rhyolitic lavas that contain between 2.5 and 3.2 wt% K_2O. Several of these relatively high-K_2O lavas yield age determinations spanning from 19 to 5 ka with 2σ uncertainties of only 1–3 kyr. Although reconstructions of the pre-LGM growth history have uncertainties, reasonable interpretations of volumes of preserved lava flow stacks that have been $^{40}Ar/^{39}Ar$ dated and that account for removal of lavas in glaciated valleys cut into these stacks imply that an early edifice grew rapidly (0.9 km^3/kyr) closely following the end of the penultimate glaciation at ~127 ka until about 96 ka (Fig. 4). Beginning at about 69 ka, the ancestral Puyehue cone then grew at an average rate of about 0.3 km^3/kyr, followed by a 60 % higher rate of growth at 0.5 km^3/kyr for the modern, post-LGM cone (Singer et al., 2008; Fig. 4). These growth rate estimates may have uncertainties of more than 25 % (Singer et al., 2008). However, we are reasonably confident that closely following the penultimate deglaciation ~127 ka, and the LGM at 18 ka, eruptive rates and cone growth at Volcán Puyehue increased by factors of between 100 and 50 %. This conclusion is consistent with analysis of the regional post-LGM tephra record which supports up to a two-fold increase in eruption rate in the 5 kyr following the LGM (Watt et al., 2013).

Volcán Calbuco has erupted a much narrower range of magma compositions (basaltic andesitic to andesitic; mostly 53–61 % SiO_2) compared to Volcán Puyehue (Castruccio et al., 2016; Arzilli et al., 2019; Morgado et al., 2019a, 2019b; Mixon et al., 2021; Vander Auwera et al., 2021; Romero et al., 2021; Fig. 5). Establishing an accurate long-term chronology for these K_2O-poor (0.5–0.9 wt%) eruptions is challenging with modern, low-blank, multi-collector mass spectrometry methods yielding $^{40}Ar/^{39}Ar$ age determinations from only 9 of 36 lava samples measured by Mixon et al. (2021). Notably, these age determinations range from 99 ± 12 to 9 ± 5 ka and represent the map units of Sellés and Moreno (2011) for which SERNAGEOMIN $^{40}Ar/^{39}Ar$ ages are as old as 340 ka, with the discrepancies likely reflecting unstable analytical blanks and single-collector mass spectrometer methods (Klug et al., 2022). The modern $^{40}Ar/^{39}Ar$ determinations imply a much shorter duration of volcanism and therefore much greater rates of cone growth than previously thought (Fig. 4; Mixon et al., 2021). Combined with ^{14}C dated tephra—in places intercalated with glacial sediment deposits—spanning from 19 to <1 ka, estimated volumes of post-LGM lava and tephra deposits total 26 km^3. Six $^{40}Ar/^{39}Ar$ dates younger than 26 ± 5 ka from upper portions of the edifice comprise another 26 km^3. Using

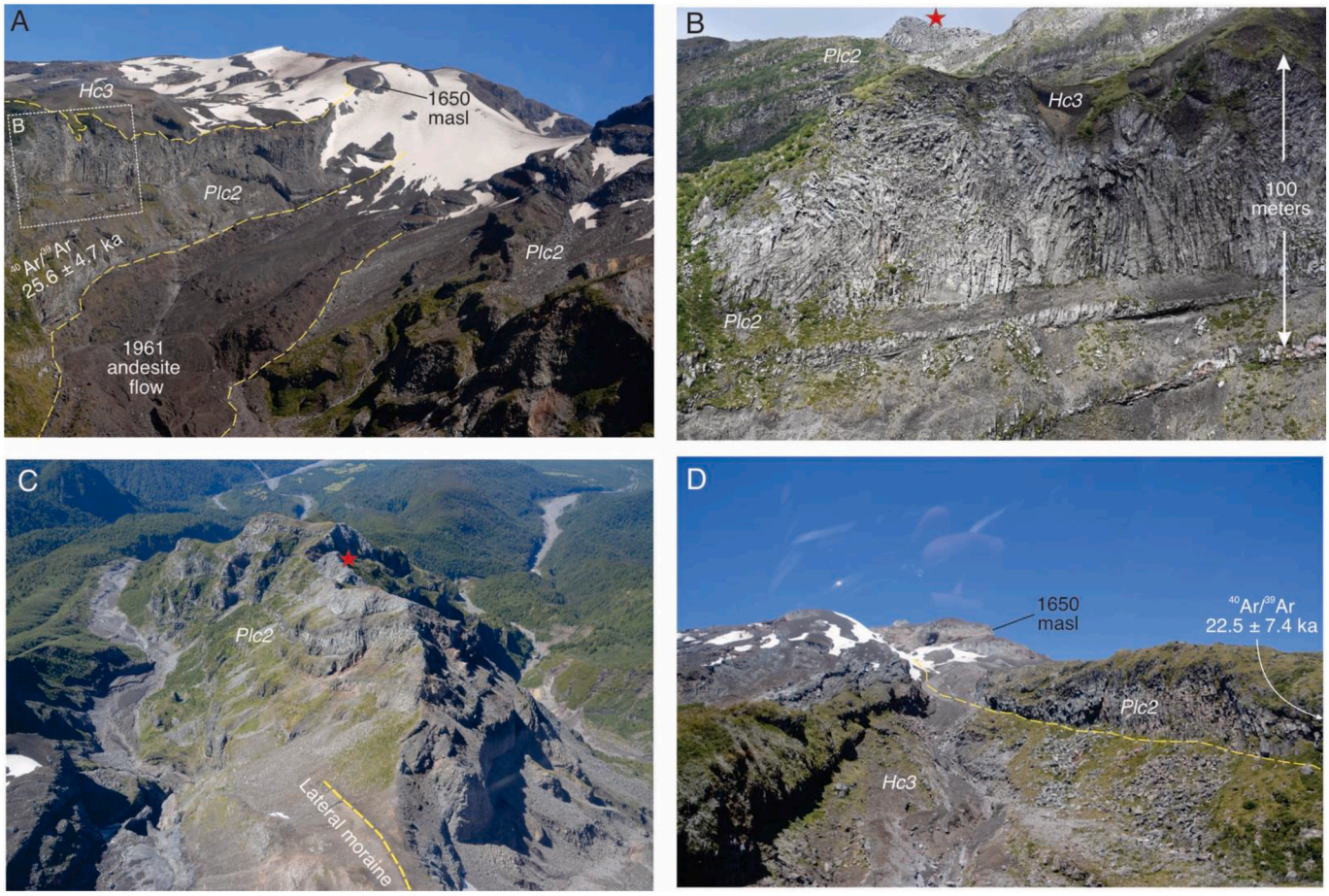

Fig. 6. Examples of chronologic constraints on ice configuration at Calbuco volcano. A. View from helicopter northward into valley walled by late Pleistocene andesite lava flows (map unit *Plc2*, overlain by Holocene lavas and tephra of unit *Hc3*) and floored by a lobe of the 1961 andesite lava flow. The stack of thick andesitic lavas comprising the west wall of the valley has been $^{40}Ar/^{39}Ar$ dated at 25.6 ± 4.7 ka (Mixon et al., 2021). Note that the flow thickens down valley and toward the valley axis. B. Photo westward from helicopter of of the area in panel A outlined in the dashed box. Note the vertical joints that flare upward into radial and sub horizontal joints. These features are consistent with lava flowing and cooling against glacial ice that occupied this valley at 26 ka during the local LGM. Modeling by Cuzzone et al. (2024) suggests that during the local LGM the PIS attained a thickness of >1600 m, consistent with the field relations illustrated here. C. View southward from helicopter of ridge comprising a stack of thick andesitic lavas to the west of those in panel A (red star in panel B shows common point) that thicken down valley and toward the axes of the valleys. These lavas, mapped as the same *Plc* unit and age as those in panel A, are interpreted as 'inverted' topography where the flows were impounded and cooled against ice that formerly occupied these valleys during the local LGM (Lescinsky and Sisson, 1998). A small lateral moraine at 1200 masl is interpreted as mid Holocene or neoglacial in age. D. View from helicopter eastward into valley walled on the south by andesitic lavas of map unit Plc2 that have been $^{40}Ar/^{39}Ar$ dated at 22.5 ± 7.4 ka (Mixon et al., 2021). As on the south flank of Calbuco volcano, these *Plc2* lavas thicken down valley indicating that they had been impounded and cooled against glacial ice during the local LGM.

this chronology, and considering modest and aggressive erosion rate scenarios, Mixon et al. (2021) demonstrate that the cone growth and eruption rate at Volcán Calbuco increased from less than about 0.5 km^3/kyr between 96 and 26 ka, to more than 2 to 3 km^3/kyr during post-LGM time (Fig. 4). A lacuna between about 55 and 30 ka wherein no lava flows are dated may reflect either suppression of eruptions as the Patagonian ice sheet thickened, or enhanced erosion by ice during this time that could bias the pre-LGM growth rate estimate (Mixon et al., 2021).

A remarkable feature of Volcán Calbuco is the preservation of several narrow ridges comprising steep stacks of thick andesitic lava flows, separated by several hundred-meter-deep glaciated valleys that radiate from the modern summit vent area. Many of these lavas thicken downslope and toward the adjacent valleys and display curvilinear to radial jointing indicating that flow was arrested by impoundment against glacial ice (Fig. 6). The $^{40}Ar/^{39}Ar$ ages for three of these lavas range from 25.6 ± 4.7 to 22.5 ± 7.4 ka indicating a series of eruptions closely associated with the transition from peak glacial to interglacial conditions that began at 18 ka. Some of these flows crop out well above 1400 m above sea level (masl) on the south and west flanks of Calbuco volcano and are interpreted to have flowed against valley glaciers that merged into a Patagonian ice sheet that was at least this thick prior to the onset of rapid retreat at ~18 ka (Fig. 6). Retreat of the Patagonian ice sheet left behind the inverted topography formed by ice-confined lava flows (Lescinsky and Sisson, 1998). This is but one example of how $^{40}Ar/^{39}Ar$ dating, in support of field observations, can provide direct evidence for the geometry of glacial ice that surrounded the large arc front volcanoes during the period of time shortly prior to rapid ice retreat following the local LGM.

Volcán Mocho-Choshuenco (Figs. 1 and 2) comprises 106 km^3 of basaltic andesitic to rhyolitic eruptive products (Fig. 5; Moreno-Yaeger et al., 2024). Based solely on the post-LGM tephra record, Rawson et al. (2016) hypothesize that changes in the eruption rate and the composition of magmas in the magma plumbing system beneath Mocho-Choshuenco are related to unloading of the Patagonian ice sheet. The Rawson et al. (2016) three phase model includes: large eruptions of long-stored SiO_2-rich magma from 13 to 8 ka (Phase 1), followed by refilling of the reservoir to produce small mafic eruptions from 7 to 3 ka

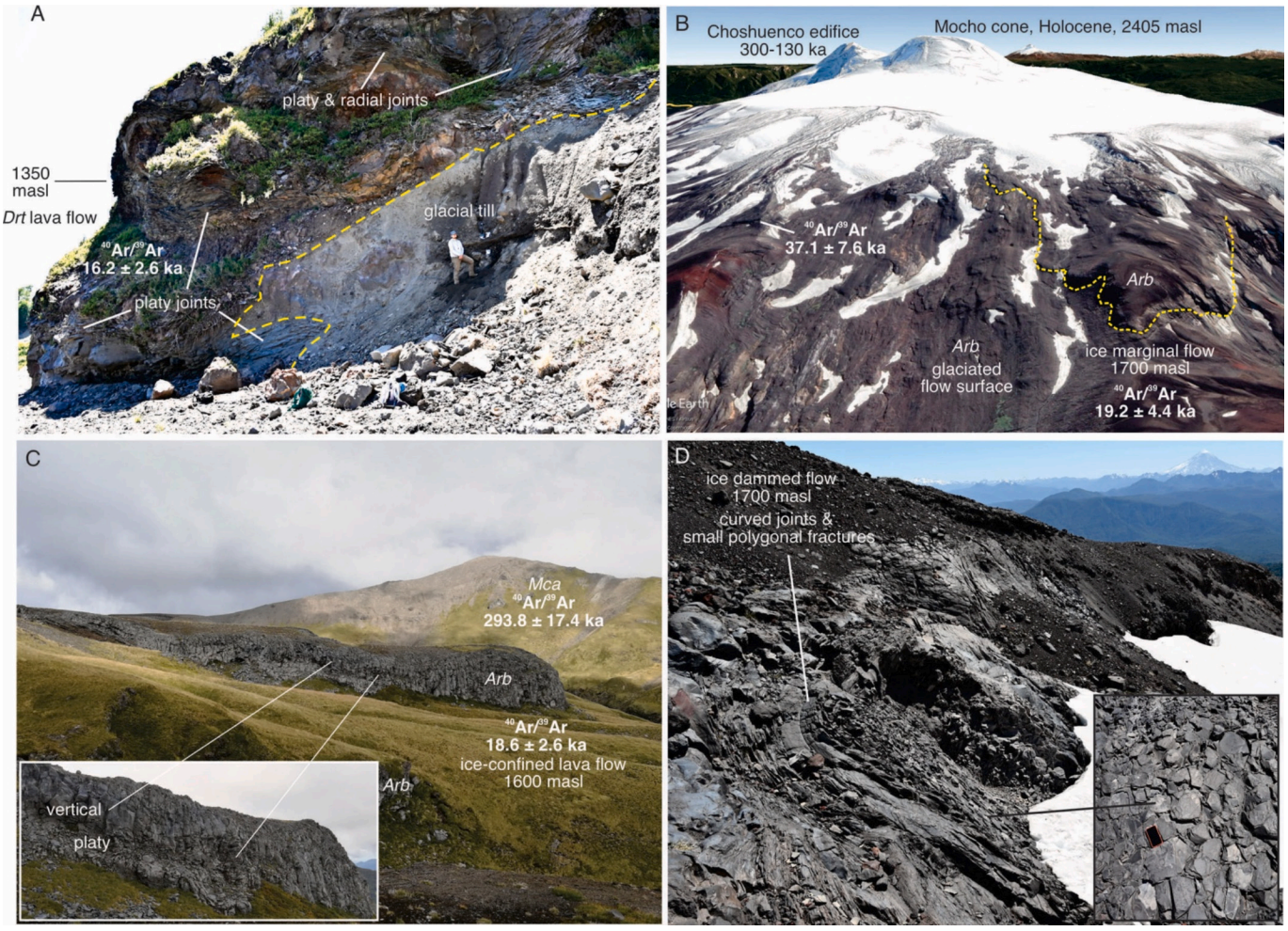

Fig. 7. Examples of chronologic constraints on ice configuration at Mocho-Choshuenco volcano. A. On the east flank of the volcano at 1350 masl dacitic lava flows thicken downslope, comprise irregularly oriented platy and radial joints, and in this outcrop, the lava flowed onto several meters of glacial till. Note the 1.8 m tall person for scale. This lava flow is $^{40}Ar/^{39}Ar$ dated at 16.2 ± 2.6 ka (Moreno-Yaeger et al., 2024). We interpret these field relations to reflect lava flowing into and cooling against the margin of the Patagonian ice sheet as it has begun to shrink rapidly between 18 and 15 ka. B. Google Earth view northward onto the upper southern flank of the volcano highlighting a lava flow $^{40}Ar/^{3}9Ar$ dated at 19.2 ± 4.4 ka inferred to have been impounded at an elevation of 1700 masl against the margin of the Patagonian ice sheet during the local LGM. C. On the west flank of the volcano, view to the south of a 30 m thick andesitic lava flow at 1600 masl that has been $^{40}Ar/^{39}Ar$ dated at 18.6 ± 2.6 ka (Moreno-Yaeger et al., 2024). This lava flow thickens downslope and comprises a platy-jointed base below subvertical joints. We infer that this flow was impounded against the margin of the Patagonian ice sheet during the local LGM (e.g., Smellie et al., 2011-see their Fig. 9). D. On the east flank of the volcano a dacitic lava mapped together with the lava in panel A as unit *Drt* exhibits curved jointing and small polygonal fractures (cell phone in the inset is 15 cm long) along its southern margin suggesting confinement by the Patagonian ice sheet at 1700 masl during the local LGM (e.g., Conway et al., 2015). The field observations and chronology highlighted here are consistent with modeling of the configuration of the Patagonian ice sheet during the last 25 ka (Cuzzone et al., 2024).

(Phase 2), culminating in an uptick in rate and andesitic activity since 2.4 ka (Phase 3). Because this model is only based on post-LGM tephra, Moreno-Yaeger et al. (2024) have acquired extensive new field observations on the effusive history via 24 modern $^{40}Ar/^{39}Ar$ age determinations of lava flows and two ^{3}He surface exposure ages. The findings, outlined briefly here, facilitate an examination of eruption rates and compositional evolution prior to, during, and after the local LGM that occurred between 35 and 18 ka. Moreover, a group of $^{40}Ar/^{39}Ar$-dated lava flows at elevations between 1350 and 1700 masl that give ages between 19.7 ± 3.2 and 16.6 ± 2.4 ka, many of which display platy, curved, or chaotic, arcuate or irregularly oriented (hackly) jointing, some of which are intercalated with glacial till, provide evidence for the height of the Patagonian ice sheet during the local LGM (Fig. 7).

As at Volcán Calbuco, the new $^{40}Ar/^{39}Ar$ dating has revised the chronostratigraphy and duration of volcanism based on previous work (Moreno and Lara, 2007), such that half of the volume of Mocho-Choshuenco has been erupted since 130 ka (Fig. 4; Moreno-Yaeger et al., 2024). In this work volumes of map units are calculated from a 12 m-resolution digital elevation model by measuring areas in a geographic information system with thicknesses from field and aerial drone observations (e.g., Fig. 11A). Volume estimates are based on eroded products and are hence minimum values. We estimate uncertainties of between 10 and perhaps up to 20 % on the volumetric growth curves at most time slices, particularly where dense arrays of radioisotopic ages have been determined (Fig. 4). On Mocho-Choshuenco, erosion is estimated by reconstructing pre-incision topography within extant incised valleys and applying $^{40}Ar/^{39}Ar$ ages, stratigraphic principles, and field observations to extrapolate the timing of incision onset. The average erosion rates in several radial valleys give a minimum volume removed from the edifice of about 13 km^3 over the past 300 kyr, with about 4.8 km^3 of that volume removed since 150 ka, and 0.34 km^3 since 18 ka (Moreno-Yaeger et al., 2024). The time-volume evolution of Mocho Choshuenco yields an average growth rate since 300 ka of about 0.4 km^3/kyr, similar to other

arc front volcanoes, but with prominent increases in volumetric eruptive output to 1.4 km^3/kyr or greater at about 130 ka, and again at about 13 ka, that closely follow the penultimate deglaciation and the LGM, respectively (Fig. 4).

Our findings at Mocho-Choshuenco expand upon those of Rawson et al. (2016) in several ways. First, there are lacunae between about 80 and 45 ka and 37 and 26 ka wherein few, if any, lavas are preserved, and the rate of cone growth was low between 45 and 18 ka (Fig. 4). A similar lacuna at Calbuco, and a relatively low rate of cone growth at Puyehue-Cordón Caulle, suggests that a regional factor—perhaps growth of the Patagonian ice sheet—rather than sampling bias, is involved. Interestingly, a parallel may be preserved at the 2640 m high Ruapehu volcano, central North Island, New Zealand at a similar southern latitude (39.28 °S), where a lacuna occurs between $^{40}Ar/^{39}Ar$-dated ice-marginal lava flows between about 45 and 20 ka (Conway et al., 2015). Moreover, we have discovered that both basaltic andesitic and dacitic lavas erupted extensively between 20 and 7 ka from an intricate set of magma reservoirs distinguished from one another by trace element contrasts (Moreno-Yaeger et al., 2024). Many of these lavas erupted during the local LGM when the Patagonian ice sheet was at its greatest thickness

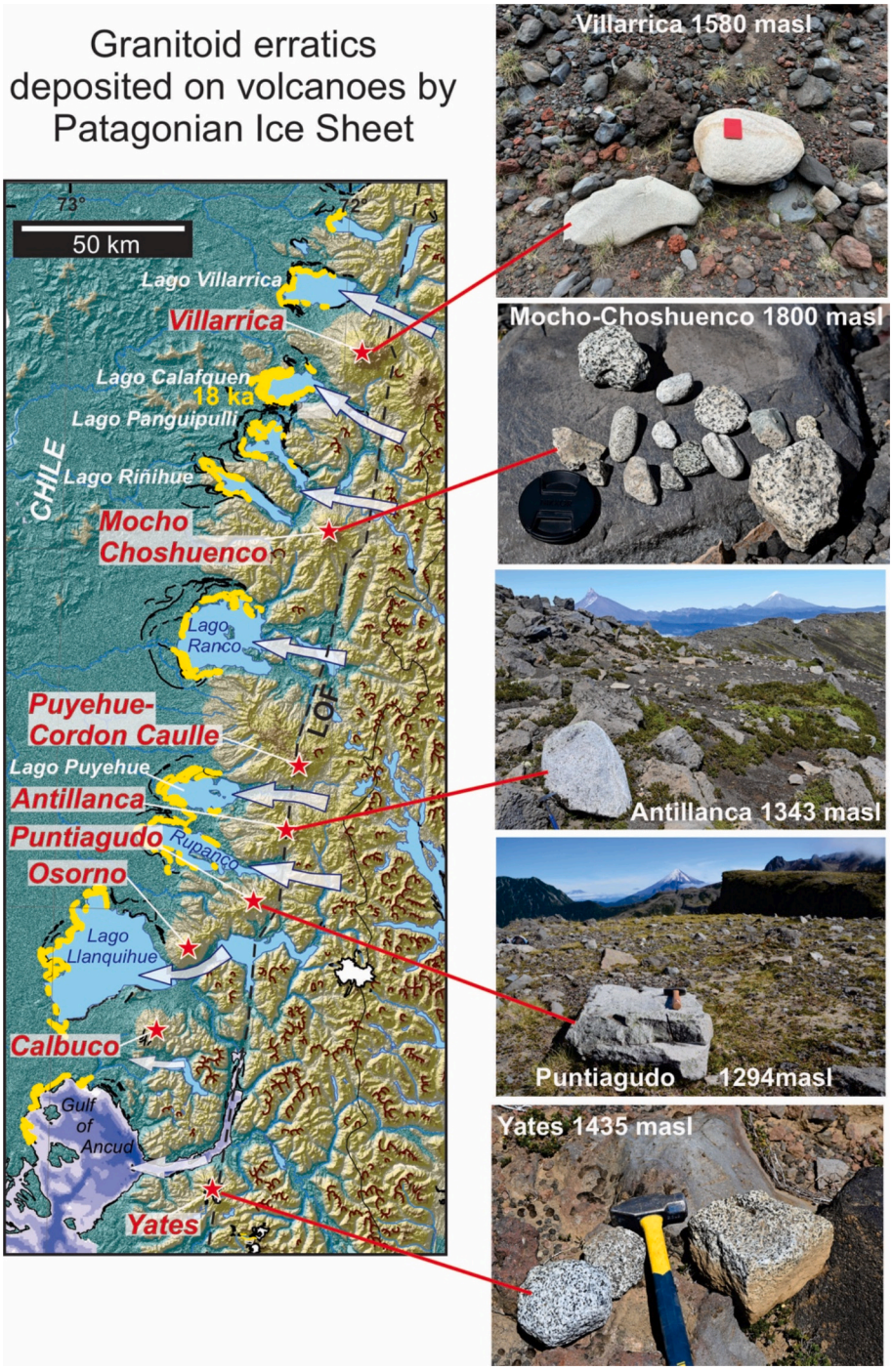

Fig. 8. Examples of erratic cobbles and boulders of various granitoid lithologies discovered on the eastern or southern flanks of several composite volcanoes. During the course of field campaigns from 2019 to 2024, erratics have been found in a band of altitude that varies among volcanoes. Erratics have been found at Villarrica between 1550 and 1900 masl on the south flank, at Mocho-Choshuenco on the east flank between 1650 and 1800 masl, at Antillanca between 1300 and 1343 masl, on Puntiagudo at 1290 to 1310 masl, and on the east flank of Yate volcano at 1430–1500 masl.

and extent (Fig. 4), thus reduction in surface loading is likely not the only factor in promoting the uptick in silicic eruptions at 12 ka featured in the Rawson et al. (2016) model. Notably, a dacitic lava dated at 16.6 ± 2.4 ka is truncated by a 3.5 km wide caldera from which the 5 km^3 rhyolitic Neltume Tephra was likely sourced at 12 ka (Moreno-Yaeger et al., 2024). The possibility that the rapid reduction in surface loading at the end of the LGM may have propelled volatile exsolution and pressurization of a modest-sized silicic magma reservoir, that led to dike ascent, roof failure, and caldera collapse, is the subject of ongoing investigation and is addressed in modeling below.

4.2. Glaciovolcanic constraints on ice sheet configuration

While extensive work, mainly in Iceland and British Columbia, document the characteristics of glaciovolcanic deposits (Smellie and Edwards, 2016; Edwards et al., 2020), much less work has been published on glaciovolcanic deposits within subduction zones. Exceptions to this are largely from New Zealand (Conway et al., 2015; Cole et al.,

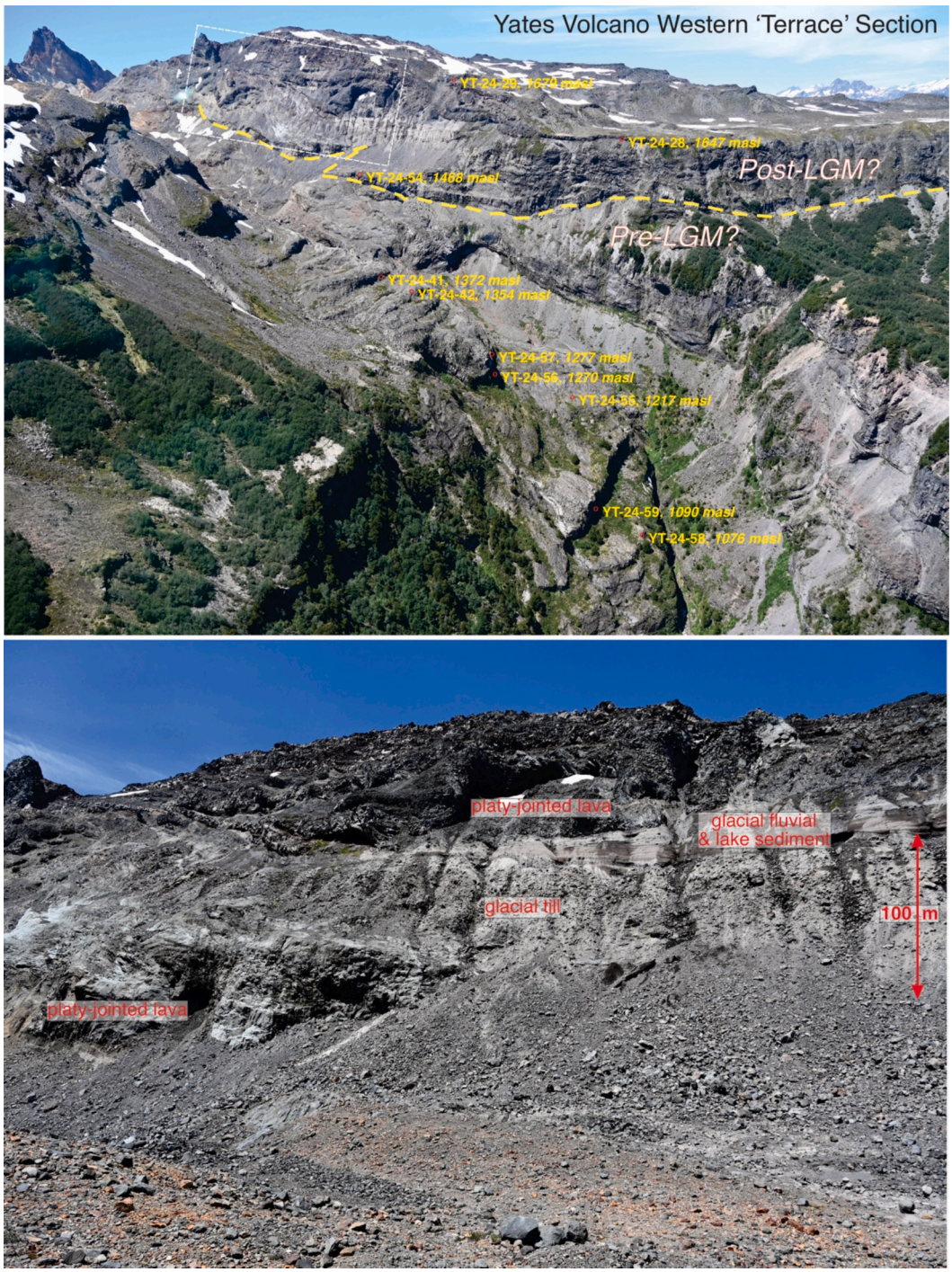

Fig. 9. Upper panel: View south from helicopter of a glacially excavated valley descending the west flank of Yate volcano (Fig. 2). From the deepest part of the valley in the photograph, to the the top of the ridge is about 700 m. A > 100 m thick wedge of glacial till and sediment is sandwiched between underlying lavas that dip westward and flat-lying lavas above. The lower panel is a close up of the area outlined in white box in the upper panel illustrating characteristics of the glacial sediments and bracketing lava flows.

2018) and the Cascades (Lescinsky and Sisson, 1998; Lescinsky and Fink, 2000; Kelman et al., 2002; Wilson et al., 2019), with limited observations from the Andes (Lachowycz et al., 2015). General references to subglacial deposits are indicated on map legends for some volcanoes in Chile, but detailed characterization and systematic mapping of glaciovolcanic deposits is sparse, and none have been documented from the volcanoes that are the focus of our current research (Figs. 2 and 3). Identification of volcano-ice interaction is particularly critical to our goals as it is the only approach that can link with certainty geochemical characteristics of volcanic units with the presence or absence of ice. Thus, identifying and characterizing volcano-ice contact features on CSVZ composite volcanoes is key to testing hypotheses developed from $^{40}Ar/^{39}Ar$ dating of eruptions and models of ice sheet configuration over time.

Many of the most characteristic deposits of glaciovolcanism that are interpreted to require the presence of impounded water generated via eruption-synchronous melting of an ice sheet, such as pillow lavas, palagonitized tephra and lava-fed deltas, are documented in basaltic deposits from Iceland (e.g., Bennett et al., 2009; Skilling, 2009) and British Columbia (e.g., Mathews, 1947; Edwards et al., 2020). Field-based studies at subduction zone volcanoes have generally relied on lava flow morphologies and patterns of jointing (Lescinsky and Fink, 2000) to identify potential glaciovolcanic deposits. We have highlighted above similar features within our target area (e.g., Mixon et al., 2021; Moreno-Yaeger et al., 2024; Figs. 6 and 7).

Notably, the lava flows on the east flank of Volcán Mocho-Choshuenco that have been $^{40}Ar/^{39}Ar$ dated to between about 20 and 16 ka display many ice-contact features (Fig. 7) that we interpret to result from growth of a lava-fed delta within a lake that formed along the margin of the Patagonian ice sheet between 1350 and 1700 masl (Moreno-Yaeger et al., 2024). Other novel observations that provide local constraints on the configuration of the northernmost Patagonian ice sheet include: (1) the occurrence of granitoid erratic boulders as a 'bathtub ring' deposit high on volcano flanks, (2) glacio-fluvial sediments interbedded with lava flows at high altitude on Yates and Mocho-Choshuenco volcanoes, as well as high altitude occurrences of: (3) pillow lavas, (4) lava-ice contact surfaces, (5) palagonite, and (6) ice-block melt-out cavities in lava flows.

Glacial erratics have been observed on several of the composite volcanoes within an elevational band ranging between about 1300 to 1900 masl (Fig. 8) and are interpreted as lodgement till that was deposited as the Patagonian ice sheet melted and thinned between 18 and 16 ka. Although this till could have been reworked during successive Pleistocene and Holocene glaciations, its current position in the landscape implies that the local thickness of the Patagonia ice sheet at this time of peak LGM extent was at least 1200 m regionally, and as much as 1900 m around the flanks of some volcanoes. The latter estimates are consistent with numerical modeling of the ice sheet discussed below.

A spectacular example of glacio-fluvial sediment deposited on, and buried by, late Pleistocene to Holocene lava flows is preserved between 1520 and 1650 masl on the west flank of Volcán Yate (Fig. 9). The package of coarser diamictite and overlying finer grained, well-sorted

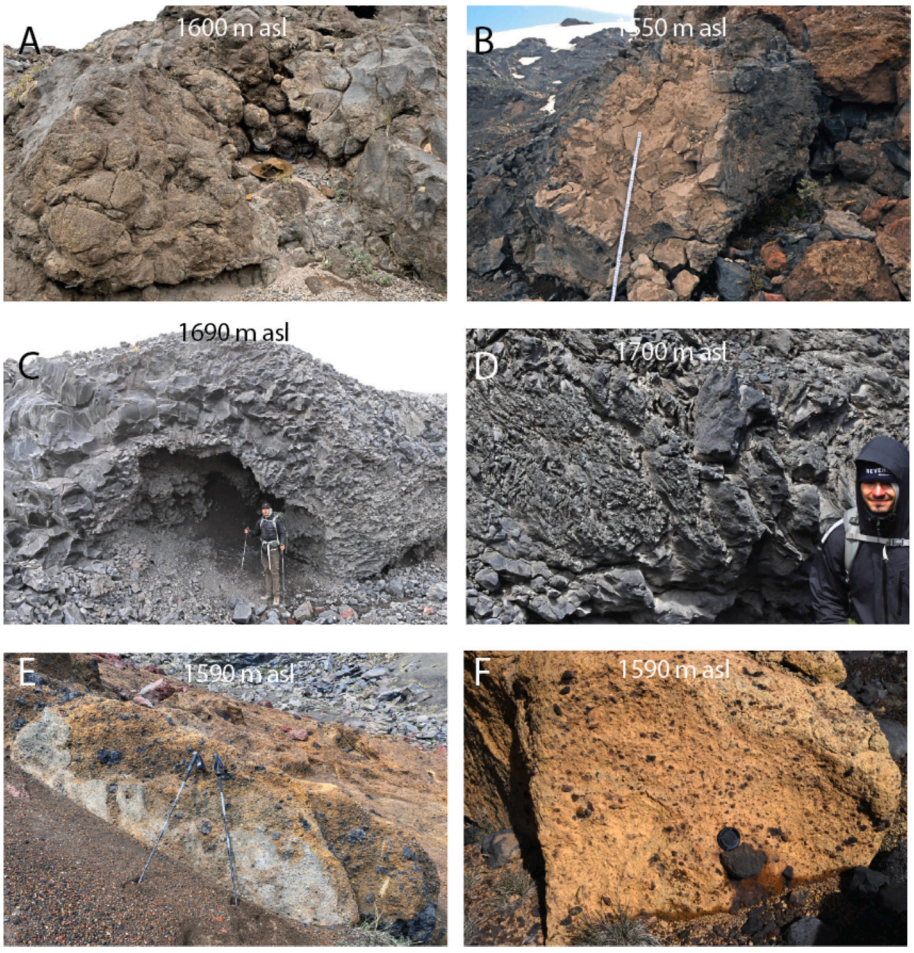

Fig. 10. Examples of features indicating lava-ice interactions at high altitude on volcano flanks. A. Pillow lavas on the southwestern flank of Villarrica volcano. B. Isolated pillow lava on the eastern flank of Mocho-Choshuenco volcano. C. Cavity beneath lava flow at Villarrica volcano interpreted to be an ice block melt-out cavern. D. Hackly and irregular lava surface textures indicative of direct ice contact, Villarrica volcano. E. Outcrop of palagonitized tuff-breccia, southern flank of Villarrica volcano. F. Palagonitized lapilli tuff block, southern flank of Villarrica volcano.

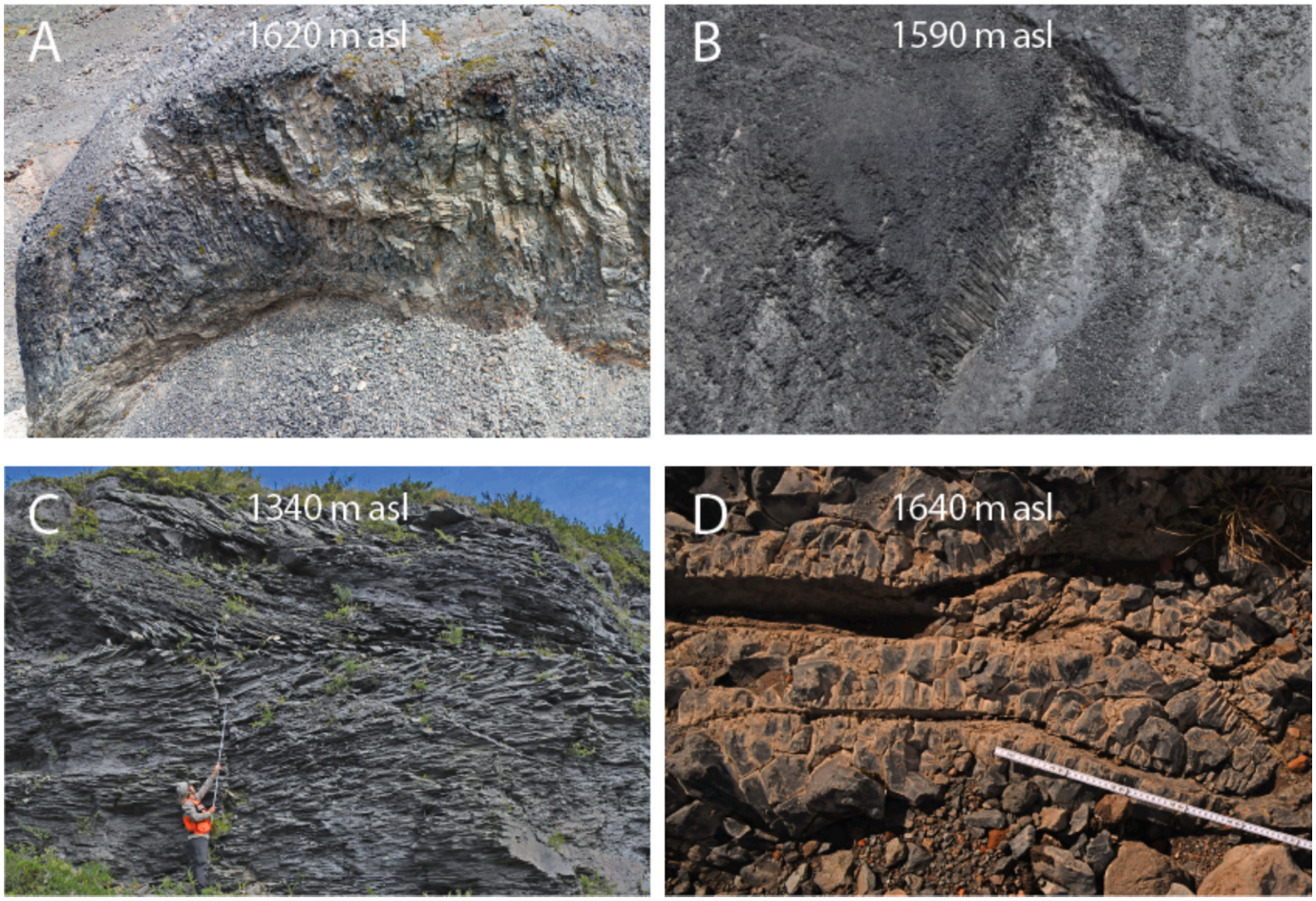

Fig. 11. Examples of lava jointing characteristics commonly indicative of lava-ice interactions observed high on the eastern flank of Mocho-Choshuenco volcano. A. Pervasively jointed 30 m high cliff of lava, B. Inclined columnar joints spanning 10 m across a lava flow edge, C. Pervasively platy joints in 16 ka lava D. Pseudo-pillow jointing.

glacial fluvial and lake sediments are similar to those described by Bennett et al. (2009) that formed as a result of subglacial eruptions at the Brekknafjoll–Jarlhettur volcanic complex in Iceland. This glacio-fluvial sediment package interfingers with, and is buried by, flat-lying lava flows that cap a broad ridge on the west flank of Volcán Yate. These flat-lying lava flows and the diamictite disconformably rest upon a package of thick lava flows that dip to the west (Fig. 9); the entire section through these lavas and the till is more than 700 m thick. We interpret the lower lavas to have erupted prior to the local LGM that began about 35 ka, and the upper lavas to have been erupted during and after retreat of the Patagonian ice sheet from the upper reaches of Volcán Yate, during which the till and glacial lake sediment were deposited in a glacially-impounded lake beginning at about 16 ka. This hypothesis can be tested by $^{40}Ar/^{39}Ar$ dating of the lava samples in yellow that span this section (Fig. 9).

Several 'classic' types of glaciovolcanic deposits, have also been observed high on the flanks of Villarrica and Mocho-Choshuenco volcanoes. Pillow-like lava lobes have been located on Villarrica (1600 masl) and Mocho-Choshuenco (1550 masl) volcanoes (Fig. 10A and B). Cavities defined by radial, narrow-width fractures at the base of lava flows occur on the western flank of Villarrica (1690 masl; Fig. 10C) and are interpreted as ice block melt-out features (e.g., Smellie et al., 2023). At another Villarrica location (1700 masl) lava surface textures are covered by glassy, hackly fractures (Fig. 10D) that we interpret to indicate direct ice contact emplacement similar to features documented in the 2010 Gigjökull lava flow (Björnsson, 2016). We have also documented the presence of palagonitized tuff breccia (Fig. 10E; Villarrica 1590 masl) and lapilli tuff (Fig. 10F; Villarrica 1590 masl). Moreover, a variety of fracture features ascribed to lava-ice contact are pervasive, including apparent ice-dammed lava cliffs (Fig. 11A, Mocho-Choshuenco 1620 masl) and sub-horizontal to radiating column joints (Fig. 11B, Mocho-Choshuenco 1590 masl), pervasive platy-jointing in lava interpreted to have been confined within sub-ice channels (Moreno-Yaeger et al., 2024; Fig. 11C), and pseudo-pillow joints indicative of the presence of water (Fig. 11D; Lescinsky and Fink, 2000).

5. Modeling ice, erosion, intracrustal stress, and magma reservoirs during deglaciation

5.1. Modeling northernmost Patagonia Ice Sheet (PIS) retreat

Given a limited number of geologic constraints on paleo-PIS extent and retreat, early ice sheet modeling efforts focused on reconstructing areal ice extent and volume of the PIS (Hulton et al., 1994; Sugden et al., 2002; Hubbard et al., 2005) in response to an inferred uniform temperature change during the LGM. Since these early efforts, geologic reconstructions of LGM and deglacial PIS behavior have improved (Davies et al., 2020) to a point where model-data comparisons can yield important constraints on the climate drivers of PIS change. More recent work using a newer generation ice sheet model (Yan et al., 2022) applied spatially varying temperature and precipitation fields from an ensemble of climate model simulations for the LGM. These results show that while the LGM temperature depression was largely responsible for the simulated areal extent and ice volume of the PIS most closely matching

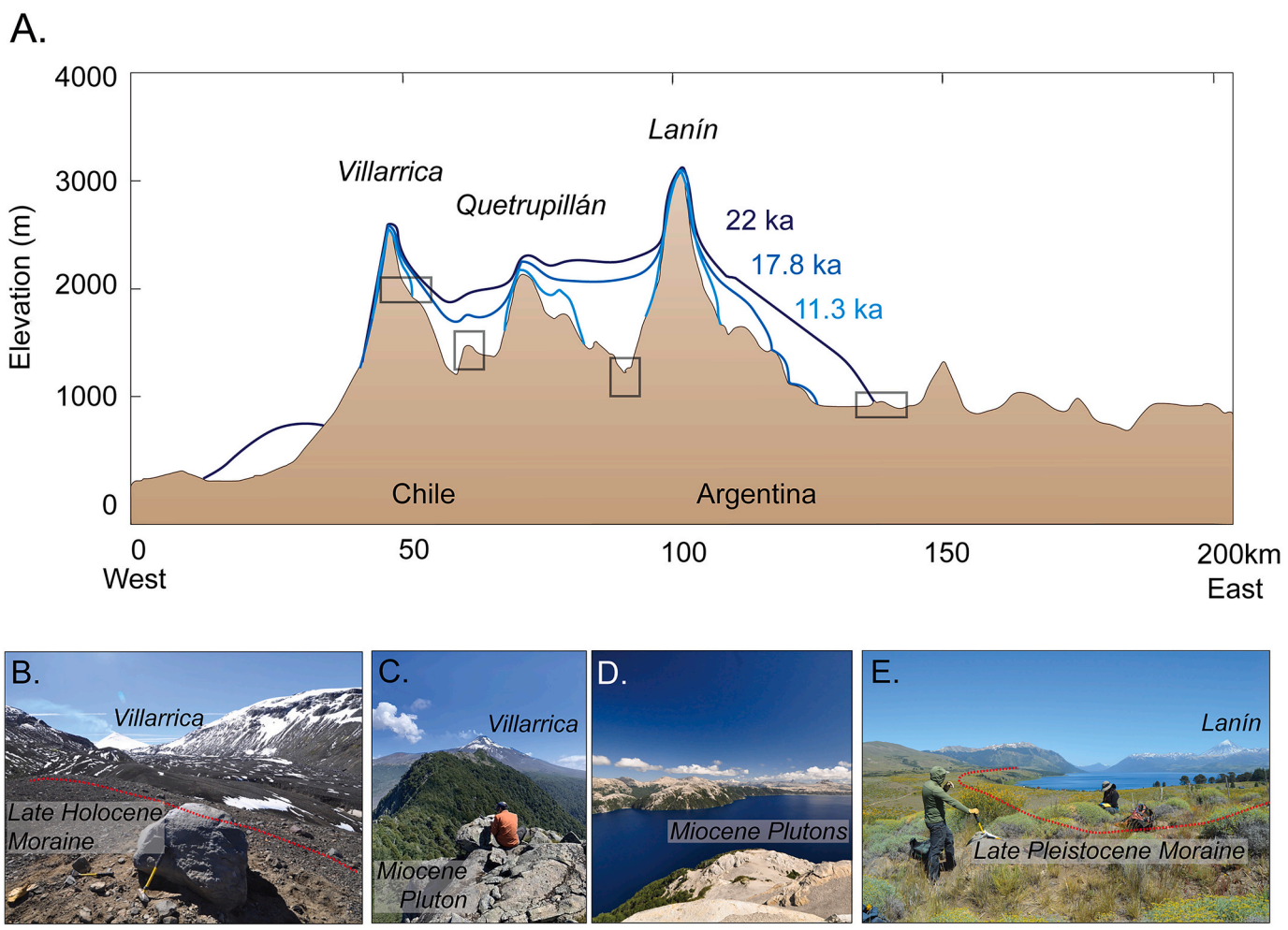

Fig. 12. Elevation profile of modeled Patagonia Ice Sheet (PIS) profile through time and geomorphic glacial features adjacent to the volcanoes. A. Topographic cross section of the PIS near three volcanoes in the CSVZ. Profiles are during the last glacial maximum (22 ka), the last deglaciation (17.8 ka), and at the beginning of the Holocene (11.3 ka), B. Photo of Late Holocene Moraine crest (dashed red line) on the southern flank of Villarrica Volcano, C. High elevation Miocene pluton outcrop near the southern flank of Villarrica volcano, D. Miocene plutonic outcrop at lower elevations between volcanoes, and E. View west toward Late Pleistocene moraines near the eastern flank of Lanín volcano straddling the Chile-Argentina border.

geologic reconstructions (Davies et al., 2020), variations in regional precipitation play an important role in modulating PIS extent. Regional ice modeling studies also suggest that variations in glacial and late glacial precipitation, driven by changes in large scale atmospheric circulation and associated latitudinal shifts in the Southern Westerly Winds (SWW), played a key role in PIS retreat and advance (Leger et al., 2021; Martin et al., 2019; Muir et al., 2023). Ultimately, where the existing synthesis of geologic reconstructions (PATICE; Davies et al., 2020) can be used to constrain deglacial changes in PIS extent, constraints on vertical ice thinning and volume are limited. Whereas ice sheet models can help fill gaps in our understanding of deglacial PIS thinning and volumetric changes, large-scale simulations of the deglacial response of the PIS are limited to a more regional and local scale.

Recently, Cuzzone et al. (2024) simulated the response of the PIS across the Chilean Lakes District (CLD) during the last deglaciation using the Ice Sheet and Sea-level System Model (ISSM; Larour et al., 2012). These numerical simulations were performed using a spatially varying high resolution model mesh that resolved bedrock features down to 450 m and resolved ice flow using higher order ice flow approximations (Dias dos Santos et al., 2022). LGM and deglacial changes in the PIS across the CLD were simulated by prescribing climate from a transient climate model simulation of the last deglaciation, TraCE-21 ka (Liu et al., 2009; He et al., 2013). During the LGM, ice thicknesses of up to 2000 m are simulated within the deep valleys of the CLD, with thinner ice cover <250 m simulated across the highest elevation peaks (e.g. volcanic peaks). Large-scale ice retreat began after 19 ka, and accelerated between 18 and 16.5 ka, coincident with deglacial warming (Fig. 12). Because geologic reconstructions of vertical ice thinning in this region are limited to non-existent at present, thickness and volumetric changes could not be evaluated in this study. However, the simulated areal extent was shown to agree well with early deglacial behavior reconstructed from PATICE (Davies et al., 2020), giving confidence that the ice sheet model simulations performed well in capturing geographic PIS retreat across the CLD. These simulations reveal that by 15 ka deglaciation across the CLD was largely complete, with only small ice caps and mountain glaciers remaining (Fig. 13). This simulated retreat history contrasts with the PATICE reconstruction during this interval (Davies et al., 2020), which suggests more extensive ice cover at 15 ka, before the PIS evolved into regional ice caps during the early Holocene. Unfortunately, limited geologic constraints on the ice history in this region, particularly during the late deglacial period, add large uncertainties to the PATICE reconstruction and model validation, and echoes a need for more additional constraints on past ice margin and ice thickness change to evaluate the ice modeling results. Nonetheless, the good agreement between the modeled ice retreat and the geologic reconstruction during the period of most rapid ice loss during the early deglaciation, it is reasonable to assume the ice model of Cuzzone et al. (2024) is capturing the large-scale ice thinning history with fidelity

(Fig. 13). Ultimately, climate forcing is critical for a more accurate simulation of deglacial ice retreat and remains one of the largest uncertainties in more accurately simulating the nature of deglacial PIS retreat. Cuzzone et al. (2024) finds that whereas deglacial warming controlled the overall retreat of the PIS across the CLD, modest variations in precipitation were able to modulate the rate and timing of deglacial ice retreat. This insight aligns with proxy data suggesting that during the LGM and early deglacial period, conditions were likely wetter across the CLD (Moreno et al., 1999, 2015, 2018) coincident with an intensification or equatorward shift of the SWW. More recent findings (Pesce and Moreno, 2014; Moreno, 2020; Díaz et al., 2023; Moreno et al., 2023, 2024) indicate that the transition out of the hyperhumid LGM involved a major decline in south westerly winds that led to an early termination westerly minimum, between 18 and 16.5 ka, with subsequent increases in westerly influence in pulses at 16.5 ka and at the onset of the Antarctic Cold Reversal (14.5 ka). While TraCE-21 ka simulated this increased precipitation in accordance with proxy records (Liu et al., 2009; He et al., 2013), the magnitude of this simulated change in precipitation was much less than inferred from precipitation proxies. Therefore, it is possible that larger anomalies in LGM and deglacial precipitation could have impacted the timing and pace of deglacial ice retreat more than is currently simulated (Cuzzone et al., 2024).

5.2. *Modeling evolution of intracrustal stress during deglaciation*

Understanding how deglaciation perturbs the state of stress where continental arc magmas are stored and transported is crucial for linking deglaciation to volcanism. Simplistic models assuming an elastic crust subject to the removal of a slab of ice yield varied predictions in the magnitude and distribution of decompression (~1–100 MPa in the shallow crust beneath the SVZ post-LGM; Rawson et al., 2016; Mora and Tassara, 2018). The significant difference in predicted decompression, up to two orders of magnitude, stems mainly from differing assumptions about crust rheology. Elastic half-space models suggest smaller pressure changes because the load is fully supported by elastic deformation of the crust (Rawson et al., 2016), while plate bending models assume the crust has a finite elastic thickness underlain by an inviscid fluid, leading to surface load accommodation through plate bending (Fig. 1; Wilson and Russell, 2020; Mora and Tassara, 2018). Although elastic thickness in volcanic settings can be locally thin (e.g., ~20–25 km beneath the SVZ – Pérez-Gussinyé et al., 2008), treating the lower crust and mantle as an inviscid fluid likely overestimates crustal flexure and decompression, especially over the short (~kyr) timescales of deglaciation. More realistic models consider viscoelastic behavior of the lower crust and mantle (Lucas et al., 2022; Nakada and Yokose, 1992; Kutterolf et al., 2013) and explore how the presence of melt-rich magma bodies locally modifies host-rock rheology and concentrates stress to potentially trigger magma reservoir failure (e.g. Lucas et al., 2022; Geyer and Bindeman, 2011).

The rheological behavior of the crust during deglaciation is also influenced by the geometry of the ice load. Currently overlooked in existing models is the role of bedrock topography in modulating the thickness of ice over volcanically active regions. In these areas, ice tends to be thinner atop volcano summits and thicker in the surrounding valleys (Fig. 12; Cuzzone et al., 2024). In addition, numerous geomorphic and volcanic processes may accompany deglaciation that contribute to the redistribution of surface mass, but few efforts go beyond accounting for the loss of ice (Sternai et al., 2016). Enhanced erosion rates, sediment and water redistribution, and the growth or destruction of volcanic cones as they respond to changes in surface cover can all perturb the state of stress at depth (Pinel and Jaupart, 2000; Sternai et al., 2016). Recent advances in modeling ice sheet dynamics (e.g., Cuzzone et al., 2024) and their effects on erosion and sediment redistribution (e.g., Jefferson et al., 2014), and refined chronologies of volcano growth (e.g., Singer et al., 2008; Mixon et al., 2021; Moreno-Yaeger et al., 2024), offer an opportunity to develop more realistic and location-specific models of crustal stress evolution at the scale of individual volcanic systems.

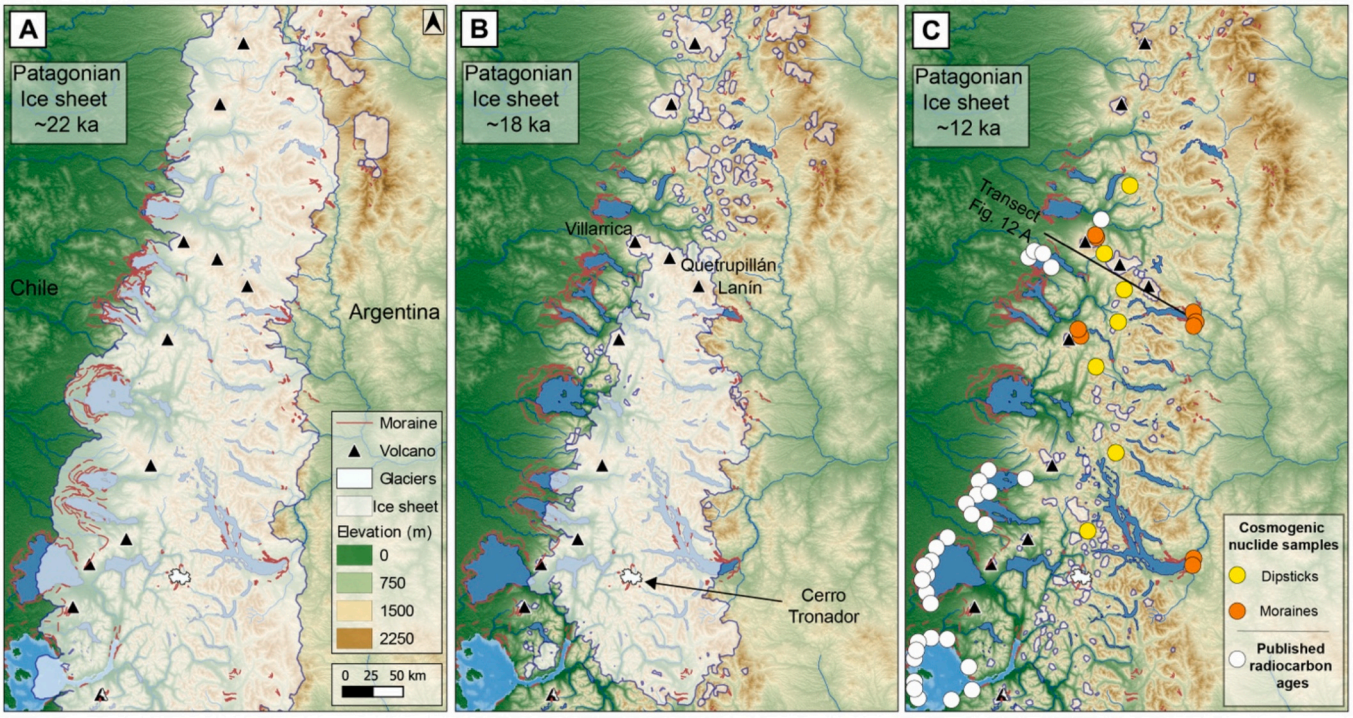

Fig. 13. Simulated Patagonian Ice Sheet (PIS) area (Cuzzone et al., 2024) and mapped and dated glacial deposits and features (Denton et al., 1999; Moreno et al., 2015; Davies et al., 2020). Simulated PIS extent at: A. 22 ka, B. 18 ka, and C. 12 ka. Mapped end moraines (red lines) and locations of published radiocarbon (white circles) and future surface exposure dates (yellow and orange circles) noted.

As a proof of concept, we simulate the load of the PIS from the model of Cuzzone et al. (2024); Fig. 14) as a distribution of normal tractions acting on the surface of an elastic half space (Boussinesq, 1885; Fig. 15). Following deglaciation at Mocho-Choshuenco, Puyehue-Cordón Caulle, and Calbuco, the resulting change in crustal mean stress is greatest in magnitude directly beneath the valleys where ice was thickest, with little to no change in mean stress in the upper ~1 km beneath the base of the volcanoes (Fig. 15). However, unloading from the sides of the volcanoes causes the magnitude of the mean stress change to increase with depth directly beneath the volcanoes, reaching a depth range of maximum change before decaying again with depth. The maximum magnitude of the mean stress change and the depth range at which the stress change peaks differ for the three volcanoes because they experienced different ice histories due to variations in their topography and geographic position beneath the PIS (Fig. 15). At Mocho-Choshuenco, the change in mean stress reaches −5.5 MPa at a depth range of ~9–13 km beneath the base of the edifice. At Puyehue-Cordón Caulle, the maximum change in mean stress is greater (−6.2 MPa) over a wider depth range (~6.5–17 km) because the volcano's lower relief and flatter summit region hosted thicker ice during the LGM. By contrast, the high relief and conical shape of Calbuco and its proximity to the western margin of the PIS imply thinner ice during the LGM and subsequently smaller changes in mean stress following deglaciation (−3.7 MPa from ~8–18 km depth beneath the edifice).

5.3. Crustal stress responses to cone growth

In order to contextualize the effect of ice loading on crustal stress and capture potential feedbacks between crustal stress change and volcanic activity, it is necessary to understand how volcanic activity itself can modulate stress at the shallow depths where subvolcanic magmas reside. The growth of a volcanic edifice progressively loads the crust and increases compressive stresses beneath the base of the edifice. Idealized elastic models for the change in horizontal normal stress in response to the load of a volcano were developed by Pinel and Jaupart (2000) by modeling the load of a volcano as a distribution of cylindrical slabs of infinitesimal thickness to approximate the load of a cylindrical cone. We apply this model to estimate the stress change during growth of Mocho-Choshuenco using eruption rates determined by Moreno-Yaeger et al. (2024). We idealize the Mocho-Choshuenco edifice as a cylindrical slab with a 5-km radius that increases in thickness over time according to the net cone growth rates determined in the sections above. We consider that tephras and other explosive deposits are too widely distributed and too easily eroded to contribute to the growth of the cone and use only the volume of erupted lavas.

By calculating the change in radial normal stress with depth beneath the edifice over different time periods, we can glean key insights about the role of edifice growth on crustal stress. Using a long-term average cone growth rate of 0.3 km^3/kyr for the past 300 kyr, we find that growth of the cone to its present-day size adds approximately 25 MPa of

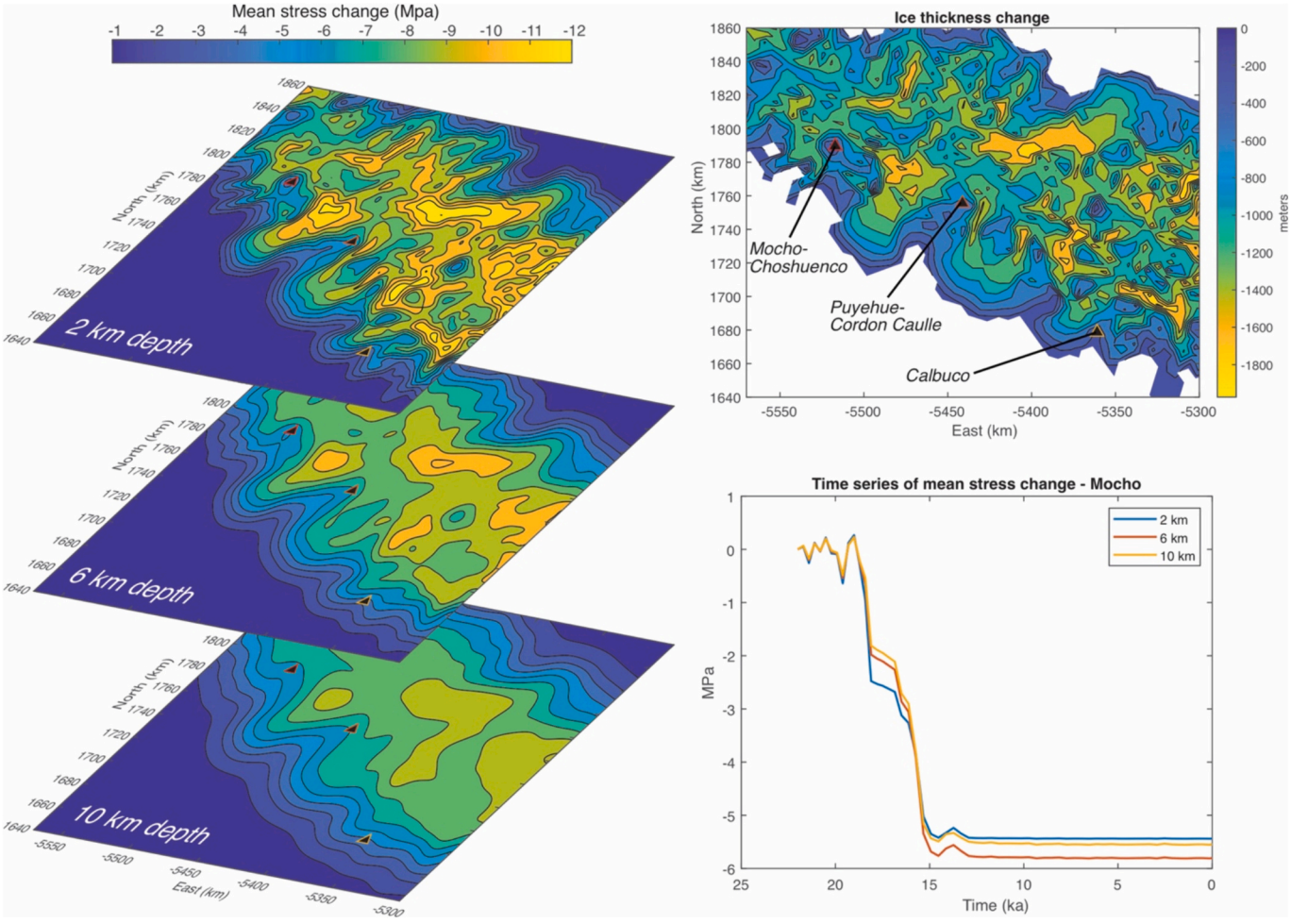

Fig. 14. Crustal stress model. Ice thickness change from the model of Cuzzone et al. (2024); Fig. 13) over 22 kyr is illustrated in the upper right panel. Lower right panel illustrates the mean stress change below Mocho-Choshuenco volcano at 2, 6, and 10 km depths shown in the stress maps in the left panels. Note that nearly all the stress change occurs during the rapid deglaciation between 18 and 15 ka predicted in the ice sheet retreat model of Cuzzone et al. (2024) and supported by geologic and geochronologic data.

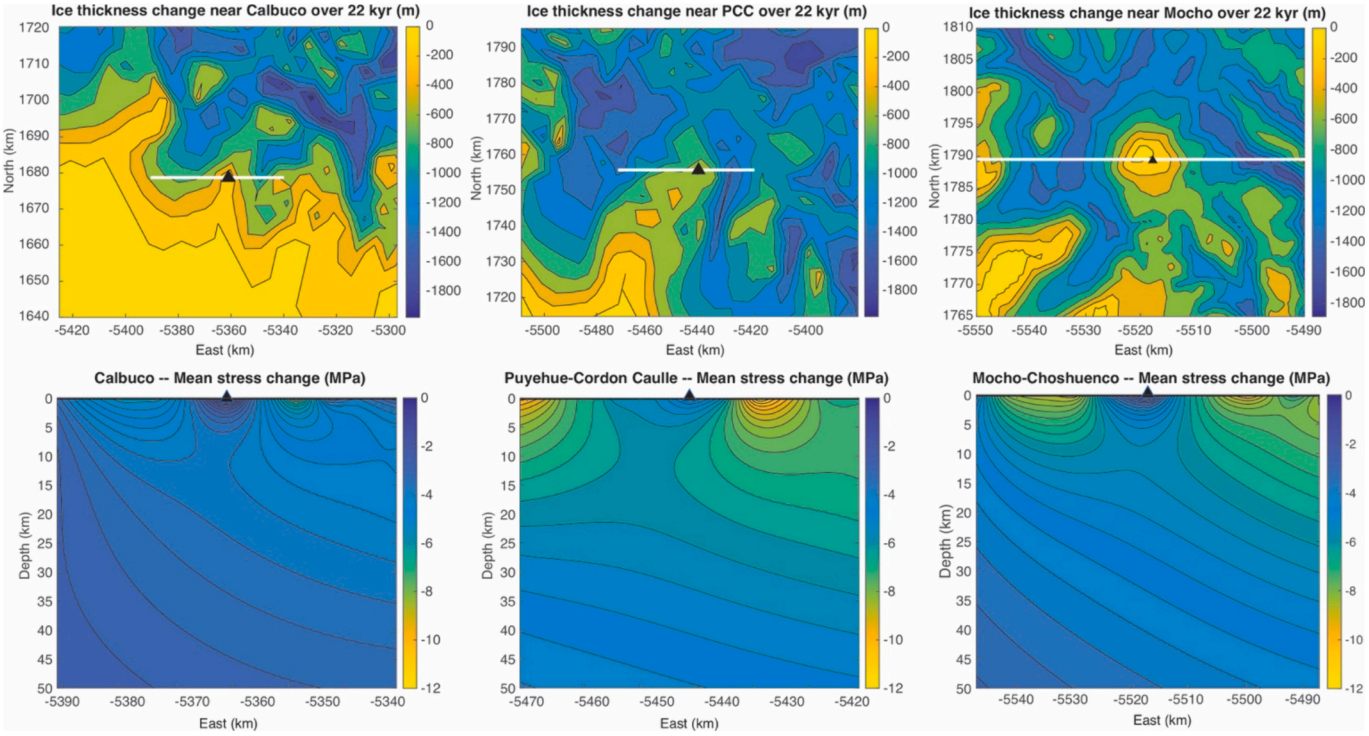

Fig. 15. Crustal stress model applied at Calbuco, Puyehue-Cordon Caulle, and Mocho-Choshuenco volcanoes. Top panels: depict ice thickness changes integrated over 22 kyr (Fig. 14) around each volcano. Bottom panels: depict mean stress changes below each volcano along the white cross section lines in upper panels. The map and depth profile for Mocho-Choshuenco are models generated at much higher spatial resolution than for the other two volcanoes.

compressive normal stress beneath the edifice, for a time-averaged rate of ~0.08 MPa/kyr (Fig. 16). However, during periods of accelerated cone growth, such as that following the penultimate glacial maximum between ~130–100 ka, stress change rates can reach ~0.3 MPa/kyr in the shallowest ~1 km beneath the edifice.

Compared to crustal stress change caused by deglaciation of the PIS, volcano growth is a much shallower perturbation to the crustal stress field and operates on a much longer timescale. The stress perturbation from cone growth decays over a depth range on the order of the radius of the volcano; for example, the stress change from growth of Mocho-Choshuenco appears to nearly vanish by ~6–8 km depth beneath the edifice. Thus, we can infer that volcano loading will primarily impact near-surface magmatic processes such as transport through dikes (Pinel and Jaupart, 2000, 2004), whereas the stress changes from PIS retreat may extend well into magma storage regions to modulate processes that occur there. In addition, the peak mean stress change due to retreat of the PIS is ~5.5 MPa in only ~4 kyr, for a rate (1.4 MPa/kyr) that is about one order of magnitude faster than even the most rapid cone growth (Figs. 14 and 15).

5.4. *Crustal stress responses to erosion and deposition of sediment*

Erosion of rock and deposition of sediment drive crustal deformation by redistributing mass across Earth's surface (e.g., Dalca et al., 2013; Ferrier et al., 2017), and thus have the potential to influence magma production, transport, and eruption, just as the growth and retreat of ice sheets do (Sternai et al., 2019). Relative to changes in loading driven by ice mass variations, changes in loading driven by erosion are amplified by the density of the eroded rock, which is ~3 times higher than that of ice. Calculating the degree to which this affects crustal stresses at a given volcano depends on the local history of sediment redistribution, which requires estimating the history of rates and patterns of erosion and deposition on and around the volcano (e.g., Jefferson et al., 2014). Here we describe an illustrative example from Mocho-Choshuenco to show how erosion and deposition can generate changes in crustal loading that are locally comparable in magnitude to ice-driven changes, following the analysis in Moreno-Yaeger et al. (2024).

Several observations suggest that Mocho-Choshuenco may have experienced significant changes in loading driven by erosion and deposition of rock and sediment. Deep valleys incised into the flanks of the volcano show the removal of large volumes of rock by erosion. Mocho-Choshuenco is mantled by young lava flows (Moreno-Yaeger et al., 2024), suggesting susceptibility to rapid erosion, as many young volcanic surfaces are elsewhere (e.g., Gayer et al., 2019). It was overrun by a temperate ice sheet during recent glaciations (Cuzzone et al., 2024), indicating that erosion may have been fast, similar to that in other settings (e.g., Koppes and Montgomery, 2009; Alley et al., 2019; Hallet et al., 1996). All of these suggest that the deep valleys on the volcano flanks may be locations of focused crustal unloading.

The sediment eroded from these valleys is transported by rivers toward floodplains upstream of lagos Riñihue, Panguipulli, Ranco, and Maihue, which are west, northwest, southwest, and south of Mocho-Choshuenco, respectively (Fig. 17). These lakes are glaciogenic and accumulate water and sediment from upstream catchments hundreds to thousands of km^2 in area (Laugenie, 1982; Van Daele et al., 2015), suggesting that the floodplains and lakes are locations of focused crustal loading.

To illustrate how large these sediment- and water-driven changes in loading may have been, we constructed a scenario of rock and sediment redistribution via erosion and deposition at Mocho-Choshuenco. For each valley incised into the flanks of Mocho-Choshuenco, we calculated a basin-averaged erosion rate by dividing the mass of eroded rock by the valley's drainage area and the duration of erosion. We estimated each valley's eroded rock mass as the product of valley volume and rock density, in which valley volumes were estimated by subtracting the present valley topography from pre-incision topography reconstructed from minimally eroded valley rims, following procedures adopted in volcanic landscapes elsewhere (Singer et al., 1997; Ferrier et al., 2013a,

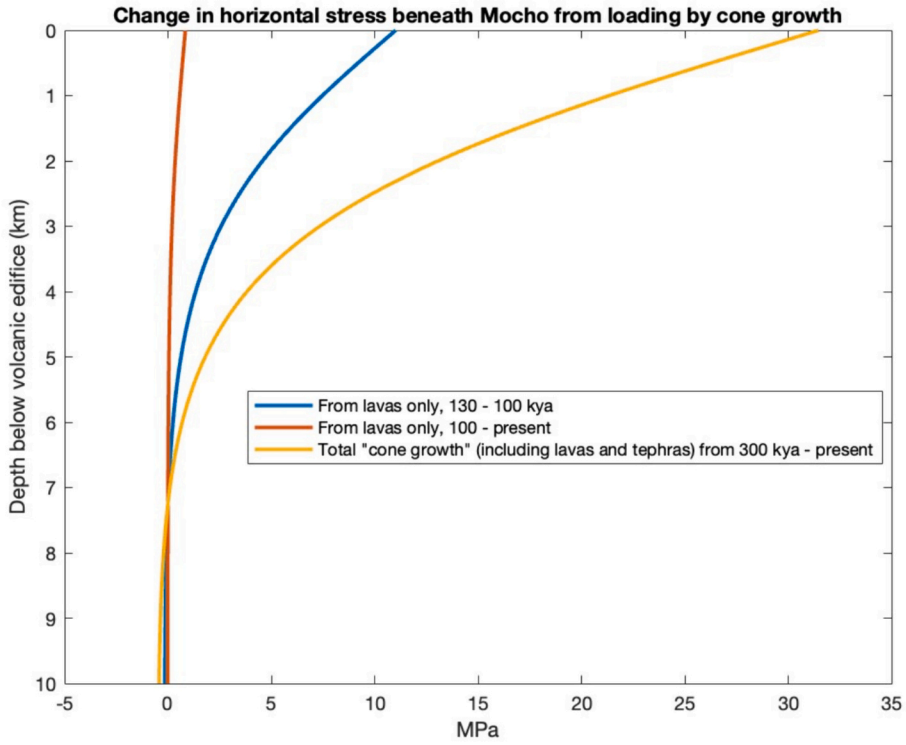

Fig. 16. Change in compressive horizontal normal stress in response to growth of the Mocho-Choshuenco volcano with depth beneath the center of the edifice, using eq. 2.1 from Pinel and Jaupart (2000) with a Poissons's ratio of 0.25. Curves reflect the total normal stress distribution accumulating over different time periods of cone growth (from Moreno-Yaeger et al., 2024), including the penultimate post-glacial period of rapid cone growth (1.4 km^3/kyr) from 130 to 100 kya (blue), 100 kya to present (~0.03 km^3/kyr; red), and 300 kya to present (~0.3 km^3/kyr; yellow).

b). We used the ages of mapped lava flows to constrain the timing of the onset of incision, which, combined with the estimates of eroded rock masses and drainage areas, yield maps of eroded rock mass fluxes. Since this approach assumes that the valley was eroded entirely over the time since the mapped lava flows were emplaced, this gives upper bounds on erosion rate estimates and hence upper bounds on erosion-driven changes in crustal loading.

Valleys on the flanks of Mocho-Choshuenco are as deep as 440 m. Using a bedrock density of 2.8 g cm^{-3} and the ages of the mapped lava flows, this translates to rock mass fluxes as large as 7600 t km^{-2} yr^{-1} (Fig. 17). Erosion of valleys this deep corresponds to local drops in crustal loading as large as 12.1 MPa, equivalent to unloading of 1.35 km of ice. The eroded valleys are all on the flanks of the volcano, 2–15 km from the summit of Mocho-Choshuenco (Fig. 17).

We are unaware of measurements of sediment deposition rates in the area surrounding Mocho-Choshuenco over the past glacial cycle, which precludes the possibility of constructing an empirically constrained sediment deposition history for the region. For the purposes of illustrating the potential effects of sediment deposition on crustal stress changes, we construct a prospective deposition history by identifying geomorphically plausible sinks for each valley's eroded sediment.

Given the presence of floodplains upstream of the lakes and the absence of large deltas, we built a prospective deposition scenario in which sediment is deposited exclusively on floodplains (Fig. 17). Restricting deposition to these relatively small areas yields higher estimates of deposition rates—and therefore higher estimates of deposition-driven increases in crustal loading—than would occur if deposition were more widely distributed. Thus, these can be considered upper bounds on deposition rates in the depositional areas.

We began identifying potential depositional areas by mapping channel networks around Mocho-Choshuenco, calculated by applying D8 flow routing to 30-m resolution topographic data (SRTM 4 Digital Elevation Model; NASA Shuttle Radar Topography Mission, 2013). These channel networks indicate the direction rivers transport eroded sediment from each valley. To delineate depositional areas along each river, we used the presence of meander belts, point bars, and fans in Google Earth satellite imagery, low gradient (< 0.001) areas, and previously mapped deposition areas (Campos et al., 1998; Rodríguez et al., 1999; Moreno and Lara, 2007; Moreno-Yaeger et al., 2024). From these observations we delineated six depositional areas in floodplains that collectively lie 10–36 km away from the summit of Mocho-Choshuenco (Fig. 17).

We applied sediment mass conservation in each time interval (Fig. 17; 130–18 ka, 18–12 ka, and 12 ka-present) to ensure that the mass of sediment in each depositional area matched the mass of eroded sediment from the contributing valleys. Within each depositional area, we applied spatially uniform deposition rates, which yielded rates as large as 8800 t km^{-2} yr^{-1}. This corresponds to a change in surface loading of 11.2 MPa, equivalent to the addition of 1.25 km of ice.

Elsewhere in the CSVZ, seismic surveys in several lakes reveal facies interpreted to be the paleo-interface of lacustrine deposits and ice, suggesting that lakes in the CSVZ pre-date the last glacial cycle (Heirman et al., 2011; Van Daele et al., 2016). This implies that the lake basins were likely filled with ice during glaciation and then filled with water after glaciation. If so, then deglacial changes in load in the lake basins should be associated with the replacement of ice with an equivalent volume of water. This would generate a far smaller increase in load than would have been generated if the lake basins had been empty before filling with water. For example, given the maximum depth of Lago Maihue (207 m; Rodríguez-López et al., 2024) and the 90 kg m^{-3} density difference between water and ice, the maximum increase in load associated with the replacement of ice by water in the Lago Maihue basin is 0.18 MPa (equivalent to ~20 m of ice), which is substantially smaller than the estimated changes in load associated with erosion and

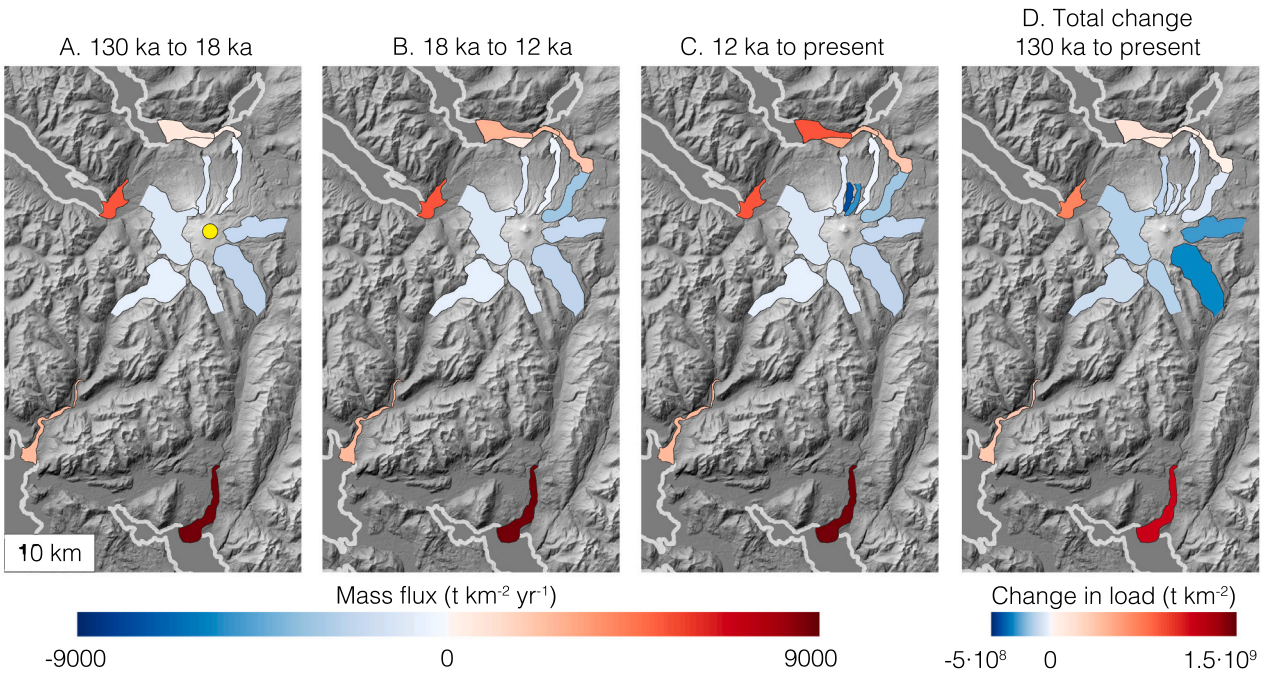

Fig. 17. Estimates of erosion rates (blue) and deposition rates (red) around Mocho-Choshuenco from 130 ka to present. Summit is indicated by a yellow circle at 39.93°S, 72.03°W. Lakes are outlined in light gray lines in grayscale shaded topography. A. Estimates of erosion rates (blue) and deposition rates (red) around Mocho-Choshuenco at 130–18 ka. B—C. As in panel A, but for 18–12 ka and 12 ka-present, respectively. D. Total change in load associated with erosion and deposition from 130 ka to the present. Erosion is focused on the volcano flanks ~2–15 km of the summit, while deposition is focused in small areas farther from the volcano, up to ~36 km from the summit. This implies that the net effect of sediment redistribution directly on the volcano is a reduction in crustal load.

deposition elsewhere across the study area. Thus, for simplicity in our simulations, we neglected changes in load associated with the replacement of ice with water in the lake basins during deglaciation.

After constructing this sediment redistribution scenario, we used the rates and patterns of erosion and deposition in Fig. 17 to compute changes in crustal stresses in response to the imposed changes in surface loading around Mocho-Choshuenco. The largest reductions in stress are under the volcano flanks where erosion is fastest, while the largest increases in stress are under floodplains where deposition is fastest (Fig. 18). Changes in stress grow smaller in amplitude and laterally smoother with depth, demonstrating that the largest changes in crustal stress and the largest lateral gradients in changes in crustal stress are nearest the surface. Over the duration of this sediment redistribution scenario, the largest integrated stress changes at 2 km depth are no larger than ~1.5 MPa in magnitude (Fig. 18D). These crustal stress changes are small relative to those associated with the ice unloading during deglaciation, which generated changes in crustal stress that exceed 10 MPa in magnitude near the surface (Fig. 18).

Together, Fig. 17 and Fig. 18 illustrate how to account for sediment redistribution on active volcanoes and how to compute crustal stress responses to it, and thus provide a template for applying this approach to volcanoes throughout the CSVZ and elsewhere. Future work using this approach could benefit from field-derived measurements of erosion and deposition rates (e.g., Schachtman et al., 2019), as well as model simulations that account for transient variations in physical and chemical erosion rates (e.g., Ferrier and West, 2017), which could help identify periods of rapid changes in crustal loading.

5.5. Modeling evolution of magma reservoirs of varied composition under ice loading and unloading conditions

Open system magma chambers host a wide range of coupled nonlinear processes and consequently their response to variations in external forcing, such as surface load changes, is complex. Our primary modeling goal when considering the physical response of a magma chamber to ice loading and unloading is to learn about the causality between surface load changes and the thermo-mechanical conditions of the chamber, specifically with respect to its eruption history. While the stress changes caused by ice accumulation and loss are small compared to the confining pressure at the depth of the subvolcanic magma chambers (4–12 km), many factors associated with the evolving stress state of the crust around the chamber caused by these loading/unloading events can affect the evolution of the coupled magma chamber-host crust system.

On a thermodynamic basis, the confining pressure changes caused by ice loading are moderate in amplitude but can influence the partitioning of volatiles (H_2O and CO_2) between the melt and an exsolved phase (hereafter called magmatic volatile phase or MVP). Coonin et al. (2024) illustrated that ice unloading can expedite gas exsolution, building up pressure in the chamber, significantly increasing magma compressibility and subsequently increasing the volume of magma erupted. On a mechanical basis, the confining pressure changes caused by ice loading and unloading on the magma have a negligible influence over its physical properties besides volatile partitioning. The mechanical response to loading is primarily the stress changes in the crust and their effect on the initiation and propagation of dikes. The spatial and temporal variations of the stress field around the magma chamber and between the chamber and the surface impact the critical overpressure required to initiate a dike. Moreover, the stress field in the crust between the chamber and the surface affects the growth of dikes, their shape and trajectory, and therefore their ability to reach the surface and feed an eruption or stall in the crust. While dike propagation will be discussed in more detail below, we assume for now that whether a dike reaches the surface or stalls at depth does not dramatically impact the physical evolution of the subvolcanic magma chamber. For simplicity, we consider all dikes sourced from the shallow storage region to generate an eruption. This assumption is revisited below.

Teasing out the causality between surface load changes and the eruption history at a volcanic center, as well as the sensitivity of magma chambers to ice loading cycles, requires a simplified approach where

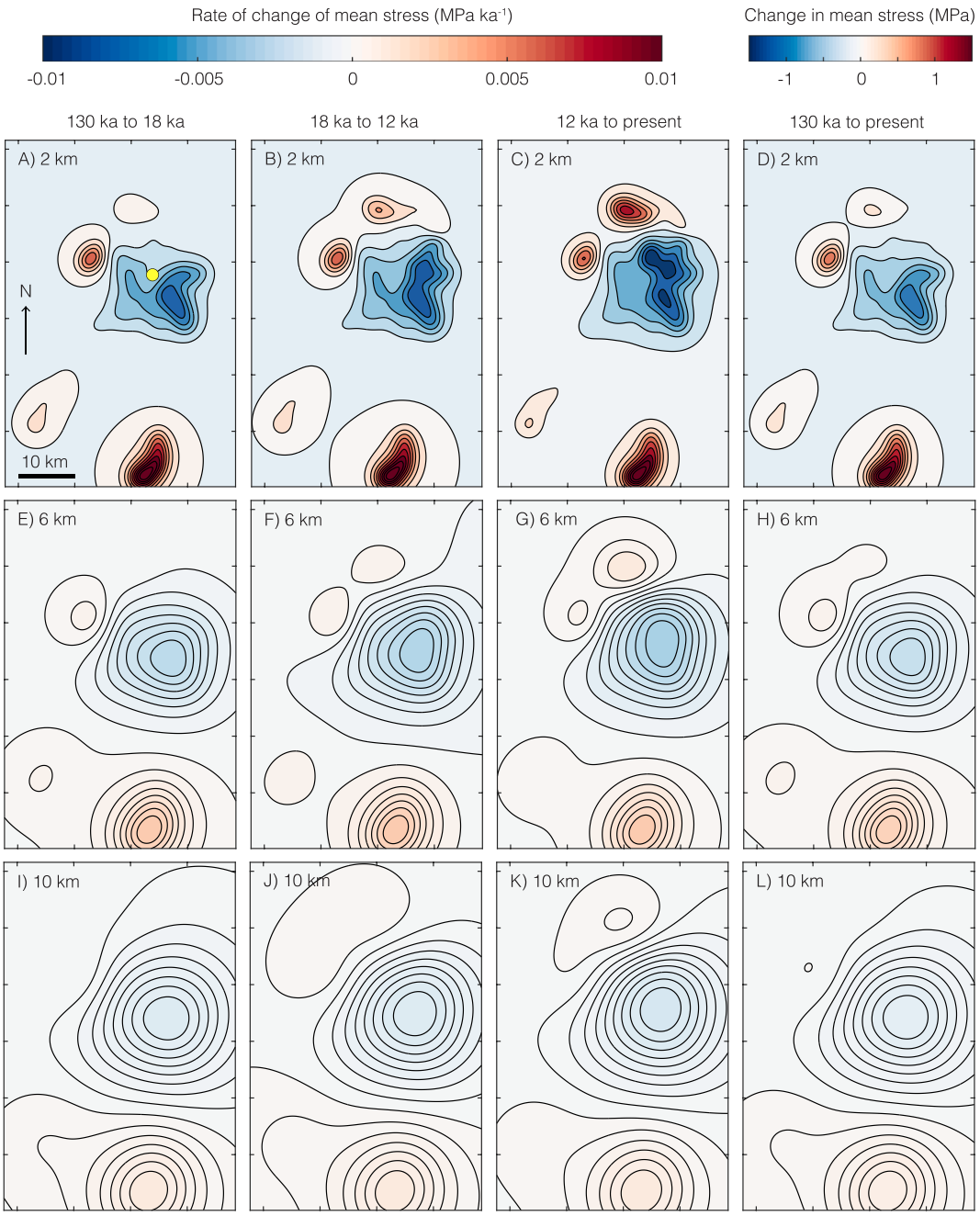

Fig. 18. Map of rate of change in mean crustal stress at 2 km depth in response to erosion and deposition from 130 ka to present. A. Map of rate of change in mean crustal stress at 2 km depth in response to erosion and deposition from 130 to 18 ka (Fig. 17A). Yellow circle indicates summit of Mocho-Choshuenco. B—C. As in panel A, but in response to erosion and deposition at 18–12 ka and 12 ka to the present, respectively (Fig. 17B-C). D. Total change in mean crustal stress over 130 ka to present. *E*-H. As in panels A-D, but at 6 km depth. I-L. As in panels A-D, but at 10 km depth. The largest reductions in stress are under the volcano flanks where erosion is fastest, while the largest increases in stress are under valleys where deposition is fastest. Stress changes grow smaller in amplitude and laterally smoother with depth, illustrating that the largest changes in crustal stress are nearest the surface.

parametric analyses are possible within a framework that accounts for the necessary processes to study possible feedbacks. We base our model on the box model framework introduced by Jellinek and DePaolo (2003) and expanded by Degruyter and Huber (2014) to analyze the thermal and mechanical evolution of a subvolcanic magma chamber subjected to magma recharge, hosting a multiphase magma (Fig. 19). Two notable recent additions to the model include the presence of CO_2 as a secondary volatile species (Scholz et al., 2023) and the consideration of time-dependent changes in confining pressure associated with ice unloading (Coonin et al., 2024). Both are accounted for in the model results (Fig. 20), but it is important to note that the unloading model proposed in Coonin et al. (2024) is further modified here to account for both ice loading and unloading phases.

As a thought experiment, we devise a series of simulations of magma chambers undergoing an ice loading cycle to understand if conditions exist where the eruptive history of the system mimics qualitatively the features observed in Fig. 4, namely a drop in cumulative volume erupted as the ice sheet grows followed by an increase in eruptive output soon after the initiation of the unloading. The series of simulations discussed here assume a greater confining pressure change than estimated in Figs. 14 and 15 (15 MPa change at the depth of the chamber) that would be consistent with a thick ice sheet covering the whole edifice.

Moreover, we consider a case where the effective fracture toughness to initiate and grow a dike from the magma chamber correlates with the confining pressure because of anelastic effects near the crack tip as suggested by Barenblatt (1962) and Rubin (1993). In that context, the critical overpressure in the chamber required to initiate dikes increases during periods of ice growth and decreases during unloading. Whereas more work is required to establish whether this effect is relevant in the present case and how large it may be, we consider here arbitrarily that the maximum change in critical overpressure is 6 MPa. The evolution of the confining pressure in the model starts from background confining pressure (unglaciated), to growing ice load (transient increase in confining pressure to a constant high confining pressure), transitioning into a rapid decrease (ice unloading) back to background confining values (bottom dashed line in Fig. 20a).

Our modeling predicts that requent eruptions take place in the background state. In this particular instance, the magma is initially undersaturated and MVP bubble exsolution only takes place consistently after approximately 4000 years (Fig. 20 panel c). As ice loading proceeds, both the confining pressure and critical pressure for eruptions increase, albeit the latter more than the former because of the assumed increase in fracture toughness at higher confining pressure. The increasing critical overpressure extends the period between eruptions up to a point when the eruptions are suppressed for almost 5000 years. During this quiescent stage, the magma chamber grows in mass and volume. Once unloading starts, the critical pressure required to initiate a dike decreases which facilitates the onset of new eruptions. These final eruptions are significantly larger in volume than the ones before loading, mostly because the magma chamber has grown during the high confining pressure stand and because MVP bubbles render the magma more compressible (Townsend et al., 2019). Overall, on a qualitative basis, this mechanical response to ice loading leads to a cumulative mass erupted (Fig. 20d) that resembles the growth of Mocho-Choshuenco, Puyehue-Cordón Caulle and, to a lesser extent, Calbuco (Fig. 4).

In order to compare simulation outputs within which recharge, magma chamber depth and volume differ, Degruyter and Huber (2014) developed a regime diagram built of ratios of fundamental timescales that control the evolution of magma chambers. These include the timescale for magma chamber cooling τ_{cool} (time to cool a chamber of volume V), the timescale for magma injection/recharge τ_{inj} (time to fully replenish a magma chamber of volume V with a given recharge rate) and the timescale of viscous relaxation τ_{rel} (time to transition from an elastic to a viscous crustal response). These timescales were further complemented by the addition of a timescale for surface load change by Coonin et al. (2024), which is here, by choice, fixed for all runs and not discussed further. The magma chamber scenarios that display a strong modulation of the eruption history by surface load changes encompass conditions for which $\tau_{cool} > \tau_{inj}$ (recharge-driven eruptions are possible) and τ_{rel} are barely greater than τ_{inj}. The latter condition is crucial, as it means that the rate of pressurization by recharge is initially just large enough before loading to overcome viscous relaxation of overpressure by creep around the chamber. Finally, we find that cases where eruptions are not only suppressed at high surface load but the erupted mass rate increases after unloading compared to the background state require the chamber to be initially volatile undersaturated and exsolve MVP by second boiling during the long repose during the period of high ice load.

It is important here to revisit some of the assumptions underlying this thought experiment. We considered a larger change in confining pressure at the depth of the magma chamber than those computed for the volcanoes considered here. Moreover, we assumed that this change in confining pressure directly impacted the critical overpressure required to initiate a dike out of the magma chamber. In many ways we considered optimal conditions for load changes to affect the eruptive history of these synthetic volcanic systems. Whereas we show under these most favorable conditions that it is possible to obtain an eruptive output due to loading changes that qualitatively resembles that of Mocho-Choshuenco and Puyehue-Cordón Caulle, the required conditions are narrow and define a very constrained sweet spot that these systems must satisfy coincidentally before the LGM. While such a coincidence is not impossible, it is unlikely, which suggests that other factors, not accounted for in our model, play an important role and must broaden the range of conditions that generate these types of eruption histories.

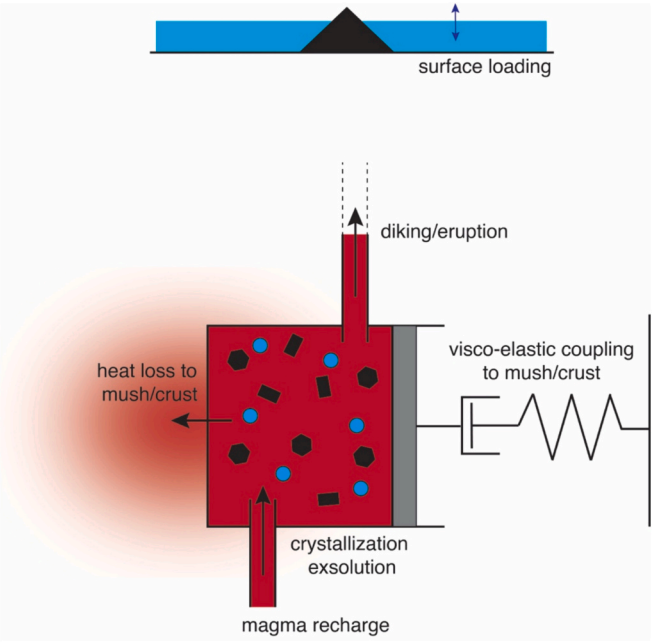

Fig. 19. Illustration of the magma chamber model. The magma is assumed homogeneous in the chamber, changes in the relative proportion of melt, crystals and MVP are driven by conductive cooling to the surrounding crust and is governed by the crystallinity-temperature and solubility curves (for H_2O-CO_2 mixtures), see Scholz et al. (2023) for details. Modified from Degruyter and Huber (2014).

One important factor not accounted for here is that the initiation of a dike from a magma chamber does not necessarily lead to an eruption at the surface. Dikes may arrest before reaching the surface either because they are limited by source pressure and volume and/or because of thermal (freezing) and mechanical barriers to propagation (e.g., stress barriers). Townsend and Huber (2020) used a coupled magma chamber-dike model to identify specific source conditions needed for chamber-fed dikes to reach the surface before depleting the magma pressure and volume from their source. Chambers below a critical volume and compressibility will lose pressure faster than the dike can extend to the surface. In addition, deep chambers or less buoyant magmas will require even larger critical volumes to erupt at the surface. Considering these factors would further narrow the conditions under which we expect to observe a surface manifestation of a magma chamber's response to ice loading. Furthermore, while greater critical overpressures for dike initiation might inhibit dike formation by causing $\tau_{inj} > \tau_{rel}$, chambers reaching critical pressure (i.e. those that maintain $\tau_{inj} < \tau_{rel}$) during loading will experience greater pressure for dike growth, potentially leading to larger dike volumes with a higher chance of reaching the surface. From this perspective, an increase in the critical overpressure during periods of glaciation could for some cases result in a greater ratio of magma extrusion to intrusion, contrary to observations at Mocho-Choshuenco, Puyehue-Cordón Caulle, and Calbuco.

On the other hand, dike propagation is very sensitive to the state of stress at the leading edges of the dike. Increasing compressive stresses between the chamber and surface during ice loading could potentially slow down or arrest the vertical growth of dikes and instead encourage either stalling or lateral growth (Pinel and Jaupart, 2000, 2004). Upon removal of these compressive stresses during ice unloading, dike ascent

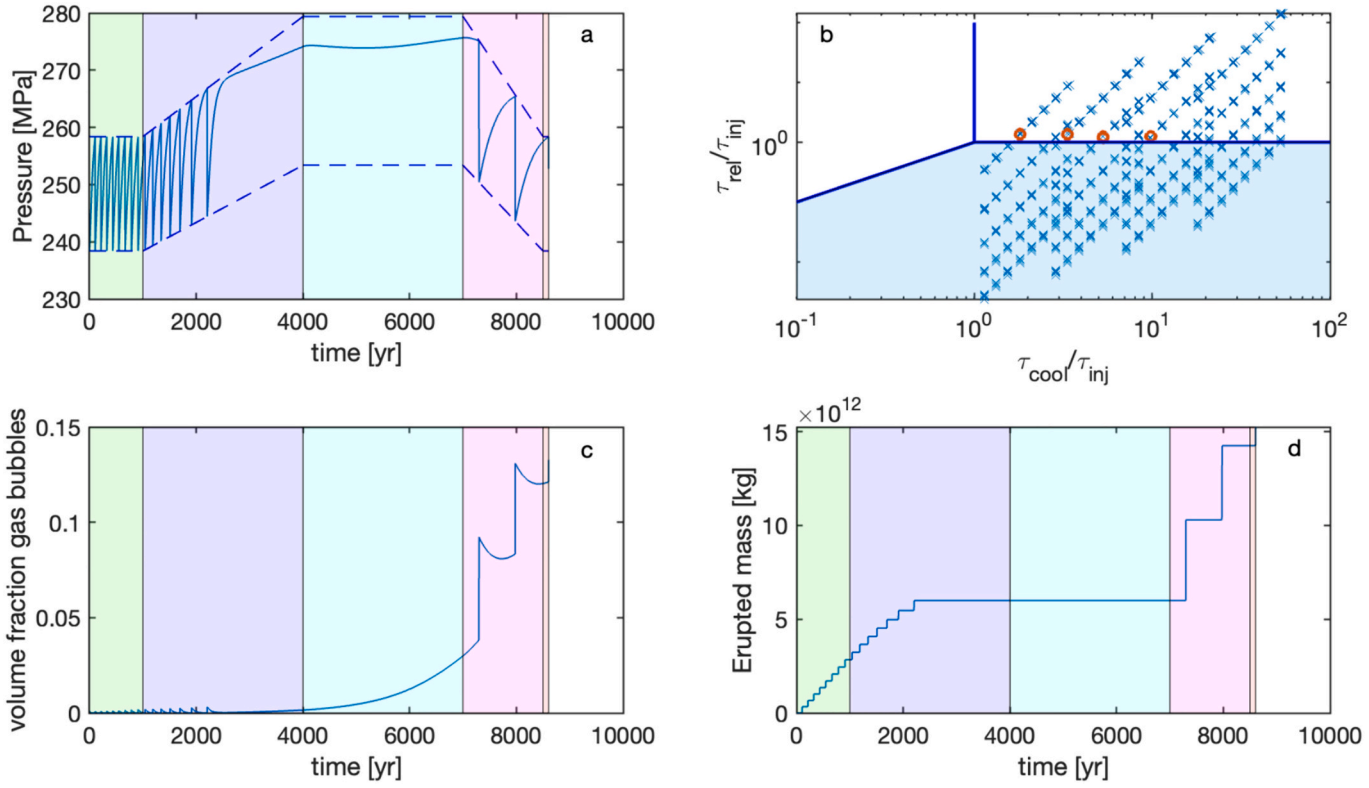

Fig. 20. Timeseries of magma chamber pressure (panel a), MVP volume fraction (panel c) and cumulative erupted mass (panel d) for a silicic magma chamber of initially 30 km^3 located at 9 km depth and containing initially 6 wt% H_2O and 200 ppm CO_2, subjected to a constant recharge rate of 2.5 $\times$ 10^{-3} km^3/yr. Panel a shows the magma pressure in the chamber through time, with dashed lines showing the confining pressure (bottom one) and critical pressure for eruptions (top one). The background colors highlight the different phases in the loading evolution. The green shaded area covers the first 1000 years of magma chamber evolution at a constant confining pressure (before ice loading). This phase serves as a background state for comparison to the subsequent eruption history. The stage highlighted in purple reflects the increase in ice load over 3000 years, and it is followed by a stage of constant maximum ice load for 3000 years (in cyan) and a rapid unloading phase (pink) spanning 1750 years (half of the loading time) before the background conditions are restored. Panel b shows a regime diagram of time-scales for 800 simulations (symbols) using the initial conditions for each simulation. T_{cool} is the magma chamber cooling time scale, T_{inj} is the recharge timescale and T_{rel} is the viscoelastic timescale of the crust (more information in the main text). Blue crosses refer to simulations that do not qualitatively agree with the cumulative eruptive outputs shown for Mocho-Choshuenco and Puyehue in Fig. 4 and red circles are the simulations that do qualitatively agree.

would become more feasible (Wilson and Russell, 2020). This effect would broaden the range of conditions conducive to the type of magma chamber response depicted in Fig. 20, to include higher values of τ_{rel}/τ_{inj}.

Mocho-Choshuenco and Puyehue-Cordón Caulle both exhibit ranges of composition that change coevally with the end of the LGM, with silicic magmas contributing more to the eruptive outputs after LGM (Figs. 4 and 5). Moreover, the composition of the magmas erupted is consistent with the more silicic endmembers being generated through crystal fractionation from mafic parent magmas, with moderate degrees of assimilation (Jicha et al., 2007; Singer et al., 2008; Winslow et al., 2022; Moreno-Yaeger et al., 2024). Can the hiatus or decline in eruption during LGM play a role in the maturation of the magmas and, consequently, the generation and extraction of more differentiated erupted products?

Melt extraction from crystal mushes is dominated by a combination of crystal settling and mush repacking (Bachmann and Huber, 2019). The degree of differentiation required to generate the silicic endmember components at Mocho-Choshuenco and Puyehue-Cordón Caulle is significant and likely extends beyond what hindered crystal settling alone can explain. Using the recent work by Florez et al. (2024a) where melt extraction from mushes under compaction by repacking is calibrated by phase separation experiments, Florez et al. (2024b) applied a model of compaction by mush repacking to constrain the efficiency of high silica melt extraction from cumulates at the Spirit Mountain batholith in Nevada. They calculate an estimated time required to extract a given volume of melt from a repacking mush driven solely by gravity (upper bound estimate given that shear deformation can speed up the process).

We use the same approach to estimate the time it would take to extract 5 km^3 of silicic magma from the mushy part of the magma chamber under Mocho-Choshuenco to produce the Neltume Tephra that erupted ~3000 years after the LGM (Rawson et al., 2015, 2016; Moreno-Yaeger et al., 2024). Assuming that the caldera footprint of the Neltume eruption provides a good estimate for the areal extent of the magma chamber we find that a melt-rich lens of 300–500 m thickness would account for the volume of magma erupted. Repacking of the mush under gravity alone would extract enough melt to fully account for the volume erupted in 20–30 kyr (Florez et al., 2024b), which is an upper bound as (1) some amount of melt extracted before the LGM was already present and (2) stress changes around the chamber also induce deformation and therefore speed up the repacking processes. Under these conditions it is not surprising to see that incubation periods as long as 50 to 70 kyr at Mocho-Choshuenco can lead to conditions amenable to the accumulation of a silicic melt pool necessary to generate the rhyolitic Neltume Tephra.

6. Evolution of volcanoes and their plumbing systems spanning a glacial-interglacial cycle

To illustrate how field observations, geochronologic constraints, and

the modeling of ice sheet retreat, erosion and deposition, surface loading, stress evolution within the crust, and magma reservoir behavior may be used in an integrated manner to better understand the evolution of magma plumbing systems, we discuss changes in magma storage conditions and eruption rates spanning the last glacial-interglacial transition at three CSVZ composite arc front volcanoes. As an initial, first-order attempt at estimating pre-eruptive depths of magma extraction and storage, we employ a machine learning-based thermobarometer for magmatic liquids (Weber and Blundy, 2024) that estimates pressures and temperatures from the major element compositions of lava flows and tephra. Whereas the Weber and Blundy (2024) algorithm facilitates rapid surveys of thermobarometric conditions below specific volcanoes, we also recognize that it is important to obtain estimates from measurements of mineral-melt equilibria and via thermodynamic modeling, particularly for more crystal-rich eruptive products. We note that the more crystal-poor silicic eruptive products (>62 % SiO_2) characteristic of the target volcanoes meet the criteria for application of the Weber and Blundy (2024) method. Ongoing work at the target volcanoes (Fig. 2) aims to obtain mineral and melt-based pressure and temperature estimates for comparison to the Weber and Blundy (2024) estimates highlighted here. The examples from Puyehue-Cordón Caulle, Mocho-Choshuenco, and Calbuco volcanoes highlight that each underlying magma plumbing system has responded differently to the rapid retreat of the northernmost Patagonian ice sheet.

6.1. Volcán Puyehue-Cordón Caulle

Despite producing explosive-followed-by-effusive rhyolitic eruptions of more than 1 km^3 each in 1921–22, 1960, and 2011–12, constraints on the longer-term evolution of the magma plumbing system beneath Volcán Puyehue-Cordón Caulle are limited. Salient to our focus on potential impacts that ice loading and unloading may play in modulating volcanic outputs, Singer et al. (2008) show that after 300 kyr of erupting mainly basaltic andesitic to andesitic (52–61 wt% SiO_2) lava flows, eruptive products including lavas flows and tephra become exceptionally bimodal beginning at about 35 ka, and more so immediately following the LGM (Figs. 5 and 21). On the Puyehue composite cone, a stack of basaltic to basaltic andesitic (48–55 wt% SiO_2) lava flows, first recognized by Gerlach et al. (1988), crop out between dacitic lava flows $^{40}Ar/^{39}Ar$ dated at 14.9 ± 2.9 and 11.5 ± 1.1 ka. These ~13 ka basalts erupted from vents within a km of younger rhyolitic lavas $^{40}Ar/^{39}Ar$ dated at 6.9 ± 1.6 to 5.2 ± 2.4 ka comprising the southern rim of the modern Puyehue summit crater (Singer et al., 2008). Trace element compositions (K/Rb vs. Rb, and Dy/Yb vs. SiO_2) suggest that the dacites and rhyolites erupted from Puyehue volcano could be produced by extensive fractional crystallization of a cumulate mineral assemblage comprising hornblende, clinopyroxene, orthopyroxene, plagioclase, and magnetite (Singer et al., 2008), despite the absence of amphibole in the eruptive products. Projecting whole rock compositions from plagioclase into the pseudoternary olivine-clinopyroxene-quartz system, Gerlach et al. (1988) suggest that fractionation occurred at pressures of 200–500 MPa, equivalent to depths of about 7–17 km.

Hydrothermal phase equilibrium experiments (Castro et al., 2013), mineral equilibrium and radar satellite geodesy-measured surface deformation (Jay et al., 2014), and rhyolite-MELTS thermodynamic models (Seropian et al., 2021) constrain the pressures of pre-eruptive storage for the rhyolitic magma erupted from Cordón Caulle in 2011 to between 80 and 150 MPa, equivalent to about 3 to 7 km depth (Fig. 21). Thermodynamic modeling suggests that the 1921–22 and 1960 rhyolitic eruptions from Cordón Caulle were sourced from similar depths (Seropianet al., 2021). Rhyolite-MELTS thermodynamic models are consistent with low pressure fractional crystallization of basaltic andesite to produce the post-glacial rhyolites (Fig. 5). Volcán Puyehue lies 8 km southeast from the 1960 and 2011–12 eruptive vents on Cordón Caulle and it remains unclear whether or not the magma plumbing system beteween these vents is connected at depth (Jay et al., 2014; Seropian et al., 2021).

The Weber and Blundy (2024) thermobarometer has been employed to gauge changes in magma extraction and storage depths over the 70 kyr period spanning the last glacial to post-glacial transition beneath Puyehue-Cordón Caulle (Fig. 21). Whole rock (mineral + matrix) compositions are inferred to reflect depths where magma crystallization begins; matrix glass compositions are inferred to reflect pre-eruptive storage depths of eruptible melt (Weber and Blundy, 2024). Between 70 and 35 ka many basaltic andesitic magmas were extracted from depths of about 16–25 km, and the andesitic and dacitic magmas from about 9 to 12 km (Fig. 21). A conspicuously mingled lava flow, $^{40}Ar/^{39}Ar$ dated at 34 ka, attests to contact between deeply sourced basaltic andesitic and shallower dacitic magma during the LGM (Fig. 21). Rhyolitic eruptions, sourced mainly from depths of 5 to 7 km, commenced at both Cordón Caulle and Puyehue during the period of maximum intracrustal stress change, 18–15 ka. The shallow crystallization and storage of rhyolite suggested from the Weber and Blundy (2024) thermobarometer is consistent with the experimental and thermodynamic estimates outlined above. Also, soon after the peak change of crustal stress, basaltic magma from deep levels erupted along with the more shallowly sourced rhyolitic magma (Fig. 21). Thus, a major shift in the depth of sources for erupted magmas, and an increase in compositional bimodality, is associated with the rapid drop in surface loading. The basaltic lavas erupted at Puyehue are among the most MgO-rich in the SVZ (Gerlach et al., 1988) and have a much wider range in $^{87}Sr/^{86}Sr$ ratios than the previously or subsequently erupted rhyolites (Singer et al., 2008), consistent with a deep crustal origin distinct from shallower reservoirs. We hypothesize that the stress drop of about 5 MPa enabled the Liquine Ofqui fault system (Fig. 2), on which the Puyehue edifice sits, to become an efficient pathway for the ascent of basalt from the lower crust (e.g., Watt et al., 2013; Chamberlain et al., 2024) and led to an increase in the growth rate of the Puyehue edifice (Fig. 4).

Obtaining the compositions of key minerals from prehistoric lava flows and tephra layers that are well-dated and span the range of compositions erupted during the last 70 kyr, in parallel with rhyolite-MELTS modeling (e.g., Seropian et al., 2021), is clearly the next step to refining the pressures at which magmas were stored during and after the last glacial-interglacial transition and exploring in more detail how the Puyehue-Cordón Caulle magma plumbing system responded to glacial loading and unloading (Fig. 21).

6.2. Volcán Mocho-Choshuenco

The compositions of minerals including plagioclase, clinopyroxene, orthopyroxene and amphibole, as well as modeling crystallization conditions using the alphaMELTS thermodynamic phase equilibrium code, have been used to estimate pressures of pre-eruptive magma storage for a set of well dated lava flows and tephras at Mocho-Choshuenco (Fig. 5; the findings will be reported elsewhere). These estimates suggest that during the last 50 kyr pressures of pre-eruptive storage and crystallization for both silicic and mafic magmas varied greatly between about 200 to 450 MPa (7 to 16 km depth). Notably, water-rich amphibole-bearing dacitic to rhyolitic magmas erupted at 11.5 ka were extracted from a reservoir 2 to 5 km deeper in the crust, ~12–14 km, than were earlier erupted dacites. Holocene eruptions tapped relatively shallow magma reservoirs at 7–11 km depth.

The above pressure estimates are reinforced and expanded upon by those obtained using the Weber and Blundy (2024) thermobarometer which suggests that most magmas crystallized in reservoirs between about 7 and 16 km depth during the last 50 kyr (Fig. 21), with dacitic and rhyolitic magma sourced from deeper crustal levels than at Puyehue-Cordón Caulle, but not as deep as andesitic magmas from Calbuco (Fig. 21). Shortly following the unloading of the Patagonian ice sheet, at 11.5 ka, an explosive eruption of 5 km^3 of rhyolitic Neltume Tephra left behind a 3 km-wide summit caldera (Moreno-Yaeger et al., 2024). The Neltume rhyolite magma began to crystallize at a depth of about 13 km,

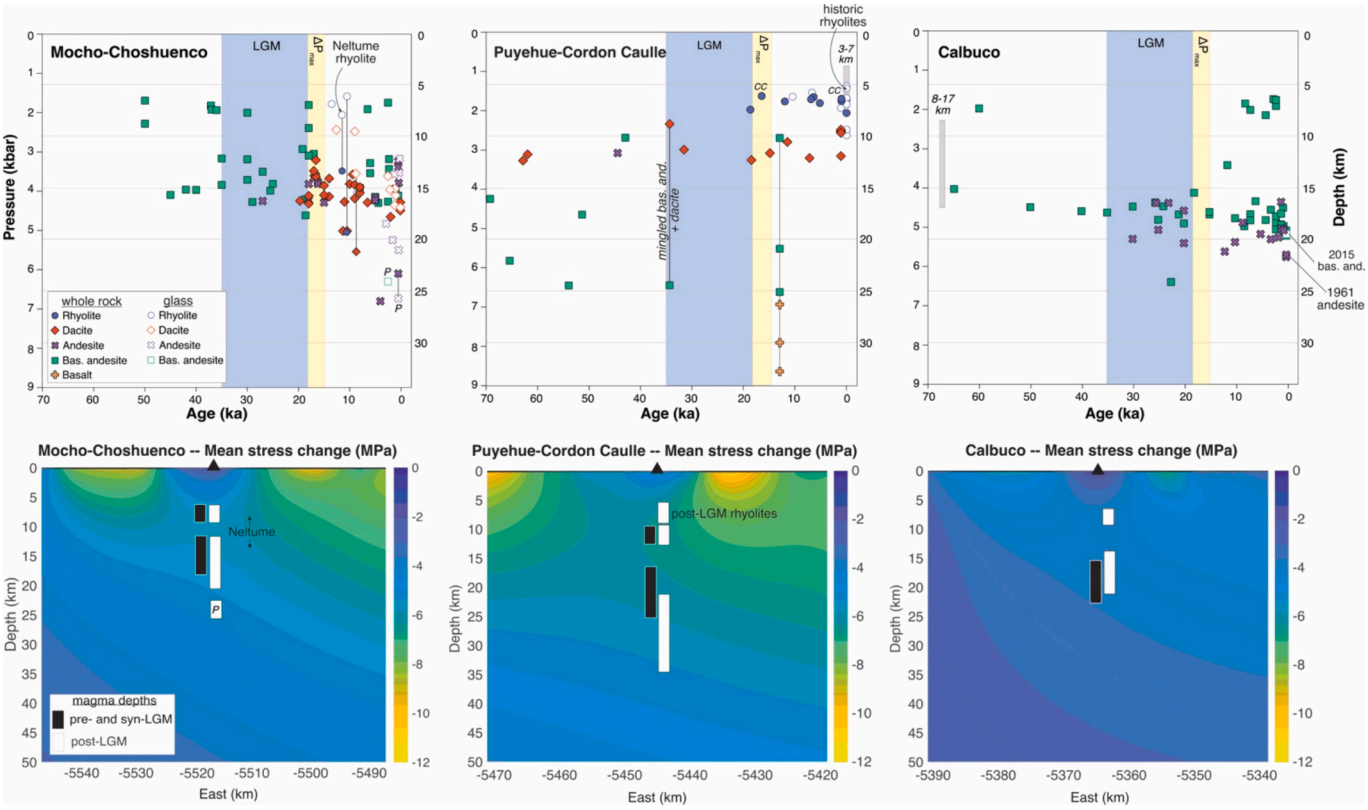

Fig. 21. Upper panels: whole rock lava and tephra compositions and tephra glass compositions from Mocho-Choshuenco, Puyehue-Cordón Caulle, and Calbuco volcanoes are used in the Weber and Blundy (2024) machine-learning thermobarometer to estimate pressures (and depths assuming crustal density of 2.7 g/cm^3) of magma extraction (whole rocks) or storage (glass). Ages of lava and tephra samples from Calbuco are in Mixon et al. (2021), from Puyehue-Cordón Caulle these are in Singer et al. (2008), Naranjo et al. (2017), and Alloway et al. (2022), and from Mocho-Choshuenhco they are in Moreno-Yaeger et al. (2024). Ages from several lava samples are inferred from stratigraphic positions relative to lavas from which $^{40}Ar/^{39}Ar$ ages have been obtained. Vertical gray bars show range of pressures estimated in sources from the literature discussed in the text. For Calbuco this includes four samples spanning the 70 kyr period, from Puyehue-Cordón Caulle the 3–7 km depth range is from experimental and thermodynamic constraints on historical rhyolites. *P* denotes two small parasitic cones on Mocho-Choshuenco, *CC* denotes prehistoric rhyolite from Cordón Caulle with compositions identical to those from Puyehue. Lower panels: Mean stress changes at depth from the ice sheet-surface loading models for areas surrounding each of the three volcanoes discussed in the text and illustrated in Fig. 15. The black and white boxes schematically illustrate the positions of prominent magma reservoirs that fueled eruptions prior to, and following, the period of peak intracrustal stress change between 18 and 15 ka (the yellow vertical bands denoted ΔP_{max} reflect stress drops illustrated in Fig. 14).

whereas the crystal-poor rhyolitic melt was extracted from this magma and stored at 6 km depth prior to the caldera-forming eruption (Fig. 21). The latter finding of shallow storage of rhyolitic melt is consistent with rhyolite-MELTS thermodynamic models (Fig. 5). The output from the Weber and Blundy (2024) thermobarometer thus suggests a vertically extensive silicic reservoir produced the Neltume Tephra. Moreover, the output suggests magma extraction from two separate depth regimes both prior to, and following, the rapid drop in surface load of about 3 to 6 MPa. During the last 5 kyr, andesites erupted from small parasitic vents on the flanks of Mocho-Choshuenco likely tapped into magma reservoirs residing much deeper, 23–26 km, than any prior eruption (Fig. 21). Thus, the most striking changes in the magma plumbing system include the onset of abundant dacitic eruptions during the rapid drop in surface load between 18 and 15 ka, and the deepening of magma sources during post-glacial time. We hypothesize that surface loading during growth of the Patagonian ice sheet led large volumes of magma to pond, cool, and crystallize at depths of 13 to 19 km, where H_2O-saturated amphibole-bearing dacite magma formed. Rapid unloading may have propelled extraction, ascent to 6 km depth, and exsolution of H_2O from the Neltume rhyolitic melt that pressurized the shallow magma reservoir, leading to an explosive eruption and caldera collapse at 11.5 ka (Fig. 21). During the last 12 kyr, the volumetric eruption rate from Mocho-Choshuenco has increased about 50-fold (Fig. 4), possibly in response to the reduction in surface load.

6.3. Volcán Calbuco

In contrast to Mocho-Choshuenco and Puyehue-Cordón Caulle, Calbuco has erupted compositionally monotonous basaltic andesite and andesite (53–61 wt% SiO_2; Fig. 5). Mineral thermobarometry acquired from lava flows, blocks, and bombs spanning the 96 ka eruptive history of Volcán Calbuco (Fig. 4), including scoria from the 2015 eruption, constrain magma storage and crystallization pressures to between about 210 and 460 MPa, corresponding to depths of about 8–17 km (Fig. 21; Arzilli et al., 2019; Morgado et al., 2019a, 2019b; Namur et al., 2020; Vander Auwera et al., 2021). This relatively deep level of crystallization and ponding of mafic magma containing amphibole suggests melt H_2O contents greater than 5 wt% that, upon degassing, can stall magma ascent (Rasmussen et al., 2022). From the thermobarometry survey of only four samples, no shift in magma crystallization or storage conditions that can be correlated with the glacial-interglacial transition is discernable (Vander Auwera et al., 2021). However, using the Weber and Blundy (2024) thermobarometer on whole rock lava and tephra compositions that span the last 70 kyr of eruptions on Calbuco (Mixon et al., 2021) we find that most basaltic andesitic to andesitic magma was extracted from magma reservoirs between about 16 and 20 km depth. However, during the Holocene, several basaltic andesite eruptions were sourced from reservoirs as shallow as 6–7 km (Fig. 21). The post-glacial period also coincides with a four-fold increase in the rate of eruptions

and cone growth (Fig. 4). We posit that divergence toward coeval deeper and shallower magma reservoirs and the uptick in eruptive frequency and cone growth rate the reflect the intracrustal stress drop of only about 2 MPa on a water-saturated basaltic andesitic magma that is recharged with mantle-derived melts at an exceptionally high rate (Mixon et al., 2021). The magma chamber model suggests that a high rate of magma recharge is offset by high rates of both magma cooling and viscous relaxation of the crust, suggesting a relatively cool geotherm situated beneath Calbuco.

7. Conclusions and future prospects

Addressing the mechanics and dynamics of ice sheet-arc magma plumbing system interactions at a regional-to-local scale is propelling us to a more granular, and physically realistic, understanding of what the volcanic record may be telling us about its responsiveness to glaciation. This effort benefits from a synthesis of existing and new field observations, laboratory measurements, and numerical simulations. Advances in $^{40}Ar/^{39}Ar$ radioisotopic and ^{3}He surface exposure geochronology, in conjunction with geologic mapping, permit reconstructions of volcanic eruptive histories spanning a glacial-deglacial cycle and in places can provide constraints on the thickness of ice at particular times. In parallel, existing and newly developed thermobarometers that constrain magma crystallization and storage depths can be applied to eruptive products spanning a glacial-deglacial transition, such that secular changes in magma eruptibility can be interpreted in light of intracrustal stress changes associated with glacial loading and unloading. The magnitude and geometry of the surface loading and unloading are captured in a numerical simulation of regional ice sheet retreat. We have found that rates and patterns of crustal loading and unloading based on estimates of erosion and deposition on and around volcano surfaces, and due to volcanic cone growth, are overwhelmed by the unloading due to ice retreat. Thus, the loading/unloading history due to ice retreat is central to the design of numerical simulations of magma reservoir responses to intracrustal stress changes beneath the volcanoes.

A simulation of retreat of the northernmost Patagonian ice sheet from 22 ka to the present that uses climate model input is remarkably consistent with empirical reconstructions that rely principally on the positions of dated glacial deposits marginal to the ice sheet. The numerical model simulates spatially and temporally heterogeneous changes in ice thickness, ice retreat velocity, and deglaciation age, each of which are critical to estimating changes in surface loading on the volcanoes of interest (Figs. 12 and 13). The numerical simulation suggests a southerly shift in moisture-carrying westerly winds likely contributed to the spatially heterogeneous deglaciation. Local ice sheet thicknesses of 1300 to 1900 m around the flanks of several composite volcanoes predicted by the numerical simulation are also supported by the observation of a 'bathtub ring' deposit of granitoid glacial erratic boulders (Fig. 8), as well as several precisely $^{40}Ar/^{39}Ar$-dated lava-ice contact features (Fig. 7).

In support of geologic maps of composite continental arc volcanoes, modern $^{40}Ar/^{39}Ar$, ^{14}C, and ^{3}He dating of eruptive products, including both lava flows and tephra deposits, can be sufficiently numerous and precise to reveal changes in eruptive rates during the past 100 kyr. The resulting chronostratigraphic constraints facilitate more accurate reconstructions of erosion of these composite edifices. At three volcanoes in the Andean CSVZ new geochronology reveals that rates of eruption and cone growth increased significantly during, or shortly after, the LGM. Notably, at Mocho-Choshuenco and Puyehue volcanoes, the uptick in eruptions follows the LGM by 1 to 3 kyr, whereas at Calbuco eruption rate increased at about 25 ka (Figs. 4 and 6), perhaps reflecting its position near the western limit of the Patagonian ice sheet (Fig. 2) where glacier thinning may have progressed a few kyr earlier than at the other volcanoes (Figs. 13 and 15). Moreover, periods of much lower growth rate preceded these *syn*- to post-LGM increases (Fig. 4). This may reflect the thermo-mechanical responses of upper crustal magma reservoirs that limit eruptions under conditions of maximum ice loading, but favor eruptions upon relatively rapid removal of the ice load. Our numerical magma chamber model suggests that this behavior may reflect a delicate balance between the timescale of viscous relaxation of surrounding crustal rocks, the rate of magma recharge from depth and, importantly, the effect of shallow crustal stress change on dike propagation (Fig. 20).

7.1. Outstanding issues

Ongoing work in the CSVZ is focused on improving the eruptive chronologies for several additional volcanoes, as well as cosmogenic dating of the duration of surface exposure of bedrock in several vertical profiles and on moraines east of the Andes (Romero et al., 2024). The surface exposure dating will be used to validate and refine the numerical ice sheet simulation for this region. Further work is needed to better establish how the simulated climate from TraCE-21 ka compares with proxy records (e.g., Moreno et al., 1999, 2015, 2018), which also may entail renewed efforts to produce proxy records of deglacial temperature and precipitation change. Improvements in the ice retreat model will, in turn, help improve the resolution of the surface loading model around the composite volcanoes of interest. Locating and dating many additional glaciovolcanic features promises further geologic constraints on ice sheet configuration. Field-based measurements of paleo-erosion and deposition rates are useful targets for improving constraints on the crustal loading history associated with sediment redistribution. Incorporating the latter changes in surface mass into the crustal stress modeling is another important goal.

Improving eruptive chronologies from additional volcanoes will provide additional information useful to refining the magma chamber model. Measurements of mineral compositions in key eruptive products spanning the last 70 kyr will facilitate application of several mineral-melt thermobarometers that, in parallel with rhyolite-MELTS thermodynamic modeling, will refine our current constraints on depths of magma crystallization and pre-eruptive storage from the Weber and Blundy (2024) thermobarometer.

Future work to improve our surface loading model will also focus on better constraining complex bedrock topography, which is key to understanding dike ascent. Moreover, accounting at higher spatial resolution for mass loading due to volcano growth, caldera collapse, or flank collapse, in parallel with ice loading/unloading, will improve models of subvolcanic stress evolution. From a trans-crustal plumbing system perspective, it will also be important to accommodate the rheological complexity of melts, mushes, and crustal rocks that vary with depth.

7.2. Implications for a habitable planet

Our findings thus far suggest that intracrustal stress relaxation associated with rapid deglaciation may propel 2–50 fold increases in the eruptive fluxes that are sustained over periods of several kyr at large composite continental arc front volcanoes (Fig. 4). Although difficult to quantify, the CO_2 concentrations of arc magmas can be up to 1.0 wt% at depths of crystallization and storage (Wallace et al., 2015). The amount of CO_2 flux emitted to the atmosphere from eruptions of subaerial volcanoes in magmatic arcs, hotspots, and rifts is estimated to be about 1.8×10^{12} mol/yr, or about 2 Tg of CO_2/yr, and is comparable to that of the output from the entire mid-ocean ridge sytstem (Fischer, 2008; Fischer et al., 2019). Although this current rate of CO_2 contributed by subaerial eruptions is only ~5 % of that emitted annually by the annual burning of fossil fuels at about 35 Tg of CO_2/yr (Gerlach, 2011), rapid deglaciation might be expected to increase atmospheric CO_2 concentrations over periods of several kyr on top of the anthropogenic addition, and thus contribute in a non-trivial way to longer term global warming. We anticipate that the example we have illustrated from the Andean SVZ and northernmost Patagonian ice sheet retreat will stimulate further work to characterize more quantitatively the impacts of ice sheet

loading and retreat on several other continental magmatic arcs, for example in Kamchatka, Hokkaido/Japan, the Alaskan Peninsula, and the Cascades, as well as within intraplate settings such as northern British Columbia (Edwards et al., 2020).

The magma chamber model developed here builds off one developed specifically to address the impact of subglacial volcanism in Antarctica (Coonin et al., 2024). The West Antarctic Ice Sheet (WAIS) is more susceptible to climate change, and thus more capable of contributing to sea level rise in the near future, than the remainder of ice sheets in Antarctica. It sits atop more than 100 topographic structures tentatively identified as volcanoes associated with the West Antarctic Rift System (van Wyk de Vries et al., 2018). Future thinning of the WAIS as atmospheric temperature increases could reduce crustal stresses on the underlying volcanic plumbing systems with the possibility of creating a feedback such that increasing rates of eruption could enhance ice sheet thinning via melting at the base of the ice (Coonin et al., 2024). Moreover, we anticipate that the field, laboratory, and modeling approaches we have presented here may prove useful in evaluating the contributions of continental arc magmatism to CO_2 outputs and climate changes over the last several hundred million years (e.g., Ratschbacher et al., 2019).

The increase in eruption frequency and rates of cone growth following the LGM in the CSVZ has led to widespread distribution of unconsolidated tephra deposits and oversteepened cliffs of lava flows on steep slopes through the landscape in Fig. 1b. In the context of a warming climate associated with more frequent and intense rainfall events (e.g., Towhata et al., 2021), many of these tephra deposits are unstable and can fail causing far-traveling landslides or debris flows (e.g., Somos-Valenzuela et al., 2020; Fustos-Toribio et al., 2021). Thus, widespread retreat of edifice-buttressing ice masses coupled with increased post-glacial volcanic output along the CSVZ may be a contributing factor in destabilizing volcanic massifs and significantly increasing the risk of mass flow inundation around many of these volcanoes.

CRediT authorship contribution statement

Brad S. Singer: Writing – review & editing, Writing – original draft, Visualization, Validation, Supervision, Resources, Project administration, Methodology, Investigation, Funding acquisition, Formal analysis, Data curation, Conceptualization. **Pablo Moreno-Yaeger:** Writing – review & editing, Visualization, Validation, Investigation. **Meredith Townsend:** Writing – review & editing, Writing – original draft, Visualization, Supervision, Methodology, Investigation, Funding acquisition, Formal analysis, Conceptualization. **Christian Huber:** Writing – review & editing, Writing – original draft, Visualization, Validation, Supervision, Software, Methodology, Investigation, Funding acquisition, Formal analysis, Conceptualization. **Joshua Cuzzone:** Writing – review & editing, Writing – original draft, Visualization, Validation, Software, Resources, Methodology, Investigation, Funding acquisition, Formal analysis, Conceptualization. **Benjamin R. Edwards:** Writing – review & editing, Writing – original draft, Visualization, Supervision, Project administration, Methodology, Investigation, Funding acquisition, Formal analysis, Conceptualization. **Matias Romero:** Writing – review & editing, Writing – original draft, Investigation, Formal analysis. **Yasmeen Orellana-Salazar:** Writing – original draft, Investigation. **Shaun A. Marcott:** Writing – review & editing, Writing – original draft, Visualization, Supervision, Project administration, Methodology, Investigation, Funding acquisition, Formal analysis, Conceptualization. **Rachel E. Breunig:** Writing – original draft, Visualization, Methodology, Investigation. **Ken L. Ferrier:** Writing – review & editing, Writing – original draft, Visualization, Supervision, Methodology, Investigation, Funding acquisition, Formal analysis, Conceptualization. **Kathryn Scholz:** Writing – original draft, Software, Methodology. **Brent V. Alloway:** Writing – review & editing, Resources, Investigation. **Marissa M. Tremblay:** Writing – review & editing, Supervision, Investigation, Funding acquisition. **Sally Stevens:** Visualization, Formal analysis. **Ivo Fustos-Toribio:** Resources, Methodology, Investigation.

Declaration of competing interest

The authors declare the following financial interests/personal relationships which may be considered as potential competing interests:

Brad Singer (lead PI) reports financial support was provided by National Science Foundation. If there are other authors, they declare that they have no known competing financial interests or personal relationships that could have appeared to influence the work reported in this paper.

Data availability

Data will be made available on request.

Acknowledgements

We thank Álex Alarcón of SERNAGEOMIN for support of our research in the SVZ during the past decade. We appreciate the hospitality of Bárbara Corrales and Pablo Saumann at Parque Los Ulmos, the management of the Fundación Huilo-Huilo preserve for permitting access to Mocho-Choshuenco, and CONAF for granting access to work in and collect samples from several national parks and reserves. Helicopter support from Jaime Fernández and Barraco Air has been invaluable to our efforts. We appreciate comments by David Pyle and an anonymous reviewer that helped to clarify many points. This work is supported by National Science Foundation grants from the Frontier Research in Earth Science program: EAR-2121570 (UW-Madison), EAR-2121655 (Brown), EAR-2122872 (Lehigh), EAR-2121537 (Dickinson), EAR-2121561 (UCLA) and EAR-2121372 (Purdue).

References

Åkesson, H., Morlighem, M., Nisancioglu, K.H., Svendsen, J.I., Mangerud, J., 2018. Atmosphere-driven ice sheet mass loss paced by topography: insights from modelling the south-western Scandinavian Ice Sheet. Quat. Sci. Rev. 195, 32–47.

Albino, F., Pinel, V., Sigmundsson, F., 2010. Influence of surface load variations on eruption likelihood: application to two Icelandic subglacial volcanoes, Grímsvötn and Katla. Geophys. J. Int. 181 (3), 1510–1524.

Alley, R., Cuffey, K., Zoet, L., 2019. Glacial erosion: status and outlook. Ann. Glaciol. https://doi.org/10.1017/aog.2019.38.

Alloway, B.V., Pearce, N.J., Villarosa, G., Outes, V., Moreno, P.I., 2015. Multiple melt bodies fed the AD 2011 eruption of Puyehue-Cordón Caulle, Chile. Nat. SR 5 (17589), 2015. https://doi.org/10.1038/srep17589.

Alloway, B.V., Pearce, N.J.G., Moreno, P.I., Villarosa, G., Jara, I., Ricardo De Pol-Holz, R., Outes, V., 2017a. An 18,000 year-long eruptive record from Volcán Chaitén, northwestern Patagonia: paleoenvironmental and hazard-assessment implications. Quat. Sci. Rev. 168, 151–181.

Alloway, B.V., Moreno, P.I., Pearce, N., Pol-Holz, De, Henríquez, W., Pesce, O., Sagredo, E., Villarosa, G., Outes, V., 2017b. Stratigraphy, age and correlation of Lepué tephra: a widespread c. 11,000 cal. a BP marker horizon sourced from the Chaitén Sector of southern Chile. J. Quat. Sci. 32, 795–829.

Alloway, B.V., Pearce, N.J., Moreno, P.I., Villarosa, G., Jara, I.A., Henríquez, C.A., Sagredo, E.A., Ryan, M.T., Outes, V., 2022. Refinement of the tephrostratigraphy straddling the northern Patagonian Andes (40–41° S): new tephra markers, reconciling different archives and ascertaining the timing of piedmont deglaciation. J. Quat. Sci. 37 (3), 441–477.

Andersen, B., Denton, G.H., Lowell, T.V., 1999. Glacial geomorphologic maps of Llanquihue drift in the area of the southern Lake District, Chile. Geogr. Ann. Ser. B 81, 155–166.

Arzilli, F., Morgavi, D., Petrelli, M., Polacci, M., Burton, M., Di Genova, D., Fellowes, J., 2019. The unexpected explosive sub-Plinian eruption of Calbuco volcano (22–23 April 2015; southern Chile): triggering mechanism implications. J. Volcanol. Geotherm. Res. 378, 35–50.

Aubry, T.J., Farquharson, J.I., Rowell, C.R., Watt, S.F., Pinel, V., Beckett, F., Fasullo, J., Hopcroft, P.O., Pyle, D.M., Schmidt, A., Sykes, J.S., 2022. Impact of climate change on volcanic processes: current understanding and future challenges. Bull. Volcanol. 84 (6), 58.

Bachmann, O., Huber, C., 2016. Silicic magma reservoirs in the Earth's crust. Am. Mineral. 101, 2377–2404.

Bachmann, O., Huber, C., 2019. The inner workings of crustal distillation columns; the physical mechanisms and rates controlling phase separation in silicic magma reservoirs. J. Petrol. 60, 3–18.

Bacon, C.R., Lanphere, M.A., 2006. Eruptive history and geochronology of Mount Mazama and the Crater Lake region. Oregon. Geological Society of America Bulletin 118, 1331–1359. https://doi.org/10.1130/B25906.1.
Barenblatt, G.I., 1962. The mathematical theory of equilibrium cracks in brittle fracture. Adv. Appl. Mech. 7, 55–129.
Bechon, T., Billon, M., Namur, O., Bolle, O., Fugmann, P., Foucart, H., Devidal, J.L., Delmelle, N., Vander Auwera, J., 2022. Petrology of the magmatic system beneath Osorno volcano (Central Southern Volcanic Zone, Chile). Lithos 426, 106777.
Bennett, M.R., Huddart, D., Gonzalez, S., 2009. Glaciovolcanic landsystems and large-scale glaciotectonic deformation along the Brekknafjöll–Jarlhettur, Iceland. Quat. Sci. Rev. 28 (7–8), 647–676.
Bertrand, S., Boes, X., Castiaux, J., et al., 2005. Temporal evolution of sediment supply in Lago Puyehue (Southern Chile) during the last 600 years and its climatic significance. Quat. Res. 64, 163–175.
Bertrand, S., Charlet, F., Charlier, B., et al., 2008. Climate variability of southern Chile since the Last Glacial Maximum: a continuous sedimentological record from Lago Puyehue (40°S). J. Paleolimnol. 39, 179–195.
Björnsson, H., 2016. The glaciers of Iceland: a historical, cultural and scientific overview. Atlantis Press. https://doi.org/10.2991/978-94-6239-207-6.
Boschetty, F.O., Ferguson, D.J., Cortés, J.A., Morgado, E., Ebmeier, S.K., Morgan, D.J., Romero, J.E., Silva Parejas, C., 2022. Insights into magma storage beneath a frequently erupting arc volcano (Villarrica, Chile) from unsupervised machine learning analysis of mineral compositions. Geochem. Geophys. Geosyst. 23 (4) p. e2022GC010333.
Boussinesq, J., 1885. Application des Potentials a l 'Etude de l 'Equilibre et du Mouvement des Solides Elastiques, 1885. Gauthier Villars, Paris.
Campos, A., Moreno, H., Muñoz, J., Antinao, J.L., Clayton, J., Martin, M., 1998. Area de Futrono-Lago Ranco, Región de Los Lagos: Servicio Nacional de Geología y Minería, Mapas Geológicos, v. 8, scale 1:100,000.
Cashman, K.V., Sparks, R.S.J., Blundy, J.D., 2017. Vertically extensive and unstable magmatic systems: a unified view of igneous processes. Science 355. https://doi.org/10.1126/science.aag3055 eaag3055.
Castro, J.M., Schipper, C.I., Mueller, S.P., Militzer, A., Amigo, A., Parejas, C.S., Jacob, D., 2013. Storage and eruption of near-liquidus rhyolite magma at Cordón Caulle, Chile. Bull. Volcanol. 75, 702.
Castruccio, A., Clavero, J., Segura, A., Samaniego, P., Roche, O., Le Pennec, J.L., Droguett, B., 2016. Eruptive parameters and dynamics of the April 2015 sub-Plinian eruptions of Calbuco volcano (southern Chile). Bull. Volcanol. 78, 1–19.
Chamberlain, K.J., Morgan, D.J., Lara, L.E., Walshaw, R., Gardner, J., Chenery, S., Millar, I.L., Wagner, D., 2024. Effect of crustal stress state on magmatic stalling and ascent: case study from Puyehue-Cordón Caulle, Chile. Bull. Volcanol. 86, 53.
Clark, P.U., Dyke, A.S., Shakun, J.D., Carlson, A.E., Clark, J., Wohlfarth, B., Mitrovica, J. X., Hostetler, S., McCabe, A.M., 2009. The Last Glacial Maximum. Science 325, 710–714. https://doi.org/10.1126/science.1172873.
Cole, R.P., White, J.D.L., Conway, C.E., Leonard, G.S., Townsend, D.B., Pure, L.R., 2018. The glaciovolcanic evolution of an andesitic edifice, South Crater, Tongariro volcano, New Zealand. J. Volcanol. Geotherm. Res. 352, 55–77.
Conway, C.E., Townsend, D.B., Leonard, G.S., Wilson, C.J.N., Calvert, A.T., Gamble, J.A., 2015. Lava-ice interaction on a large composite volcano: a case study from Ruapehu, New Zealand. Bull. Volcanol. 77, 21. https://doi.org/10.1007/s00445-015-0906-2.
Conway, C.E., Pure, L.R., Ishizuka, O., 2023. An assessment of potential causal links between deglaciation and eruption rates at arc volcanoes. Front. Earth Sci. 11 https://doi.org/10.3389/feart.2023.1082342.
Coonin, A.E., Huber, C., Troch, J., Townsend, M., Scholz, K., Singer, B.S., 2024. Magma reservoir response to ice unloading: Applications to volcanism in the West Antarctic Rift System. In: ESS Open Archive. Under revision G-cubed.
Cutler, K.S., Cassidy, M., Blundy, J.D., 2024. Plagioclase-saturated melt hygrothermobarometry and plagioclase-melt equilibria using machine learning. Geochem. Geophys. Geosyst. 25 (4) p.e2023GC011357.
Cuzzone, J.K., Schlegel, N.-J., Morlighem, M., Larour, E., Briner, J.P., Seroussi, H., Caron, L., 2019. The impact of model resolution on the simulated Holocene retreat of the southwestern Greenland ice sheet using the Ice Sheet System Model (ISSM). Cryosphere 13, 879–893.
Cuzzone, J., Romero, M., Marcott, S., 2024. Modeling the timing of Patagonian Ice Sheet retreat in the Chilean Lake District from 22–10 ka. Cryosphere 18, 1381–1398.
Dalca, A.V., Ferrier, K.L., Mitrovica, J.X., Perron, J.T., Milne, G.A., Creveling, J.R., 2013. On postglacial sea level—III. Incorporating sediment redistribution. Geophys. J. Int. 194, 45–60.
Davies, B.J., Darvill, C.M., Lovell, H., Bendle, J.M., Dowdeswell, J.A., Fabel, D., García, J. L., Geiger, A., Glasser, N.F., Gheorghiu, D.M., Harrison, S., 2020. The evolution of the Patagonian Ice Sheet from 35 ka to the present day (PATICE). Earth Sci. Rev., 103152
Degruyter, W., Huber, C., 2014. A model for eruption frequency of upper crustal silicic magma chambers. Earth Planet. Sci. Lett. 403, 117–130. https://doi.org/10.1016/j.epsl.2014.06.047.
Denton, G.H., Lowell, T., Heusser, C., Schlüchter, C., Andersen, B.G., Heusser, L.E., Moreno, P.I., Marchant, D.R., 1999. Geomorphology, stratigraphy, and radiocarbon chronology of Llanquihue Drift in the area of the Southern Lake District, Seno Reloncaví, and Isla Grande de Chiloé, Chile. Geogr. Ann. Ser. B 81, 167–229.
DeSilva, C.M., Singer, B.S., Alloway, B.V., Moreno-Yaeger, P., 2023. Origin of the compositionally zoned Paso Puyehue Tephra, Antillanca Volcanic Complex, Chile. J. Volcanol. Geotherm. Res. 444, 107943.
Dias dos Santos, T., Morlighem, M., Brinkerhoff, D., 2022. A new vertically integrated MOno-Layer Higher-Order (MOLHO) ice flow model. Cryosphere 16 (1).
Díaz, C., Moreno, P.I., Villacís, L.A., Sepúlveda-Zúñiga, E.A., Maidana, N.I., 2023. Freshwater diatom evidence for Southern Westerly Wind evolution since ~18 ka in northwestern Patagonia. Quat. Sci. Rev. 316, 108231.
Doll, P., Eaves, S.R., Kennedy, B.M., Blard, P.H., Nichols, A.R.L., Leonard, G.S., Townsend, D.B., Cole, J.W., Conway, C.E., Baldwin, S., Fénisse, G., 2024. Cosmogenic ^{3}He chronology of postglacial lava flows at Mt. Ruapehu, New Zealand. Geochronology 6, 365–395. https://doi.org/10.5194/gchron-6-365-2024.
Edwards, B.R., Russell, J.K., Jicha, B., Singer, B.S., Dunnington, G., Jensen, R., 2020. A 3 million year record of volcanism and glaciation in northern British Columbia, Canada. Geol. Soc. Am. Spec. Pap. 548, 231–258.
Eksinchol, I., Rudge, J.F., Maclennan, J., 2019. Rate of melt ascent beneath iceland from the magmatic response to deglaciation. Geochem. Geophys. Geosyst. 20, 2585–2605.
Ferrier, K.L., West, N., 2017. Responses of chemical erosion rates to transient perturbations in physical erosion rates, and implications for relationships between chemical and physical erosion rates in regolith-mantled hillslopes. Earth Planet. Sci. Lett. 474, 447–456.
Ferrier, K.L., Huppert, K.L., Perron, J.T., 2013a. Climatic control of bedrock river incision. Nature 496, 206.
Ferrier, K.L., Perron, J.T., Mukhopadhyay, S., Rosener, M., Stock, J.D., Huppert, K.L., Slosberg, M., 2013b. Covariation of climate and long-term erosion rates across a steep rainfall gradient on the Hawaiian island of Kaua 'i. Geol. Soc. Am. Bull. 125, 1146–1163.
Ferrier, K.L., Austermann, J., Mitrovica, J.X., Pico, T., 2017. Incorporating sediment compaction into a gravitationally self-consistent model for ice age sea-level change. Geophys. J. Int. 211, 663–672.
Fischer, T.P., 2008. Fluxes of volatiles (H_2O, CO_2, N_2, Cl, F) from arc volcanoes. Geochem. J. 42, 21–38.
Fischer, T.P., Arellano, S., Carn, S., Aiuppa, A., Galle, B., Allard, P., Lopez, T., Shinohara, H., Kelly, P., Werner, C., Cardellini, C., 2019. The emissions of CO_2 and other volatiles from the world's subaerial volcanoes. Sci. Rep. 9, 18716.
Florez, D., Huber, C., Hoyos, S., Pec, M., Parmentier, E.M., Connolly, J.A.D., Hirth, G., 2024a. Repacking in compacting mushes at intermediate melt fractions: constraints from numerical modeling and phase separation experiments on granular media. J. Geophys. Res. Solid Earth 129, e2024JB029077. https://doi.org/10.1029/2024JB029077.
Florez, D., Huber, C., Bachmann, O., Sigworth, A., Claiborne, L., Miller, C., 2024b. Repacking-Driven Compaction in the Spirit Mountain Batholith, Southern Nevada. https://d197for5662m48.cloudfront.net/documents/publicationstatus/203280/preprint_pdf/ba7e21e4ea8e5d64cb0f7f6758198da8.pdf.
Fontijn, K., Lachowycz, S.M., Rawson, H., Pyle, D.M., Mather, T.A., Naranjo, J.A., Moreno-Roa, H., 2014. Late Quaternary tephrostratigraphy of southern Chile and Argentina. Quat. Sci. Rev. 89, 70–84. https://doi.org/10.1016/j.quascirev.2014.02.007.
Fontijn, K., Rawson, H., Van Daele, M., Moernaut, J., Abarzúa, A.M., Heirman, K., Bertrand, S., Mather, T.A., De Batist, M., Naranjo, J., Moreno, H., 2016. Synchronisation of sedimentary records using tephra: a postglacial tephrochronological model for the Chilean Lake District. Quat. Sci. Rev. 137, 234–254. https://doi.org/10.1016/j.quascirev.2016.02.015.
Fustos-Toribio, I.J., Morales-Vargas, B., Somos-Valenzuela, M., Moreno-Yaeger, P., Muñoz-Ramirez, R., Rodriguez Araneda, I., Chen, N., 2021. Debris flow event on Osorno volcano, Chile, during summer 2017: new interpretations for chain processes in the southern Andes. Nat. Hazards Earth Syst. Sci. Discuss. 21, 1–23.
Gayer, E., Michon, L., Louvat, P., Gaillardet, J., 2019. Storm-induced precipitation variability control of long-term erosion. Earth Planet. Sci. Lett. 517, 61–70.
Geoffroy, C.A., Alloway, B.V., Amigo, Á., Parada, M.A., Gutierrez, F., Castruccio, A., Pearce, N.J.G., Morgado, E., Moreno, P.I., 2018. A widespread compositionally bimodal tephra sourced from Volcán Melimoyu (44°S, Northern Patagonian Andes): insights into magmatic reservoir processes and opportunities from regional correlation. Quat. Sci. Rev. 200, 141–159. https://doi.org/10.1016/j.quascirev.2018.09.034.
Gerlach, T., 2011. Volcanic versus anthropogenic carbon dioxide. EOS Trans. Am. Geophys. Union 92, 201–202.
Gerlach, D.C., Frey, F.A., Moreno-Roa, H., Lopez-Escobar, L., 1988. Recent Volcanism in the Puyehue-Cordón Caulle Region, Southern Andes, Chile (40.5° S): petrogenesis of Evolved Lavas. J. Petrol. 29, 333–382.
Geyer, A., Bindeman, I., 2011. Glacial influence on caldera-forming eruptions. J. Volcanol. Geotherm. Res. 202, 127–142.
Glasser, N.F., Jansson, K.N., Harrison, S., Kleman, J., 2008. The glacial geomorphology and Pleistocene history of South America between 38 S and 56 S. Quat. Sci. Rev. 27, 365–390.
Glazner, A.F., Manley, C.R., Marron, J.S., Rojstaczer, S., 1999. Fire or ice: anticorrelation of volcanism and glaciation in California over the past 800,000 years. Geophys. Res. Lett. 26, 1759–1762. https://doi.org/10.1029/1999GL900333.
Gualda, G.A., Ghiorso, M.S., Lemons, R.V., Carley, T.L., 2012. Rhyolite-MELTS: a modified calibration of MELTS optimized for silica-rich, fluid-bearing magmatic systems. J. Petrol. 53, 875–890.
Gualda, G.A., Gravley, D.M., Deering, C.D., Ghiorso, M.S., 2019. Magma extraction pressures and the architecture of volcanic plumbing systems. Earth Planet. Sci. Lett. 522, 118–124.
Hall, K., 1982. Rapid deglaciation as an initiator of volcanic activity: an hypothesis. Earth Surf. Process. Landf. 7, 45–51.
Hallet, B., Hunter, L., Bogen, J., 1996. Rates of erosion and sediment evacuation by glaciers: a review of field data and their implications. Glob. Planet. Chang. 12, 213–235.

He, F., Shakun, J.D., Clark, P.U., Carlson, A.E., Liu, Z., Otto-Bliesner, B.L., Kutzbach, J.E., 2013. Northern Hemisphere forcing of Southern Hemisphere climate during the last deglaciation. Nature 494, 81–85. https://doi.org/10.1038/nature11822.

Hein, A.S., Hulton, N.R.J., Dunai, T.J., Sugden, D.E., Kaplan, M.R., Xu, S., 2010. The chronology of the Last Glacial Maximum and deglacial events in central Argentine Patagonia. Quat. Sci. Rev. 29, 1212–1227. https://doi.org/10.1016/j.quascirev.2010.01.020.

Heirman, K., De Batist, M., Charlet, F., Moernaut, J., Chapron, E., Brümmer, R., Urrutia, R., 2011. Detailed seismic stratigraphy of Lago Puyehue: implications for the mode and timing of glacier retreat in the Chilean Lake District. J. Quat. Sci. 26, 665–674.

Hickey-Vargas, R., Roa, H.M., Escobar, L.L., Frey, F.A., 1989. Geochemical variations in Andean basaltic and silicic lavas from the Villarrica-Lanin volcanic chain (39.5 S): an evaluation of source heterogeneity, fractional crystallization and crustal assimilation. Contrib. Mineral. Petrol. 103, 361–386.

Hickey-Vargas, R., Holbik, S., Tormey, D., Frey, F.A., Roa, H.M., 2016. Basaltic rocks from the Andean Southern Volcanic Zone: insights from the comparison of along-strike and small-scale geochemical variations and their sources. Lithos 258, 115–132.

Hubbard, A., Hein, A.S., Kaplan, M.R., Hulton, N.R., Glasser, N., 2005. A modelling reconstruction of the last glacial maximum ice sheet and its deglaciation in the vicinity of the Northern Patagonian Icefield, South America. Geogr. Ann. Ser. B 87, 375–391.

Huber, C., Townsend, M., Degruyter, W., Bachmann, O., 2019. Optimal depth of subvolcanic magma chamber growth controlled by volatiles and crust rheology. Nat. Geosci. 12, 762–768.

Hulton, N., Sugden, D., Payne, A., Clapperton, C., 1994. Glacier modeling and the climate of Patagonia during the last glacial maximum. Quat. Res. 42, 1–19.

Huybers, P., Langmuir, C., 2009. Feedback between deglaciation, volcanism, and atmospheric CO2. Earth Planet. Sci. Lett. 286, 479–491. https://doi.org/10.1016/j.epsl.2009.07.014.

Huybers, P., Langmuir, C.H., 2017. Delayed CO_2 emissions from mid-ocean ridge volcanism as a possible cause of late-Pleistocene glacial cycles. Earth Planet. Sci. Lett. 457, 238–249.

Jay, J., Costa, F., Pritchard, M., Lara, L., Singer, B., Herrin, J., 2014. Locating magma reservoirs using InSAR and petrology before and during the 2011–2012 Cordón Caulle silicic eruption. Earth Planet. Sci. Lett. 395, 254–266.

Jefferson, A.J., Ferrier, K.L., Perron, J.T., Ramalho, R., 2014. Controls on the hydrological and topographic evolution of shield volcanoes and volcanic ocean islands. The Galapagos: A natural laboratory for the Earth Sciences. In: Harpp, Karen S., Mittelstaedt, Eric, d'Ozouville, Noémi, Graham, David W. (Eds.), Geophysical Monograph 204 American Geophysical Union, pp. 185–213.

Jellinek, A.M., DePaolo, D.J., 2003. A model for the origin of large silicic magma chambers: precursors of caldera-forming eruptions. Bull. Volcanol. 65, 363–381.

Jellinek, A.M., Manga, M., Saar, M.O., 2004. Did melting glaciers cause volcanic eruptions in eastern California? Probing the mechanics of dike formation. J. Geophys. Res. Solid Earth 109, B09206. https://doi.org/10.1029/2004JB002978.

Jicha, B.R., Singer, B.S., Beard, B.L., Johnson, C.M., Moreno-Roa, H., Naranjo, J.A., 2007. Rapid magma ascent and generation of ^{230}Th excesses in the lower crust at Puyehue–Cordón Caulle, Southern Volcanic Zone, Chile. Earth Planet. Sci. Lett. 255, 229–242.

Jicha, B., Singer, B.S., Sobol, P., 2016. Re-evaluation of the ages of 40Ar/39Ar sanidine standards and supereruptions in the western U.S. using a Noblesse multi-collector mass spectrometer. Chemical Geology 431, 56–66. https://doi.org/10.1016/j.chemgeo.2016.03.024.

Jull, M., McKenzie, D., 1996. The effect of deglaciation on mantle melting beneath Iceland. J. Geophys. Res. Solid Earth 101, 21815–21828.

Kaplan, M.R., Ackert Jr., R.P., Singer, B.S., Douglass, D.C., Kurz, M.D., 2004. Cosmogenic nuclide chronology of millennial-scale glacial advances during O-isotope stage 2 in Patagonia. Geol. Soc. Am. Bull. 116, 308–321.

Kaplan, M., Moreno, P.I., Rojas, M., 2008. Glacial dynamics in southernmost South America during Marine Isotope Stage 5e to the Younger Dryas chron: a brief review with a focus on cosmogenic nuclide measurements. Journal of Quaternary Science 23, 649–658. https://doi.org/10.1002/jqs.1209.

Kelman, M.C., Russell, J.K., Hickson, C.J., 2002. Glaciovolcanism at Ember Ridge, Mount Cayley Volcanic Field, Southwestern British Columbia. Natural Resources Canada, Geological Survey of Canada.

Klug, J.D., Ramirez, A., Singer, B.S., Jicha, B.R., Mixon, E.E., Martinez, P., 2022. Intercalibration of the Servicio Nacional de Geología y Minería (SERNAGEOMIN), Chile and WiscAr ^{40}Ar/^{39}Ar laboratories for Quaternary dating. Quat. Geochronol. 72 https://doi.org/10.1016/j.quageo.2022.101354.

Koppes, M.N., Montgomery, D.R., 2009. The relative efficacy of fluvial and glacial erosion over modern to orogenic timescales. Nat. Geosci. 2, 644–647.

Kutterolf, Steffen, Jegen, M., Mitrovica, J.X., Kwasnitschka, T., Freundt, A., Huybers, P. J., 2013. A detection of Milankovitch frequencies in global volcanic activity. Geology 41, 227–230. https://doi.org/10.1130/G33419.1.

Kutterolf, S., Schindlbeck, J.C., Jegen, M., Freundt, A., Straub, S.M., 2019. Milankovitch frequencies in tephra records at volcanic arcs: the relation of kyr-scale cyclic variations in volcanism to global climate changes. Quat. Sci. Rev. 204, 1–16. https://doi.org/10.1016/j.quascirev.2018.11.004.

Lachowycz, S.M., Pyle, D.M., Gilbert, J.S., Mather, T.A., Mee, K., Naranjo, J.A., Hobbs, L. K., 2015. Glaciovolcanism at Volcán Sollipulli, southern Chile: Lithofacies analysis and interpretation. J. Volcanol. Geotherm. Res. 303, 59–78.

Larour, E., Seroussi, H., Morlighem, M., Rignot, E., 2012. Continental scale, high order, high spatial resolution, ice sheet modeling using the Ice Sheet System Model (ISSM). J. Geophys. Res. Earth 117 (F1).

Laugenie, C., 1982. La region des lacs, Chili meridional. Universite de Bordeaux III, Bordeaux, France, 822 pp.

Leger, T.P., Hein, A.S., Goldberg, D., Schimmelpfennig, I., Van Wyk de Vries, M.S., Bingham, R.G., ASTER Team, 2021. Northeastern Patagonian glacier advances (43° S) reflect northward migration of the Southern Westerlies towards the end of the last glaciation. Front. Earth Sci. 9, 751987.

Lescinsky, D.T., Fink, J.H., 2000. Lava and ice interaction at stratovolcanoes: use of characteristic features to determine past glacial extents and future volcanic hazards. J. Geophys. Res. Solid Earth 105, 23711–23726.

Lescinsky, D.T., Sisson, T.W., 1998. Ridge-forming, ice-bounded lava flows at Mount Rainier. Wash. Geol. 26 (4), 351–354.

Licciardi, J.M., Denoncourt, C.L., Finkel, R.C., 2007. Cosmogenic 36Cl production rates from Ca spallation in Iceland. Earth and Planetary Science Letters 267, 365–377. https://doi.org/10.1016/j.epsl.2007.11.036.

Lisiecki, L.E., Raymo, M.E., 2005. A Pliocene-Pleistocene stack of 57 globally distributed benthic δ18O records. Paleoceanography 20, PA1003. https://doi.org/10.1029/2004PA001071.

Liu, Z., Otto-Bliesner, B.L., He, F., Brady, E.C., Tomas, R., Clark, P.U., Carlson, A.E., Lynch-Stieglitz, J., Curry, W., Brook, E., Erickson, D., 2009. Transient simulation of last deglaciation with a new mechanism for Bølling-Allerød warming. Science 325, 310–314.

Lohmar, S., Parada, M., Gutiérrez, F., Robin, C., Gerbe, M.C., 2012. Mineralogical and numerical approaches to establish the pre-eruptive conditions of the mafic Licán Ignimbrite, Villarrica Volcano (Chilean Southern Andes). J. Volcanol. Geotherm. Res. 235–236, 55–69. https://doi.org/10.1016/j.jvolgeores.2012.05.006.

López-Escobar, L., Cembrano, J., Moreno, H., 1995. Geochemistry and tectonics of the Chilean Southern Andes basaltic Quaternary volcanism (37-46°S). Andean Geology 22, 219–234.

Lowell, T., Heusser, C., Andersen, B., Moreno, P., Hauser, A., Heusser, L., Schlüchter, C., Marchant, D., Denton, G., 1995. Interhemispheric correlation of late Pleistocene glacial events. Science 269, 1541–1549.

Lucas, L.C., Albright, J.A., Gregg, P.M., Zhan, Y., 2022. The impact of ice caps on the mechanical stability of magmatic systems: implications for forecasting on human timescales. Front. Earth Sci. 10, 868569.

Maclennan, J., Jull, M., McKenzie, D., Slater, L., Grönvold, K., 2002. The link between volcanism and deglaciation in Iceland. Geochem. Geophys. Geosyst. 3, 1–25. https://doi.org/10.1029/2001GC000282.

Martin, J.R., Davies, B.J., Thorndycraft, V.R., 2019. Glacier dynamics during a phase of Late Quaternary warming in Patagonia reconstructed from sediment-landform associations. Geomorphology 337, 111–133.

Martínez, P., Singer, B.S., Roa, H.M., Jicha, B.R., 2018. Volcanologic and petrologic evolution of Antuco-Sierra Velluda, Southern Andes, Chile. J. Volcanol. Geotherm. Res. 349, 392–408.

Mathews, W.H., 1947. "Tuyas", flat-topped volcanoes in northern British Columbia. The American Journal of Science, 245, 560-570. 10.2475/ajs.245.9.560.

Matthews, R.K., 1968. Tectonic implications of glacio-eustatic sea level fluctuations. Earth Planet. Sci. Lett. 5, 459–462.

McMillan, N.J., Harmon, R.S., Moorbath, S., Lopez-Escobar, L., 1989. Crustal sources involved in continental arc magmatism: a case study of volcan Mocho-Choshuenco, southern Chile. Geology 17, 1152–1156.

Mixon, E.E., Singer, B.S., Jicha, B.R., Ramirez, A., 2021. Calbuco, a monotonous andesitic high-flux volcano in the Southern Andes. J. Volcanol. Geotherm. Res. 416, 107279 https://doi.org/10.1016/j.jvolgeores.2021.107279.

Moon, S., Perron, J., Martel, S., Holbrook, W., St. Clair, J., 2017. A model of three-dimensional topographic stresses with implications for bedrock fractures, surface processes, and landscape evolution. J. Geophys. Res. Earth 122, 823–846.

Mora, D., Tassara, A., 2018. Upper crustal decompression due to deglaciation-induced flexural unbending and its role on post-glacial volcanism at the Southern Andes. Geophys. J. Int. 216, 1549–1559.

Mora, D., Tassara, A., 2019. Upper crustal decompression due to deglaciation-induced flexural unbending and its role on post-glacial volcanism at the Southern Andes. Geophysical Journal International 216 (3), 1549–1559.

Moreno, P.I., 2020. Timing and structure of vegetation, fire, and climate changes on the Pacific slope of northwestern Patagonia since the last glacial termination. Quat. Sci. Rev. 238, 106328.

Moreno, R.H., Lara, P.L., 2007. Geología del Complejo Volcánico Mocho-Choshuenco, región de Los Ríos. In: Servicio Nacional de Geología y Minería, Carta Geológica de Chile, Serie Geología Básica, v. 107, 1 sheet, scale 1:50,000.

Moreno, P.I., Lowell, T.V., Jacobson Jr., G.L., Denton, G.H., 1999. Abrupt vegetation and climate changes during the last glacial maximumand last termination in the chilean lake district: a case study from canal de la puntilla (41 s). Geogr. Ann. A 81, 285–311.

Moreno, P.I., Denton, G.H., Moreno, H., Lowell, T.V., Putnam, A.E., Kaplan, M.R., 2015. Radiocarbon chronology of the last glacial maximum and its termination in northwestern Patagonia. Quat. Sci. Rev. 122, 233–249. https://doi.org/10.1016/j.quascirev.2015.05.027.

Moreno, P.I., Videla, J., Valero-Garcés, B., Alloway, B.V., Heusser, L.E., 2018. A continuous record of vegetation, fire-regime and climatic changes in northwestern Patagonia spanning the last 25,000 years. Quat. Sci. Rev. 198, 15–36.

Moreno, P.I., Lambert, F., Hernández, L., Villa-Martínez, R.P., 2023. Environmental evolution of western Tierra del Fuego (~ 54° S) since ice-free conditions and its zonal/hemispheric implications. Quat. Sci. Rev. 322, 108387.

Moreno, P.I., Gonzalorena, L.A., Hernández, L., 2024. Climatic and disturbance impacts on temperate rainforest development since~ 18 ka in central-west Isla Grande de Chiloé (42.7° S). Quat. Sci. Rev. 333, 108688.

Moreno-Yaeger, P., Singer, B.S., Edwards, B.R., Jicha, B.R., Nachlas, W.O., Kurz, M.D., Breunig, R., Fustos-Toribio, I., Vasquez Antipán, D., Piergrossi, E., 2024. Pleistocene to recent evolution of Mocho-Choshuenco volcano during growth and retreat of the Patagonian Ice Sheet. Geol. Soc. Am. Bull. https://doi.org/10.1130/B37514.1.

Morgado, E., Morgan, D.J., Castruccio, A., Ebmeier, S.K., Parada, M.-Á., Brahm, R., Harvey, J., Gutiérrez, F., Walshaw, R., 2019a. Old magma and a new, intrusive trigger: using diffusion chronometry to understand the rapid-onset Calbuco eruption, April 2015 (Southern Chile). Contrib. Mineral. Petrol. 174, 61. https://doi.org/10.1007/s00410-019-1596-0.

Morgado, E., Morgan, D.J., Harvey, J., Parada, M.-Á., Castruccio, A., Brahm, R., Gutiérrez, F., Georgiev, B., Hammond, S.J., 2019b. Localised heating and intensive magmatic conditions prior to the 22–23 April 2015 Calbuco volcano eruption (Southern Chile). Bull. Volcanol. 81, 24. https://doi.org/10.1007/s00445-019-1280-2.

Muir, R., Eaves, S., Vargo, L., Anderson, B., Mackintosh, A., Sagredo, E., Soteres, R., 2023. Late glacial climate evolution in the Patagonian Andes (44–47° S) from alpine glacier modelling. Quat. Sci. Rev. 305, 108035.

Nakada, M., Yokose, H., 1992. Ice age as a trigger of active Quaternary volcanism and tectonism. Tectonophysics 212, 321–329.

Namur, O., Montalbano, S., Bolle, O., Vander Auwera, J., 2020. Petrology of the April 2015 Eruption of Calbuco Volcano, Southern Chile. J. Petrol. 61, egaa084 https://doi.org/10.1093/petrology/egaa084.

Naranjo, J., Singer, B., Jicha, B., Moreno, H., Lara, L., 2017. Holocene tephra succession of Puyehue-Cordón Caulle and Antillanca/Casablanca volcanic complexes, southern Andes (40–41 S). J. Volcanol. Geotherm. Res. 332, 109–128.

NASA Shuttle Radar Topography Mission, 2013. Shuttle Radar Topography Mission (SRTM) Global. Distributed by OpenTopography. https://doi.org/10.5069/G9445JDF.

Nowell, D.A., Jones, M.C., Pyle, D.M., 2006. Episodic quaternary volcanism in France and Germany. J. Quat. Sci. 21, 645–675.

Nyland, R.E., Panter, K.S., Rocchi, S., Di Vincenzo, G., Del Carlo, P., Tiepolo, M., Field, B., Gorsevski, P., 2013. Volcanic activity and its link to glaciation cycles: Single-grain age and geochemistry of Early to Middle Miocene volcanic glass from ANDRILL AND-2A core, Antarctica. Journal of Volcanology and Geothermal Research 250, 106–128.

Pérez-Gussinyé, M., Lowry, A.R., Phipps Morgan, J., Tassara, A., 2008. Effective elastic thickness variations along the Andean margin and their relationship to subduction geometry. Geochem. Geophys. Geosyst. 9 (2).

Pesce, O.H., Moreno, P.I., 2014. Vegetation, fire and climate change in central-east Isla Grande de Chiloé (43 S) since the Last Glacial Maximum, northwestern Patagonia. Quat. Sci. Rev. 90, 143–157.

Pinel, V., Jaupart, C., 2000. The effect of edifice load on magma ascent beneath a volcano. Philos. Trans. R. Soc. London, Ser. A 358 (1770), 1515–1532.

Pinel, V., Jaupart, C., 2004. Magma storage and horizontal dyke injection beneath a volcanic edifice. Earth Planet. Sci. Lett. 221 (1–4), 245–262.

Porter, S.C., 1981. Pleistocene Glaciation in the Southern Lake District of Chile. Quat. Res. 16, 263–292. https://doi.org/10.1016/0033-5894(81)90013-2.

Putirka, K.D., 2008. Thermometers and Barometers for volcanic systems. Rev. Mineral. Geochem. 69, 61–120. https://doi.org/10.2138/rmg.2008.69.3.

Putirka, K.D., 2016. Amphibole thermometers and barometers for igneous systems and some implications for eruption mechanisms of felsic magmas at arc volcanoes. Am. Mineral. 101, 841–858.

Putirka, K.D., 2017. Down the crater: where magmas are stored and why they erupt. Elements 13 (1), 11–16.

Rampino, M.R., Self, S., Fairbridge, R.W., 1979. Can rapid climate change cause volcanic eruptions? Science 206, 826–829. https://doi.org/10.1126/science.206.4420.826.

Rasmussen, D.J., Plank, T.A., Roman, D.C., Zimmer, M.M., 2022. Magmatic water content controls the pre-eruptive depth of arc magmas. Science 375 (6585), 1169–1172.

Ratschbacher, B.C., Paterson, S.R., Fischer, T.P., 2019. Spatial and depth-dependent variations in magma volume addition and addition rates to continental arcs: application to global CO_2 fluxes since 750 Ma. Geochem. Geophys. Geosyst. 20, 2997–3018.

Rawson, H., Naranjo, J.A., Smith, V.C., Fontijn, K., Pyle, D.M., Mather, T.A., Moreno, H., 2015. The frequency and magnitude of post-glacial explosive eruptions at Volcán Mocho-Choshuenco, southern Chile. J. Volcanol. Geotherm. Res. 299, 103–129. https://doi.org/10.1016/j.jvolgeores.2015.04.003.

Rawson, H., Pyle, D.M., Mather, T.A., Smith, V.C., Fontijn, K., Lachowycz, S.M., Naranjo, J.A., 2016. The magmatic and eruptive response of arc volcanoes to deglaciation: insights from southern Chile. Geology 44, 251–254. https://doi.org/10.1130/G37504.1.

Ridolfi, F., Renzulli, A., Puerini, M., 2010. Stability and chemical equilibrium of amphibole in calc-alkaline magmas: an overview, new thermobarometric formulations and application to subduction-related volcanoes. Contrib. Mineral. Petrol. 160, 45–66.

Rocchi, I., Tomassini, A., Masotta, M., Petrelli, M., Ágreda López, M., Rocchi, S., 2024. Textures and chemistry of crystal cargo of The Pleiades Volcanic Field, Antarctica: potential influence of ice load in modulating the plumbing system. J. Petrol., egae027 https://doi.org/10.1093/petrology/egae027.

Rodríguez, C., Pérez, Y., Moreno, H., Clayton, J., Antinao, J., Duhart, P., Martin, M., 1999. Área de Panguipulli-Riñihue, Región de Los Lagos. Servicio Nacional de Geología y Minería, Mapas Geológicos, v. 10, scale 1:100,000.

Rodríguez-López, L., Alvarez, D., Bustos Usta, D., Duran-Llacer, I., Bravo Alvarez, L., Fagel, N., Urrutia, R., 2024. Chlorophyll-a detection algorithms at different depths using in situ, meteorological, and remote sensing data in a Chilean Lake. Remote Sens. 16, 647.

Romero, J.E., Alloway, B.V., Gutiérrez, R., Bertín, D., Castruccio, A., Villarrosa, G., Swanson, F., Schipper, I., Guevara, A., Bustillos, J., Pisello, A., Daga, R., Montiel, M., Gleeman, E., González, M., Morgavi, D., Ribeiro, S., Mella, M., 2021. Centennial scale eruptive diversity at Volcán Calbuco (41.3°S, Northwest Patagonia), deduced from historic tephra cover-bed and dendrochronologic archives. J. Volcanol. Geotherm. Res. 417, 107281.

Romero, M., Cuzzone, J., Jones, A.G., Marcott, S.A., 2024. Cosmogenic nuclide constraints on the Patagonian Ice Sheet demise during the last deglaciation. In: Goldschmidt Conference Abstracts, 13eP1. https://conf.goldschmidt.info/goldschmidt/2024/meetingapp.cgi/Paper/24183.

Rubin, A.M., 1993. On the thermal viability of dikes leaving magma chambers. Geophys. Res. Lett. 20, 257–260.

Satow, C., Gudmundsson, A., Gertisser, R., Bronk Ramsey, C., Bazargan, M., Pyle, D.M., Wulf, S., Miles, A.J., Hardiman, M., 2021. Eruptive activity of the Santorini Volcano controlled by sea-level rise and fall. Nature Geoscience 14, 586–592. https://doi.org/10.1038/s41561-021-00783-4.

Schachtman, N.S., Roering, J.J., Marshall, J.A., Gavin, D.G., Granger, D.E., 2019. The interplay between physical and chemical erosion over glacial-interglacial cycles. Geology 47, 613–616.

Schindlbeck, J.C., Jegen, M., Freundt, A., Kutterolf, S., Straub, S.M., Mleneck-Vautravers, M.J., McManus, J.F., 2018. 100- kyr cyclicity in volcanic ash emplacement: evidence from a 1.1 Myr tephra record from the NW Pacific. Sci. Rep. 8, 4440. https://doi.org/10.1038/s41598-018-22595-0.

Scholz, K., Townsend, M., Huber, C., Troch, J., Bachmann, O., Coonin, A.N., 2023. Investigating the impact of an exsolved H_2O-CO_2 phase on magma chamber growth and longevity: a thermomechanical model. Geochem. Geophys. Geosyst. 24 (12) p. e2023GC011151.

Seguinot, J., Rogozhina, I., Stroeven, A.P., Margold, M., Kleman, J., 2016. Numerical simulations of the Cordilleran ice sheet through the last glacial cycle. Cryosphere 10, 639–664.

Sellés, D., Moreno, H., 2011. Geología del Volcán Calbuco, Región de Los Lagos. Carta Geológica de Chile. Servicio Nacional de Geología y Minería, Subdirección Nacional de Geología.

Seropian, G., Schipper, C.I., Harmon, L.J., Smithies, S.L., Kennedy, B.M., Castro, J.M., Alloway, B.V., Forte, P., 2021. A century of ongoing silicic volcanism at Cordón Caulle, Chile: new constraints on the magmatic system involved in the 1921–1922, 1960 and 2011–2012 eruptions. J. Volcanol. Geotherm. Res. 420, 107406.

Sielfeld, G., Lange, D., Cembrano, J., 2019. Intra-arc crustal seismicity: seismotectonic implications for the Southern Andes Volcanic Zone, Chile. Tectonics 38, 552–578.

Sigvaldasson, G.E., Annertz, K., Nilsson, M., 1992. Effect of glacier loading/deloading on volcanism: postglacial volcanic production rate of the Dyngjufjöll area, Central Iceland. Bull. Volcanol. 54, 385–392.

Singer, B.S., Thompson, R.A., Dungan, M.A., Feeley, T.C., Nelson, S.T., Pickens, J.C., Metzger, J., 1997. Volcanism and erosion during the past 930 ky at the Tatara–San Pedro complex, Chilean Andes. Geol. Soc. Am. Bull. 109, 127–142.

Singer, B.S., Jicha, B.R., Harper, M.A., Naranjo, J.A., Lara, L.E., Moreno-Roa, H., 2008. Eruptive history, geochronology, and magmatic evolution of the Puyehue-Cordón Caulle volcanic complex, Chile. Geol. Soc. Am. Bull. 120, 599–618. https://doi.org/10.1130/B26276.1.

Skilling, I.P., 2009. Subglacial to emergent basaltic volcanism at Hlöðufell, south-West Iceland: a history of ice-confinement. J. Volcanol. Geotherm. Res. 185 (4), 276–289.

Smellie, J.L., Edwards, B.R., 2016. Glaciovolcanism on Earth and Mars. Cambridge University Press.

Smellie, J.L., Rocchi, S., Armienti, P., 2011. Late Miocene volcanic sequences in northern Victoria Land, Antarctica: products of glaciovolcanic eruptions under different thermal regimes. Bull. Volcanol. 73, 1–25.

Smellie, J.L., Rocchi, S., Di Vincenzo, G., 2023. Controlling influence of water and ice on eruptive style and edifice construction in the Mount Melbourne Volcanic Field (northern Victoria Land, Antarctica). Front. Earth Sci. 10, 1061515.

Somos-Valenzuela, M.A., Oyarzún-Ulloa, J.E., Fustos-Toribio, I.J., Garrido-Urzua, N., Ningsheng, C., 2020. Hidden Hazards: the conditions that potentially enabled the mudflow disaster at Villa Santa Lucía in Chilean Patagonia. Nat. Hazards Earth Syst. Sci. Discuss. 20, 1–23.

Sparks, R.S.J., Annen, C., Blundy, J.D., Cashman, K.V., Rust, A.C., Jackson, M.D., 2019. Formation and dynamics of magma reservoirs. Phil. Trans. R. Soc. A 377 (2139), 20180019.

Sternai, P., Caricchi, L., Castelltort, S., Champagnac, J.-D., 2016. Deglaciation and glacial erosion: a joint control on magma productivity by continental unloading. Geophys. Res. Lett. 43, 1632–1641.

Sternai, P., Caricchi, L., Pasquero, C., Garzanti, E., van Hinsbergen, D.J., Castelltort, S., 2019. Magmatic forcing of cenozoic climate? J. Geophys. Res. Solid Earth 125. https://doi.org/10.1029/2018JB016460.

Stevens, N.T., Parizek, B.R., Alley, R.B., 2016. Enhancement of volcanism and geothermal heat flux by ice-age cycling: a stress modeling study of Greenland. J. Geophys. Res. Earth 121, 1456–1471.

Stewart, I.S., 2018. Did sea-level change cause the switch from fissure-type to central-type volcanism at Mount Etna, Sicily? Episodes Journal of International Geoscience 41 (1), 7–16.

Sugden, D.E., Hulton, N.R.J., Purves, R.S., 2002. Modelling the inception of the Patagonian icesheet. Quat. Int. 95–96, 55–64. https://doi.org/10.1016/S0277-3791(01)00103-2.

Tassara, A., Götze, H.J., Schmidt, S., Hackney, R., 2006. Three-dimensional density model of the Nazca plate and the Andean continental margin. J. Geophys. Res. Solid Earth 111. https://doi.org/10.1029/2005JB003976.

Till, C.B., Kent, A.J.R., Abers, G.A., Janiszewski, H.A., Gaherty, J.B., Pitcher, B.W., 2019. The causes of spatiotemporal variations in erupted fluxes and compositions along a

volcanic arc. Nat. Commun. 10, 1350. https://doi.org/10.1038/s41467-019-09113-0.
Towhata, I., Goto, S., Goto, S., Akima, T., Tanaka, J., Uchimura, T., Wang, G., Yamaguchi, H., Aoyama, S., 2021. Mechanism and future risk of slope instability induced by extreme rainfall event in Izu Oshima Island, Japan. Nat. Hazards 105, 501–530.
Townsend, M., Huber, C., 2020. A critical magma chamber size for volcanic eruptions. Geology 48 (5), 431–435.
Townsend, M., Huber, C., Degruyter, W., Bachmann, O., 2019. Magma chamber growth during intercaldera periods: insights from thermo-mechanical modeling with applications to Laguna del Maule, Campi Flegrei, Santorini, and Aso. Geochem. Geophys. Geosyst. 20, 1574–1591.
Ugelvig, S.V., Egholm, D.L., Iverson, N.R., 2016. Glacial landscape evolution by subglacial quarrying: a multiscale computational approach. J. Geophys. Res. Earth 121, 2042–2068.
Van Daele, M., Moernaut, J., Doom, L., Boes, E., Fontijn, K., Heirman, K., Vandoorne, W., Hebbeln, D., Pino, M., Urrutia, R., Brümmer, R., De Batist, M., 2015. A comparison of the sedimentary records of the 1960 and 2010 great Chilean earthquakes in 17 lakes: implications for quantitative lacustrine palaeoseismology. Sedimentology 62, 1466–1496.
Van Daele, M., Bertrand, S., Meyer, I., Moernaut, J., Vandoorne, W., Siani, G., De Batist, M., 2016. Late Quaternary evolution of Lago Castor (Chile, 45.6 S): timing of the deglaciation in northern Patagonia and evolution of the southern westerlies during the last 17 kyr. Quat. Sci. Rev. 133, 130–146.
van Wyk de Vries, M., Bingham, R.G., Hein, A.S., 2018. A new volcanic province: an inventory of subglacial volcanoes in West Antarctica. Geol. Soc. Lond. Spec. Publ. 461 (1), 231–248. https://doi.org/10.1144/sp461.7.
van Zalinge, M.E., Mark, D.F., Sparks, R.S.J., Tremblay, M.M., Keller, C.B., Cooper, F.J., Rust, A., 2022. Timescales for pluton growth, magma-chamber formation and super-eruptions. Nature 608, 87–92.
Vander Auwera, J., Montalbano, S., Namur, O., Bechon, T., Schiano, P., Devidal, J.L., Bolle, O., 2021. The petrology of a hazardous volcano: Calbuco (Central Southern Volcanic Zone, Chile). Contrib. Mineral. Petrol. 176, 1–34.
Walcott, R.I., 1972. Past sea levels, eustasy and deformation of the earth. Quat. Res. 2, 1–14. https://doi.org/10.1016/0033–5894(72)90001–4.
Wallace, P.J., Plank, T., Edmonds, M., Hauri, E.H., 2015. Volatiles in magmas. In: The Encyclopedia of Volcanoes. Academic Press, pp. 163–183.
Watt, S.F., Pyle, D.M., Naranjo, J.A., Rosqvist, G., Mella, M., Mather, T.A., Moreno, H., 2011. Holocene tephrochronology of the Hualaihue region (Andean southern volcanic zone, 42 S), southern Chile. Quat. Int. 246, 324–343.
Watt, S.F.L., Pyle, D.M., Mather, T.A., 2013. The volcanic response to deglaciation: evidence from glaciated arcs and a reassessment of global eruption records. Earth Sci. Rev. 122, 77–102. https://doi.org/10.1016/j.earscirev.2013.03.007.
Weber, G., Blundy, J., 2024. A machine-learning-based thermobarometer for magmatic liquids. J. Petrol. 65 https://doi.org/10.1093/petrology/egae020.
Wieser, P., Petrelli, M., Lubbers, J., Wieser, E., Özaydin, S., Kent, A.J., Till, C., 2022. Thermobar: an open-source Python3 tool for thermobarometry and hygrometry. Volcanica. https://doi.org/10.30909/vol.05.02.349384.
Wieser, P.E., Kent, A.J., Till, C.B., Donovan, J., Neave, D.A., Blatter, D.L., Krawczynski, M.J., 2023a. Barometers behaving badly I: assessing the influence of analytical and experimental uncertainty on clinopyroxene thermobarometry calculations at crustal conditions. J. Petrol. 64 (2) p.egac126.
Wieser, P.E., Kent, A.J., Till, C.B., 2023b. Barometers behaving badly II: a critical evaluation of Cpx-only and Cpx-Liq thermobarometry in variably-hydrous arc magmas. J. Petrol. 64 (8) p.egad050.
Wieser, P.E., Kent, A.J., Till, C.B., Abers, G.A., 2023c. Geophysical and geochemical constraints on magma storage depths along the Cascade arc: knowns and unknowns. Geochem. Geophys. Geosyst. 24 (11) p.e2023GC011025.
Wilson, A.M., Russell, J.K., 2020. Glacial pumping of a magma-charged lithosphere: a model for glaciovolcanic causality in magmatic arcs. Earth Planet. Sci. Lett. 548, 116500.
Wilson, A.M., Russell, J.K., Ward, B.C., 2019. Paleo-glacier reconstruction in southwestern British Columbia, Canada: a glaciovolcanic model. Quat. Sci. Rev. 218, 178–188.
Winslow, H., Ruprecht, P., Gonnermann, H.M., Phelps, P.R., Muñoz-Saez, C., Delgado, F., Pritchard, M., Amigo, A., 2022. Insights for crystal mush storage utilizing mafic enclaves from the 2011–12 Cordón Caulle eruption. Sci. Rep. 12 (1), 9734.
Yan, Q., Wei, T., Zhang, Z., 2022. Modeling the climate sensitivity of Patagonian glaciers and their responses to climatic change during the global last glacial maximum. Quat. Sci. Rev. 288, 107582.